NETL

NATIONAL ENERGY TECHNOLOGY LABORATORY

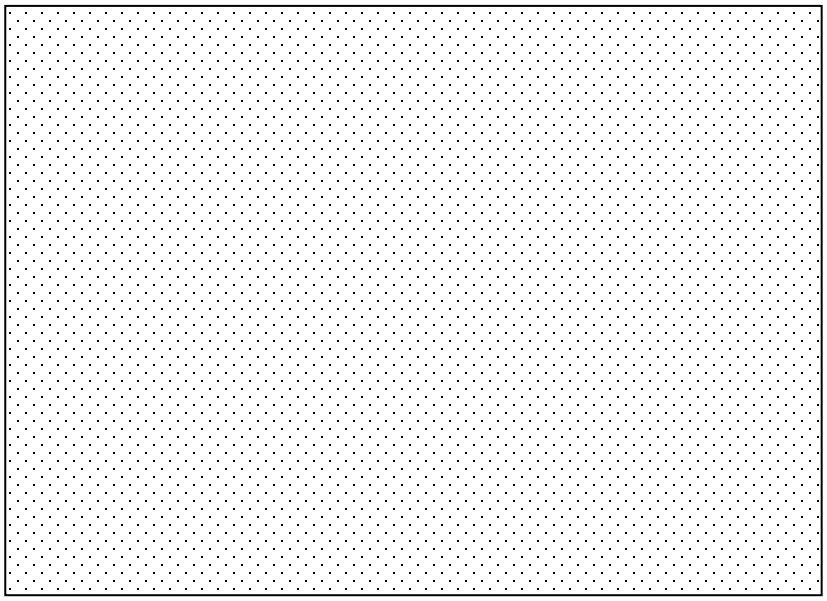

MFIX Documentation Volume 3: Verification and Validation Manual Second Edition

October, 2018

U.S. DEPARTMENT OF ENERGY | NATIONAL ENERGY TECHNOLOGY LABORATORY

Office of Fossil Energy

NETL-PUB-XXXXX

Disclaimer

This report was prepared as an account of work sponsored by an agency of the United States Government. Neither the United States Government nor any agency thereof, nor any of their employees, makes any warranty, express or implied, or assumes any legal liability or responsibility for the accuracy, completeness, or usefulness of any information, apparatus, product, or process disclosed, or represents that its use would not infringe privately owned rights. Reference therein to any specific commercial product, process, or service by trade name, trademark, manufacturer, or otherwise does not necessarily constitute or imply its endorsement, recommendation, or favoring by the United States Government or any agency thereof. The views and opinions of authors expressed therein do not necessarily state or reflect those of the United States Government or any agency thereof.

Suggested Citation: J. Musser, A. Vaidheeswaran, and M.A. Clarke, eds. *MFIX Documentation Volume 3: Verification and Validation Manual*; 2nd ed. NETL-PUB-XXXXX; NETL Technical Report Series; U.S. Department of Energy, National Energy Technology Laboratory: Morgantown, WV, 2018.

Keywords:
MFIX; Verification; Validation; Multiphase; Method of Manufactured Solutions; Computational Fluid Dynamics; Discrete Element Method; Two-Fluid Model

MFIX Documentation Volume 3: Verification and Validation Manual

J. Musser[1], A. Vaidheeswaran[1,2], and M.A. Clarke[1,2]

[1] Research and Innovation Center, National Energy Technology Laboratory

[2] West Virginia University Research Corporation

NETL-PUB-XXXXX

October, 2018

NETL-PUB-XXXXX

NETL Contacts:

J. Musser, Principal Investigator

William A. Rogers, Technical Portfolio Lead

Bryan Morreale, Executive Director, Research and Innovation Center

This page is intentionally blank.

Table of Contents

List of Figures

List of Tables

Acronyms and Abbreviations

BC	Boundary Condition
CFD	Computational Fluid Dynamics
CV	Control Volume
CI	Continuous Integration
DEM	Discrete Element Model
EE	Eulerian-Eulerian
MFIX	Multiphase Flow with Interphase eXchanges
MMS	Method of Manufactured Solutions
MPPIC	Multiphase Particle-In-Cell
PDE	Partial Differential Equation
SQA	Software Quality Assurance
TFM	Two-Fluid Model
V&V	Verification and Validation
UQ	Uncertainty Quantification

Executive Summary:

The MFIX Verification and Validation Manual aims to document verification tests and validation cases for the MFIX suite. Additionally, this manual attempts to capture best practices for verification and validation as part of a broader approach to software quality assurance. The goal is to perform a systematic verification of features available in MFIX for correctness and numerical accuracy.

Contributors:

(Alphabetical by last name)

Sofiane Benyahia
Aniruddha Choudhary
Mary Ann Clarke
Jean-François Dietiker
William Fullmer
Janine Galvin
Aytekin Gel
Chris Guenther
Tingwen Li
Mark Meredith
Aaron Morris
Jordan Musser
Thomas O'Brien
Sreekanth Pannala
William Rogers
Mehrdad Shahnam
Madhava Syamlal
Avinash Vaidheeswaran

The editors thank all contributors, especially our colleagues in the NETL Multiphase Flow Science Group, for their assistance and feedback in the creation and maintenance of this document.

Chapter 1: Introduction

The MFIX Verification and Validation Manual, referred to herein as the V&V Manual, aims to document verification tests and validation cases for the MFIX suite. Additionally, this manual attempts to capture best practices for V&V as part of a broader approach to software quality assurance (SQA). The goal is to perform a systematic verification of features available in the code for correctness and numerical accuracy. Future work will include validation cases to assess the suitability of the physical models implemented within MFIX. The V&V Manual also serves as a guide for periodic and automated testing of the software by the developers.

1.1 Verification and Validation

For the purpose of this manual, the terms *verification* and *validation* are defined as follows [1]:

- **Verification**: The process of determining that a numerical model implementation accurately represents the developer's conceptual description of the model and the mathematical solution to the model.
- **Validation:** The process of determining the degree to which a model is an accurate representation of the real world from the perspective of the intended uses of the model.

Roache [2] succinctly describes verification as an assessment on "solving the *equations right*" whereas validation is "solving the *right equations*." Figure 1-1 illustrates the relationship between verification and validation processes schematically.

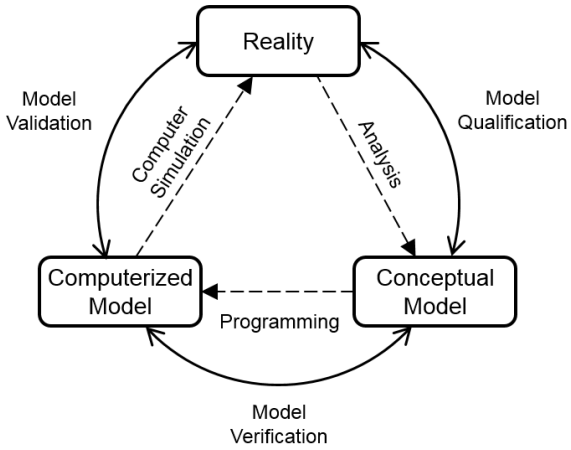

Figure 1-1: Verification and validation process [3, 4].

Verification deals with the mathematics of the simulation and involves assessing the correctness of the computer code and numerical algorithms (i.e., code verification) as well as the accuracy of the numerical solution (i.e., solution verification). Validation deals with the physics of the problem and assesses whether the selected mathematical model satisfactorily predicts the physics

of interest. Roache [5] further noted the distinction between verification and validation as, "Verification is a mathematics issue; not a physics issue." Hence, verification precedes validation.

1.2 Verification Test Selection Criteria

Verification test cases are selected based upon the following criteria:

- Each test case should exercise one or more sub-models for a physical phenomenon
- Simulations must be computationally inexpensive to facilitate regular testing
- There should be minimal overlap between tests

The preference and thereby quality of a test is assessed on the following criteria:

- (Most preferable) Examination of numerical error between the exact solution and the numerical solution for problems where an analytical solution is available (i.e., verification using method of exact solutions) or a manufactured solution is obtainable
- (Less preferable) Comparison of numerical solutions to established results in literature (i.e., similar to validation, but using benchmark problems)
- (Least preferable) Comparison of numerical solutions to results obtained from previous versions of the same code (i.e., regression test) or from another verified code (i.e., code comparison)

1.3 Testing Frequency

Cases presented within this document are tested at various intervals as part of the SQA process. Before 2014, code integrity in MFIX was tracked through a series of nightly regression tests based on an open source software testing framework called QMTest, which provided a single snapshot on a daily basis [6]. This method was replaced by a continuous integration (CI) server for greater testing and archival flexibility.

Cases that execute quickly are tested whenever modifications are committed to the source code repository to quickly detect any issues generated by the changes. However, computationally burdensome verification and validation cases are tested less frequently to prevent overwhelming the CI server. A summary table at the start of each chapter indicates the frequency at which each case is tested.

1.4 Case files and datasets

Case files and datasets for the tests outlined in this document are provided with the MFIX source code under the **mfix/tests** directory. All presented data are representative of results from the current MFIX release unless explicitly noted.

1.5 Organization

Chapter 2 provides verification tests that use the Method of Manufactured Solution (MMS) to determine whether the observed order of error reduction with grid refinement matches the formal order. Order testing with MMS is considered to be a very rigorous procedure for code verification.

Chapters 3 and 4 provide verification tests that use benchmark solutions of simple problems to test the two main models of the MFIX software suite: (1) Two-Fluid Model, and (2) Discrete Element Model. This process examines various aspects of the code but only for problems with significantly simplified physics.

Figure 1-2 shows the scope of the V&V activity covered in this manual.

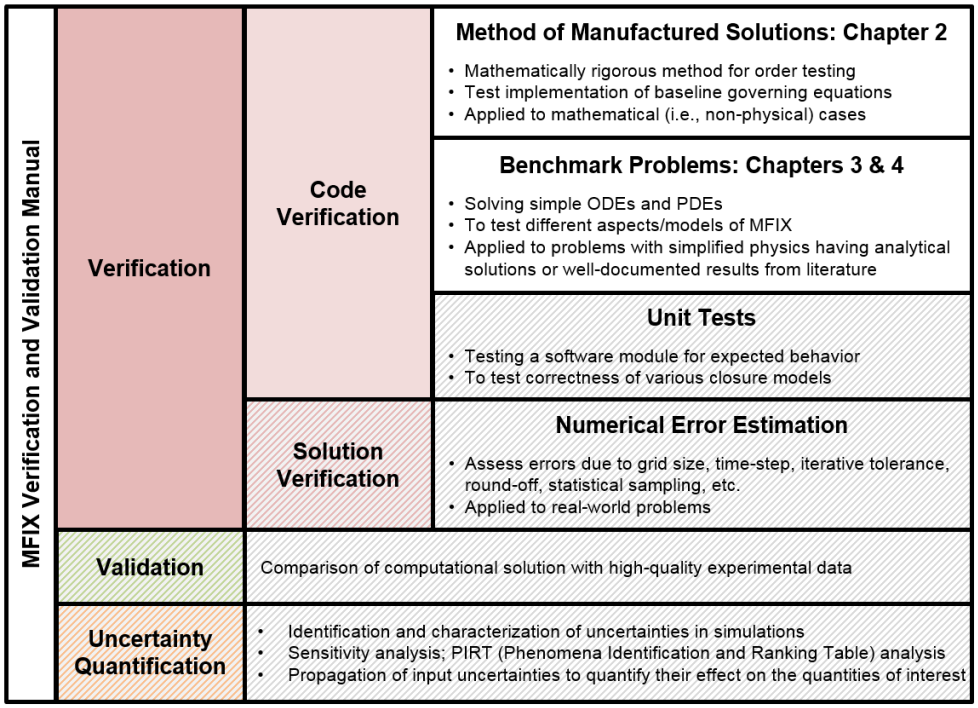

Figure 1-2: Scope of MFIX verification and validation activity covered in this manual. (Greyed parts indicate future or ongoing activities not presented in the current version of this document.)

Chapter 2: Method of Manufactured Solutions (MMS)

Order of accuracy testing (or 'order testing') is considered a rigorous method for performing code verification. During order testing, the formal order of accuracy of a numerical scheme is compared to the observed order of accuracy. The observed order is the order at which the discretization error (which is the difference between the numerical solution to the discrete equations and the exact solution to the PDEs) decreases with systematic mesh refinement. However, the exact solution to a PDE is unknown for most practical problems. In this scenario, the Method of Manufactured Solutions (MMS) [7] can be used where a selected analytical function (called a 'manufactured solution') is forced to be the exact solution by modifying the PDE through additional source terms.

The MMS test cases presented in this chapter are summarized in Table 2-1. These test cases offer an increasing level of computational complexity to isolate any potential problems in the source code. Three explanatory test cases that employ various simplifying assumptions are provided to assist the reader in understanding the MMS. Additional test cases were selected based upon their ability to invoke various parts of the MFIX code, and present physically acceptable data. All cases are executed in serial mode unless explicitly noted.

Table 2-1: Summary of MMS tests by feature

	Frequency†	Dimension	Multiphase	Continuity	Momentum	Thermal Energy	Species Mass	Granular Energy	Turbulence	No-slip Wall BC	Free-slip Wall BC	Pressure Outflow	Distributed Memory	Shared Memory
MMS-EX01	X	1D			✓									
MMS-EX02	X	1D				✓								
MMS-EX03	X	1D				✓								
MMS01	M	2D		✓	✓									
MMS02	M	3D	✓	✓	✓	✓								
MMS03	M	3D	✓		✓	✓								
MMS04	M	3D								✓				
MMS05	M	3D									✓			
MMS06	M	3D										✓		

† C-Incorporated into the continuous integration server;
M-Monthly; Q-Quarterly; D-Disabled; X-Manual

2.1 MMS Procedure Overview

To better instruct the reader, the procedure for using a MMS to conduct an order of accuracy test is summarized by example [8, 9]:

1. Allow any partial differential equation in n-dimensions to be represented through the notation:

$$L[u(x_1, x_2, \cdots, x_n, t)] = 0 \tag{2-1}$$

For example, a one-dimensional non-linear Burger equation:

$$u_t + uu_x = \alpha u_{xx} \tag{2-2}$$

would be represented as:

$$L[u(x,t)] = u_t + uu_x - \alpha u_{xx} = 0 \tag{2-3}$$

2. Make up a manufactured solution to the proposed partial differential equation. The chosen solution does not need to represent the solution to a physical problem. The MMS is a mathematical exercise to determine if a piece of software will accurately calculate a solution to its prescribed numerical order.

For example, allow: $U(x,t) = A + \sin(x + Ct)$ where A and C are constants, to be a solution to $L[u(x,t)]$.

The key is that whatever one chooses for $U(x,t)$, it must be mathematically analytic, meaning fully differentiable with continuous derivatives to at least the order of the partial differential equation one is trying to solve over the full domain of the problem. In this example, the constant value function A and the sinusoidal function $\sin(x + Ct)$ obviously meet these criteria. Do not choose functions that display discontinuities of any type for any derivative if the domain of interest extends *through* those discontinuities. In addition, it is important that all terms in a given manufactured solution are of similar magnitude. This assures that solutions are not dominated by a single term which might skew order of accuracy results.

It is essential to choose solutions that do not engage physical constraints within the code that is under evaluation. For example, MFIX issues an error message and stops all calculations if the temperature in any computational cell falls below 250 Kelvin. So, if testing the energy equation, the manufactured solution should never present a value less than 250, as this value is contextually interpreted as an unphysical temperature.

3. Apply the manufactured solution to the partial differential equation being solved. This means create the derivatives represented in the original problem and substitute them into the equation.

For example, using $U(x,t) = A + \sin(x + Ct)$ as a manufactured solution for $L[u(x,t)] = u_t + uu_x - \alpha u_{xx} = 0$ requires

$$L[u(x,t)]_{U(x,t)} = \frac{\partial}{\partial t}\big(U(x,t)\big) + U(x,t)\frac{\partial}{\partial x}\big(U(x,t)\big) - \alpha\frac{\partial^2}{\partial x^2}\big(U(x,t)\big) = 0 \tag{2-4}$$

After substitution,

$$L[u(x,t)]_{U(x,t)} = C\cos(x + Ct) + (A + \sin(x + Ct))(\cos(x + Ct)) - \alpha(-\sin(x + Ct)) = 0 \tag{2-5}$$

Or,

$$L[u(x,t)]_{U(x,t)} = (A + C)\cos(x + Ct) + \sin(x + Ct)\cos(x + Ct) + \alpha\sin(x + Ct) = 0 \tag{2-6}$$

$L[u(x,t)]_{U(x,t)}$ represents what are called *source terms* in MMS. Thinking about this using notation:

$$L[u(x,t)] = 0 = L[u(x,t)]_{U(x,t)} \tag{2-7}$$

Or,

$$L[u(x,t)] - L[u(x,t)]_{U(x,t)} = 0 \tag{2-8}$$

After calculation, any arithmetic difference between the numerical solution and the exact solution is assumed to originate from the numerical method.

4. To properly solve a partial differential equation of the form $L[u(x_1, x_2, \cdots, x_n, t)] = 0$, one needs appropriately chosen initial and boundary values.

   So, by example, assume that the physical domain of interest is $x\epsilon[0,1]$ and allow $t\epsilon[0,\infty)$.

   First, force the initial condition of $u(x,0)$ to align with that of the manufactured solution, $U(x,0)$ by choosing,

$$u(x,0) = U(x,0) = A + \sin\big(x + C(0)\big) = A + \sin(x) \tag{2-9}$$

   Then, select boundary conditions in any meaningful way, forcing alignment between the proposed partial differential equation and the manufactured solution. For example, perhaps fixed boundary conditions are useful. These are sometimes called Dirichlet boundary conditions. Applying a fixed boundary condition means choose functions for fixed boundary locations that will be maintained through all time-steps. It does <u>not</u> mean

that a boundary must have the same value for all time, although that is a possibility (the function chosen might be a constant).

So, for this example, an appropriate fixed boundary condition would be:

$$u(0,t) = U(0,t) = A + \sin(0 + Ct) = A + \sin(Ct)$$
$$u(1,t) = U(1,t) = A + \sin(1 + Ct) \tag{2-10}$$

Note that in this example, the *fixed* (Dirichlet) boundary condition varies with time.

The type of boundary condition is insignificant to the method of manufactured solutions. One can easily choose Neumann (flux conditions at the boundary), Cauchy (a mix of fixed conditions and at least one derivative in the direction of the normal of the boundary), Robin (weighted combinations of Neumann and Dirichlet conditions over all boundaries) or mixed conditions (different boundary condition types on different subsets of the boundary) as each partial differential equation application is explored.

By example, a different solution to our proposed problem will occur if we shift to a *mixed* boundary condition such that:

$$u(0,t) = U(0,t) = A + \sin(0 + Ct) = A + \sin(Ct) \quad (Dirichlet)$$
$$\frac{\partial}{\partial x}\big(u(1,t)\big) = \frac{\partial}{\partial x}\big(U(1,t)\big) = \frac{\partial}{\partial x}(A + \sin(1 + Ct)) = \cos(1 + Ct) \quad (Neumann) \tag{2-11}$$

In this way, the method of manufactured solutions allows the investigator to examine how the application of different boundary conditions affects the overall veracity of numerical approximations within the context of problems where solutions can be found through explicit hand calculation.

5. Theoretically, when a manufactured exact solution is known, computer algorithms applied to imitate that result should converge systematically toward *exactness* as the calculation space is ever more refined. Ideally, one might expect an eventual numerical result to differ from an exact solution by no more than $\mathcal{O}(\text{machine epsilon})$. Of course, the theoretical threshold of solution quality varies widely from this value as there are few calculations that can be held to such a high standard. For example, computers estimate all transcendental functions with truncated power series on computers, regardless of what a programmer types into code, and these functions are inherently burdened with this approximation error.

   However, one can systematically refine a mesh and recalculate the solution to proposed problems in search of exactness. Once the arithmetic difference between the discretized solution and a manufactured solution remains constant, regardless of further mesh refinement, one has discovered the best numerical solution possible for a given code and

a given problem. If the error between discretized solution and manufactured solution is acceptable by some standard, a code can be considered numerically *verified*. Note that this verification is limited to those code components invoked when setting up a MMS. As is the case for MFIX, most codes are far too complex to complete a full verification in a single MMS.

6. Global discretization error, DE_ℓ , is the arithmetic difference between the computer (approximate or discrete) evaluation of the manufactured solution to a by hand (exact) solution. The script ℓ is to remind the user of mesh ℓevel.

   Rather than evaluate discretization error one cell at a time, one can further consider global discretization error through various mathematical norms. An L_1norm is an average absolute error over all cell locations $(ijk = 1, \dots, n)$ in a calculation represented through an absolute difference.

$$L_1\text{:}\ \ \|DE_\ell\|_1 = \frac{\sum_{ijk=1}^{n}\left|DE_{\ell,ijk}\right|}{n} \tag{2-12}$$

   An L_2 norm is a root mean square error over all cell locations $(ijk = 1, \dots, n)$.

$$L_2\text{:}\ \|DE_\ell\|_2 = \sqrt{\frac{\sum_{ijk=1}^{n}\left|DE_{\ell,ijk}\right|^2}{n}} \tag{2-13}$$

   An L_∞ norm is the maximum error in any single cell location $(ijk = 1, \dots, n)$.

$$L_\infty = \|DE_\ell\|_\infty = \max_{ijk}\left|DE_{\ell,ijk}\right| \tag{2-14}$$

7. As mesh size, h, changes, one collects the normed values of global discretization error and applies them to create an observed order, p.

$$p = \frac{ln\left(\frac{\|DE_{\ell+1}\|}{\|DE_\ell\|}\right)}{ln\left(\frac{h_{\ell+1}}{h_\ell}\right)} = \frac{ln\left(\frac{\|DE_{\ell+1}\|}{\|DE_\ell\|}\right)}{ln(r)} \tag{2-15}$$

   In this notation, mesh level, ℓ, is largest at the coarsest mesh, and smallest at the most refined mesh. One will also see the observed order formula where the ratio between two mesh sizes (as seen in the denominator of p) is called a mesh refinement factor, r. Furthermore, the term *grid size measure*, $\breve{h}$, is a ratio formed by comparing the number of

divisions making up the finest mesh to the current mesh. Figure 2-1 works to clarify these definitions within the context of observed order, and illustrates an observed order plot where $r = 2$, between subsequent mesh levels. Note that the use of grid size measure eliminates the need for any units in graphical representations of observed order.

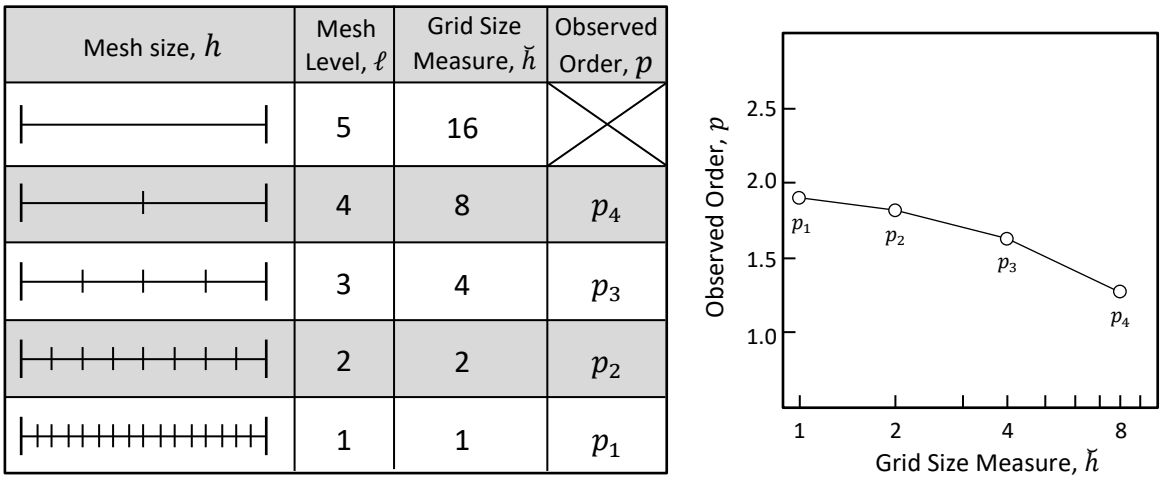

Figure 2-1: Procedure for order of accuracy testing.

Ideally, one makes as many simulations as necessary to show that $\lim_{h \to 0} p$ is constant, thereby inferring that the best possible numerical solution has been made, and further simulation is unwarranted.

Note that the norm chosen for the calculation of observed order may affect the outcome of this assessment. For example, the most challenging norm related above is L_∞, as it isolates the largest error in any given simulation. The least challenging norm is L_1, as it will most easily mask localized high level error with areas of good agreement across any given domain.

2.2 MMS-EX01: One dimensional steady state Burger's equation

2.2.1 Description

The gas-phase momentum equations in MFIX have the following generalized form:[1]

$$\frac{\partial}{\partial t}\left(\varepsilon_g \rho_g u_{gi}\right) + \frac{\partial}{\partial x_j}\left(\varepsilon_g \rho_g u_{gj} u_{gi}\right) = -\frac{\partial P_g}{\partial x_i} + \frac{\partial \tau_{gij}}{\partial x_j} + \varepsilon_g \rho_g g_i + \mathcal{S}_{gi} \tag{2-16}$$

where,

$$\tau_{gij} = 2\mu_g \left[\frac{1}{2}\left(\frac{\partial u_{gi}}{\partial x_j} + \frac{\partial u_{gj}}{\partial x_i}\right) - \frac{1}{3}\frac{\partial u_{gk}}{\partial x_k}\delta_{ij}\right] \tag{2-17}$$

To build on the previous example, the momentum equations can be recast as the one-dimensional steady state Burger's equation by imposing the following simplifying assumptions:[2]

1. A steady state simulation is needed to remove the momentum equations' transient term.
2. Calculations are restricted to one dimension.
3. The domain is of unit length in the x-axial direction: $x\epsilon[0,5]$.
4. The gas volume fraction and density are set to one, $\varepsilon_g = 1$ and $\rho_g = 1$.
5. The gas viscosity is chosen as $\mu_g = 3/4$.
6. Gravity and all other source terms are set to zero, $g = 0$ and $\mathcal{S}_{gi} = 0$.
7. Finally, because the pressure solver is integrated with the momentum equations, it is important to decouple the pressure correction step from the calculation.

The momentum equations with the above simplifications reduce to the one-dimensional Burger's equation,

$$u_g \frac{\partial u_g}{\partial x} - \frac{\partial^2 u_g}{\partial x^2} = 0 \tag{2-18}$$

where the subscript indicating dimensionality has been dropped for notational clarity.

Following the method of manufactured solutions, the partial differential equation is recast as:

$$L(x) = u u_x - u_{xx} \tag{2-19}$$

MMS requires the selection of a manufactured solution. Arbitrarily, choose any suitable analytic form of appropriate continuous, differential order. In this case, note that whatever manufactured

[1] The conservative form of the fluid momentum equations is presented here, however, the non-conservative form is solved in MFIX. The non-conservative form is obtained by subtracting the continuity equation from the conservative form.

[2] Assumptions that reduce model complexity are typically avoided when using the MMS. However, this example intentionally simplifies the momentum equations to make the example easier to follow.

solution is chosen must be continuously differentiable through its second derivative. Aside from asymptotic functions that may exhibit unphysical local changes, most any analytic function will be a suitable choice for this application. So, keeping things simple, as in the prior explanation,

$$U(x) = 0.5 + \sin(x) \tag{2-20}$$

Then, apply this form to $L(x)$:

$$L(x)_{U(x)} = (0.5 + \sin(x))\frac{\partial}{\partial x}(0.5 + \sin(x)) - \frac{\partial^2}{\partial x^2}(0.5 + \sin(x)) \tag{2-21}$$

$$L(x)_{U(x)} = (0.5 + \sin(x))(\cos(x)) - (-\sin(x)) \tag{2-22}$$

$$L(x)_{U(x)} = 0.5\cos(x) + \cos(x)\sin(x) + \sin(x) \tag{2-23}$$

Finally, cast appropriate initial and/or boundary conditions. For this case, since time is inconsequential, no initial condition is warranted. Focus then shifts to boundary conditions. With the domain of interest being $x\epsilon[0,1]$, fixed boundary conditions are given by:

$$\begin{aligned} U(0) &= 0.5 + \sin(0) = 0.5 \\ U(1) &= 0.5 + \sin(5) \end{aligned} \tag{2-24}$$

2.2.2 Setup

Initially, only the x-direction momentum equation on a domain with unit dimensions is considered. Subsequently, the setup is executed in the y- and z- directions to determine if problem orientation influences the observed order.

Computational/Physical model

1D, Steady-state, incompressible
Single-phase (no solids)
No gravity
Turbulence equations are not solved (Laminar)
Uniform mesh
Central scheme

Geometry

Coordinate system	Cartesian
Domain length, L (x)	1.0 (m)

Material†

Fluid density, ρ_g	1.0 (kg·m^{-3})
Fluid viscosity, μ_g	0.75 (Pa·s)

Initial Conditions

Pressure *(gauge)*, P_g	0.0 (Pa)
Fluid x-velocity, u_g	1.0 (m·sec^{-1})

Boundary Conditions‡

East / West (x)	Mass inflow (MMS)
All other boundaries	Cyclic

† Material properties selected to ensure comparable contribution from convection and diffusion terms.
‡ The manufactured solution imposed on the east / west boundaries is given by equation (2-24) .

User-defined functions specific to the MMS implementation in MFIX are used to introduce the source term. Specifically, for each discretized x-momentum computational cell, equation (2-23) is evaluated and subtracted from the right hand side of the linear equation. Once the simulation has converged, the L_1, L_2 and L_∞ error norms are computed by referencing equation (2-20).

2.2.3 Results

Following the outline of MMS methodology, three separate 1-dimensional systems (x, y and z) were created, each having 4,8, 16, 32, 64, and 128 cells, using the steady state Burger's equation and manufactured solution previously described.

An observed order for each direction is calculated using L_1, L_2 and L_∞ error norms. The following tables and figure illustrate these data. One can quickly see from the tabled *L*-norms and subsequently calculated observed order that direction does not have a large influence on these values. All data points to a 2nd order (*p*) convergence of the steady state Burger's equation using MFIX. In the present input-deck construction, whereby the numerical method implemented is *central differencing* method, this is the best outcome to expect.

Table 2-2: Observed Order, *p*, for steady state Burger's equation using $U(x) = 1 + \sin(x)$ on $0 \le x \le 1$.

Mesh Divisions	L_1-norm	L_2-norm	L_∞-norm	*p* (from L_1)	*p* (from L_2)	*p* (from L_∞)
4	2.4834E-01	2.5853E-01	3.1909E-01	N/A	N/A	N/A
8	5.2081E-02	5.3318E-02	7.0000E-02	2.2535	2.2776	2.1886
16	1.1771E-02	1.2317E-02	1.6652E-02	2.1455	2.1139	2.0716
32	2.8250E-03	2.9965E-03	4.1128E-03	2.0589	2.0393	2.0176
128	6.9383E-04	7.4135E-04	1.0251E-03	2.0256	2.0151	2.0043

Hence, these data imply that the terms engaged in the momentum equation through the evaluation of the steady state Burger's equation are numerically closed on 2nd order approximations which is correct and *verified* by the method of manufactured solutions.

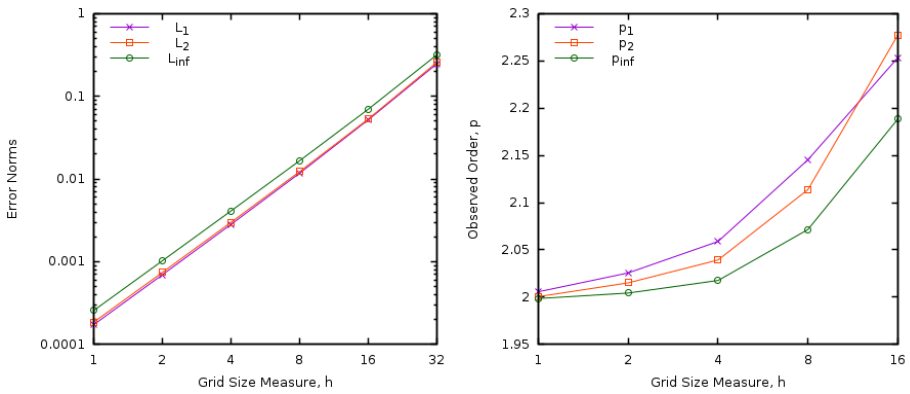

Figure 2-2: Observed Order, MMS Solution to 1-D steady state Burger's equation in MFIX, using $U(x) = 1 + \sin(x)$ on $0 \leq x \leq 1$.

As a final observation, note that observed order appears to increase with decreasing spatial mesh. However, *as expected*, L-norms decrease with increasing mesh density, indicating a better overall solution.

2.3 MMS-EX02: One dimensional steady state heat equation

2.3.1 Description

The gas phase energy equations in MFIX are:

$$\varepsilon_g \rho_g C_{p_g} \left[\frac{\partial T_g}{\partial t} + U_{gj} \frac{\partial T_g}{\partial x_j} \right] = -\frac{\partial}{\partial x_j} \left(-\varepsilon_g \kappa_g \frac{\partial T_g}{\partial x_j} \right) - \sum_{n=1}^{N_g} h_{gn} R_{gn} + \mathcal{S}_g \qquad (2\text{-}25)$$

The energy equations can be recast as the one-dimensional heat equation by imposing the following simplifying assumptions: [3]

1. A steady state simulation is needed to remove the energy equations' transient term.
2. Calculations are restricted to one dimension.
3. The domain length in the x-axial direction is $x \epsilon [0,5]$.
4. The gas volume fraction, density, thermal conductivity, and specific heat are set to one, $\varepsilon_g = 1$, $\rho_g = 1$, $\kappa_g = 1$, and $C_{pg} = 1$.
5. The gas momentum equations are not solved and initial velocity field is set to zero so that the convective term is zero.
6. There are no chemical reactions, interphase mass transfer or other sources of energy implying: $\sum_{n=1}^{N_g} h_{gn} R_{gn} + \mathcal{S}_g = 0$.

[3] Again, simplifying assumptions are typically avoided when using the MMS. However, this example intentionally simplifies the energy equations to make the example easier to follow.

On re-evaluation of the energy equations, the following one-dimensional form (aka the steady state heat equation) emerges:

$$\frac{\partial^2 T_g}{\partial x^2} = 0 \tag{2-26}$$

Following the method of manufactured solutions, the partial differential equation is recast as:

$$L(x) = \left(T_g\right)_{xx} = 0 \tag{2-27}$$

MMS requires the selection of a manufactured solution. Because this is a steady-state form, the manufactured solution is chosen not to incorporate a time variable for simplicity. Arbitrarily, choose any suitable analytic form of appropriate continuous, differential order. In this case, observe that whatever manufactured solution we choose must be continuously differentiable through its second spatial derivative. Also note, in MFIX, temperature is calculated absolutely and is restricted as: $250 < u < 4000$ (which represents the Kelvin scale). Values outside of these bounds cause a fatal error within the code. So, in this case, there is a caveat that requires the manufactured solution chosen cannot present out-of-bound values on any domain of interest. In this example, the domain, $0 \leq x \leq 5$, and the manufactured solution:

$$T_g(x) = 500 + (1 + x^3) = 501 + x^3 \tag{2-28}$$

work within the MFIX constraints. Continuing to follow the MMS, this solution is applied to $L(x)$:

$$L(x)_{T_g(x)} = \frac{\partial^2}{\partial x^2}(501 + x^3) \tag{2-29}$$

$$L(x)_{T_g(x)} = 6x \tag{2-30}$$

Then, appropriate initial and/or boundary conditions are cast. For this case, since time is inconsequential, no initial condition is warranted. Focus then shifts to boundary conditions.

On the domain of interest: $x\epsilon[0,5]$, Dirichlet boundary conditions are:

$$\begin{aligned} T_g(0) &= 501 + 0^3 = 501 \\ T_g(5) &= 501 + 5^3 = 501 + 125 = 626 \end{aligned} \tag{2-31}$$

2.3.2 Setup

This case is designed to test the energy equation implementation.

Computational/Physical model

1D, Steady-state, incompressible
Single-phase (no solids)

No gravity
Turbulence equations are not solved (Laminar)
Uniform mesh
Central scheme

Geometry	
Coordinate system	Cartesian
Domain length, L	5.0 (m)
Material†	
Fluid density, ρ_g	1.0 (kg·m^{-3})
Fluid viscosity, μ_g	1.0 (Pa·s)
Fluid specific heat, C_{pg}	1.0 (J·kg^{-1}·K^{-1})
Initial Conditions	
Pressure *(gauge)*, P_g	0.0 (Pa)
Temperature, T_g	550.0 (K)
Boundary Conditions‡	
East / West (x)	(MMS)
All other boundaries	Adiabatic Walls

† Material properties selected to ensure comparable contribution from convection and diffusion terms.
‡ The manufactured solution imposed on the east / west boundaries is given by equation (2-31).

User defined functions specific to the MMS implementation in MFIX are used to introduce the source term. Specifically, for each computational cell, equation (2-30) is evaluated and subtracted from the right hand side of the linear equation. Once the simulation has converged, the L_1, L_2 and L_∞ error norms are computed by referencing equation (2-28).

2.3.3 Results

Following the outline of MMS methodology, three separate 1-dimensional systems (x, y and z) were created, each having 8, 16, 32, 64, 128, and 256 cells, using the steady state heat equation and manufactured solution previously described.

An observed order for each direction is calculated using L_1, L_2 and L_∞ error norms. The following tables and figure illustrate these data. One can quickly see from the tabled L-norms and subsequently calculated observed order that direction does not have a large influence on these values. All data points to a 2nd order (p) convergence of the steady state heat equation using MFIX.

Hence, these data imply that the diffusion term engaged in the energy equation through the evaluation of the steady state heat equation is numerically closed on 2nd order approximations which is correct and *verified* by the method of manufactured solutions.

Table 2-3: Observed Order, *p*, for steady state heat equation using $U(x) = 501 + x^3$ on $0 \le x \le 5$.

Mesh Divisions	L_1-norm	L_2-norm	L_∞-norm	p (from L_1)	p (from L_2)	p (from L_∞)
8	7.3242E-01	8.4407E-01	1.3733E+00	N/A	N/A	N/A
16	1.8311E-01	2.1133E-01	3.5477E-01	2.0000	1.9979	1.9527
32	4.5776E-02	5.2852E-02	9.0122E-02	2.0000	1.9995	1.9769
64	1.1444E-02	1.3214E-02	2.2709E-02	2.0000	1.9999	1.9886
128	2.8610E-03	3.3036E-03	5.6997E-03	2.0000	2.0000	1.9943
256	7.1525E-04	8.2590E-04	1.4277E-03	2.0000	2.0000	1.9972

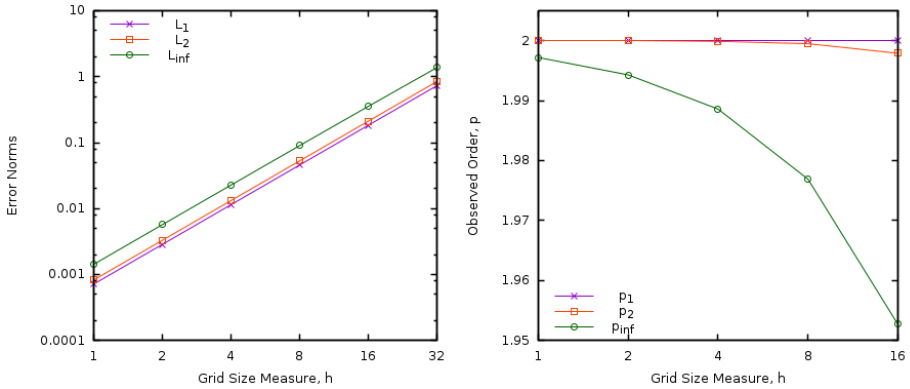

Figure 2-3: Observed Order, MMS Solution to 1-D steady state heat equation in MFIX, using $U(x) = 501 + x^3$ on $0 \le x \le 5$.

2.4 MMS-EX03: One dimensional transient heat equation

2.4.1 Description

Again consider the gas phase energy equations in MFIX given by equation (2-25) in the previous example. The energy equations can be recast as the 1-dimensional transient heat equation by imposing the following simplifying assumptions:

1. Calculations are restricted to one dimension.
2. The domain length in the x-axial direction is $x\epsilon[0,1]$.
3. The gas volume fraction, density, thermal conductivity, and specific heat are set to one, $\varepsilon_g = 1$, $\rho_g = 1$, $\kappa_g = 1$, and $C_{pg} = 1$.
4. The gas momentum equations are not solved and initial velocity field is set to zero so that the convective term is zero.
5. There are no chemical reactions, interphase mass transfer or other sources of energy implying: $\sum_{n=1}^{N_g} h_{gn} R_{gn} + \mathcal{S}_g = 0$.

On re-evaluation of the energy equations, the following one-dimensional form (aka the transient heat equation) emerges:

$$\frac{\partial T_g}{\partial t} - \frac{\partial^2 T_g}{\partial x^2} = 0 \tag{2-32}$$

Following the MMS approach, the partial differential equation is recast as:

$$L(x,t) = \frac{\partial T_g}{\partial t} - \alpha \frac{\partial^2 T_g}{\partial x^2} = 0 \tag{2-33}$$

As MMS requires the selection of a manufactured solution, a suitable analytic form of appropriate continuous, differential order is chosen. In this case, note that whatever manufactured solution is picked must be continuously differentiable through its second spatial derivative and first temporal derivative. In addition, for illustrative purposes, the manufactured solution is chosen so that time will appear in the boundary conditions. For simplicity, MMS-EX02 is modified by incorporating a time value, *t*, as:

$$T_g(x,t) = T_{g0} + T_{gx}\cos\left(A_{Tgx}\pi x\right) + T_{gt}\cos\left(A_{Tgt}\pi t\right) + T_{gtx}\cos\left(A_{Tgtx}\pi tx\right) \tag{2-34}$$

with a simple domain: $\{t \geq 0,\ \ 0 \leq x \leq 1\}$.

Then, this form is applied to $L(x,t)$:

$$L(x,t)_{T_g(x,t)} = \frac{\partial}{\partial t}T_g(x,t) - \alpha \frac{\partial^2}{\partial x^2}T_g(x,t) \tag{2-35}$$

$$\begin{aligned} L(x,t)_{T_g(x,t)} = &-T_{gt}\left(A_{Tgt}\pi\right)\sin\left(A_{Tgt}\pi t\right) - T_{gxt}\left(A_{Tgtx}\pi x\right)\sin\left(A_{Tgtx}\pi tx\right) \\ &+ \alpha T_{gx}\left(A_{Tgx}\pi\right)^2\cos\left(A_{Tgx}\pi x\right) \\ &+ \alpha T_{gtx}\left(A_{Tgtx}\pi\right)^2\cos\left(A_{Tgtx}\pi tx\right) L(x,t)_{U(x,t)} = (1+x^3) - 6\alpha xt \end{aligned} \tag{2-36}$$

Then, appropriate initial and/or boundary conditions are cast. For this case, an appropriate initial condition is:

$$T_g(x,0) = T_{g0} + T_{gx}\cos\left(A_{Tgx}\pi x\right) + T_{gt} + T_{gtx} \tag{2-37}$$

Focus then shifts to boundary conditions. On the spatial domain of interest: $x\epsilon[0,1]$, boundary conditions become:

$$\begin{aligned} T_g(0,t) &= T_{g0} + T_{gx} + T_{gt}\cos\left(A_{Tgt}\pi t\right) + T_{gtx} \\ T_g(1,t) &= T_{g0} + T_{gx}\cos\left(A_{Tgx}\pi\right) + T_{gt}\cos\left(A_{Tgt}\pi t\right) + T_{gtx}\cos\left(A_{Tgtx}\pi t\right) \end{aligned} \tag{2-38}$$

Note that these boundary conditions, while Dirichlet in nature, are dependent on time. The parameters chosen in the manufactured solution are summarized below:

Table 2-4: Parameters used in MMS applied to transient heat conduction

T_{g0}	500 K
T_{gx}	10 K
T_{gt}	100 K
T_{gtx}	10 K
A_{Tgx}	2.0
A_{Tgt}	2.0
A_{Tgtx}	2.0

2.4.2 Setup

This case is designed to test the energy equation implementation.

Computational/Physical model

1D, Steady-state, incompressible
Single-phase (no solids)
No gravity
Turbulence equations are not solved (Laminar)
Uniform mesh

Geometry

Coordinate system	Cartesian
Domain length, L	1.0 (m)

Material†

Fluid density, ρ_g	1.0 (kg·m^{-3})
Fluid viscosity, μ_g	1.0 (Pa·s)
Fluid specific heat, C_{pg}	1.0 (J·kg^{-1}·K^{-1})

Initial Conditions

Pressure *(gauge)*, P_g	0.0 (Pa)
Temperature, T_g	Set with user routine (K)

Boundary Conditions‡

East / West (x)	(MMS) (K)
All other boundaries	Adiabatic Walls

† Material properties selected to ensure comparable contribution from convection and diffusion terms.
‡ The manufactured solution imposed on the east / west boundaries is given by equation (2-38). In this case, because boundary conditions change with time, they must be managed by creating a user-defined function (in MFIX, update the standard function usr1.f).

User defined functions specific to the MMS implementation in MFIX are used to introduce the source term. Specifically, for each computational cell, equation (2-36) is evaluated and

subtracted from the right hand side of the linear equation. Once the simulation has converged, the L_1, L_2 and L_∞ error norms are computed using equation (2-34).

2.4.3 Analysis variation for mixed variable problems

When analyzing a problem where both transient and spatial order verification must be conducted simultaneously, care must be taken with problem set up. As a first step, to examine temporal order, spatial discretization must be held constant (fixed grid); then, to examine spatial order, temporal discretization must be held constant (fixed time step). Holding either discretization at a constant level introduces a fixed error that applies to all calculations in that group. In a problem such as this, one imagines discretization error as being in two parts:

$$DE = DE_{temporal} + DE_{spatial} \tag{2-39}$$

When one of these errors is constant, the normed error that is collected to represent overall discretization error contains that constant, albeit one cannot preconceive its value. For example, consider that time step is held constant, and that this choice results in constant temporal discretization error, k:

$$\|DE\| = \left\|k + DE_{spatial}\right\| \tag{2-40}$$

Note that the existence of k destroys the notion of equation (2-15) for calculating a one-variable observed order by masking $DE_{spatial}$. To eliminate the effect of k, observed order, $\hat{p}$, must be calculated in such a way as to naturally remove its presence. This can be done through subtraction as:

$$\hat{p} = \frac{ln\left(\frac{\|DE_{\ell+2}\| - \|DE_{\ell+1}\|}{\|DE_{\ell+1}\| - \|DE_{\ell}\|}\right)}{ln(r)} \tag{2-41}$$

with the caveat that at least 3 levels of spatial mesh are needed to isolate $\hat{p}$. Then, a similar calculation can be conducted by refining time step and using a fixed spatial mesh.

If the reader now allows themselves a *thought experiment*, they might be curious how error might manifest itself when the observed order associated with space and the observed order associated with time are equal or non-equal. If equal, and a naïve approach to order calculation is made, one might not detect that an analysis like (2-15) is invalid. However, when non-equal, the naïve approach will result in utter confusion. (Yes, we did it.)

To run a combined analysis without the above step where either temporal or spatial discretization is held constant, [10] provides a useful table illustrating refinement factors needed to accurately isolate observed order of spatially and temporally mixed problems in two discretization levels

instead of three, by assuring that the spatial and temporal discretization error terms are scaled together as solutions approach their asymptotic range. A portion of that table is given here, as it applies to the problem at hand, where the expectation is a spatial order of 2, and a temporal order of 1.

Table 2-5: Mixed analysis refinement factors [10]; highlighted row for expected spatial order =2, and expected temporal order = 1 based on known MFIX routines

Expected Spatial order p	Expected Temporal order q	Spatial refinement factor r_x	Temporal refinement factor r_t	Expected error reduction ratio (coarse/fine)
2	**1**	**2**	**4**	**4**
2	2	2	$\sqrt[2]{4}$	4
2	3	2	$\sqrt[3]{4}$	4
2	4	2	$\sqrt[4]{4}$	4

Likewise, Richards [11] summarily defines $r_t = (r_x)^{p/q}$. Using the suggestions from this table (formula) for an expected spatial order, $p = 2$, and an expected temporal order, $q = 1$, a calculated observed spatial order, $\hat{p}$, and a calculated observed temporal order, $\hat{q}$ are computed as described in [10]:

$$\hat{p} = \frac{ln\left(\frac{\|DE_{l+1}\|}{\|DE_l\|}\right)}{\ln(r_x)} \qquad \hat{q} = \frac{ln\left(\frac{\|DE_{l+1}\|}{\|DE_l\|}\right)}{\ln(r_t)} \tag{2-42}$$

In the following result section, the calculations derived from both methodologies are illustrated.

2.4.4 Results

Both methodologies described in section 2.4.3 were implemented to examine temporal and spatial orders of accuracy in the transient heat equation as it applies to MFIX.

Temporal order of accuracy

The temporal order of accuracy is determined by fixing the grid size and performing simulations by reducing the time step size. In this case, with spatial domain set to $x\epsilon[0,1]$, 16 cells were used corresponding to a coarse discretization. Expectation is that spatial error was significant.

The following time step sizes were used: 1.25E-4s, 6.25E-5s, 3.13E-5s, 1.56E-5s, 7.81E-6s, and 3.91E-6s, resulting in a refinement factor, *r*, equal to 2. The observed order of accuracy, $\hat{p}$, converges to 1 which is equal to the formal order of the first-order Euler time stepping method utilized in MFIX.

Table 2-6: L norms and the observed order for the unsteady heat equation – temporal order of accuracy[4]

h	L_1-norm	L_2-norm	L_∞-norm	$\hat{p}$ (from L_1)	$\hat{p}$ (from L_2)	$\hat{p}$ (from L_∞)
1	9.4156E-02	1.1189E-01	1.9267E-01	1.00	0.95	1.00
2	9.4175E-02	1.1182E-01	1.9260E-01	1.00	0.90	1.00
4	9.4214E-02	1.1168E-01	1.9244E-01	1.00	0.77	1.00
8	9.4291E-02	1.1143E-01	1.9214E-01	1.00	0.36	1.00
16	9.4444E-02	1.1101E-01	1.9153E-01	N/A	N/A	N/A
32	9.4751E-02	1.1047E-01	1.9031E-01	N/A	N/A	N/A

An example calculation, using h = 1, 2, 4 and L_1-norm is given:

$$\hat{p} = \frac{ln\left(\frac{\|DE_{\ell+2}\|-\|DE_{\ell+1}\|}{\|DE_{\ell+1}\|-\|DE_{\ell}\|}\right)}{ln(r)} = \frac{ln\left(\frac{9.4214\text{E-}02-9.4175\text{E-}02}{9.4175\text{E-}02-9.4156\text{E-}02}\right)}{ln\left(\frac{1.25\text{e-}4}{6.25\text{e-}5}\right)} = 1.00$$

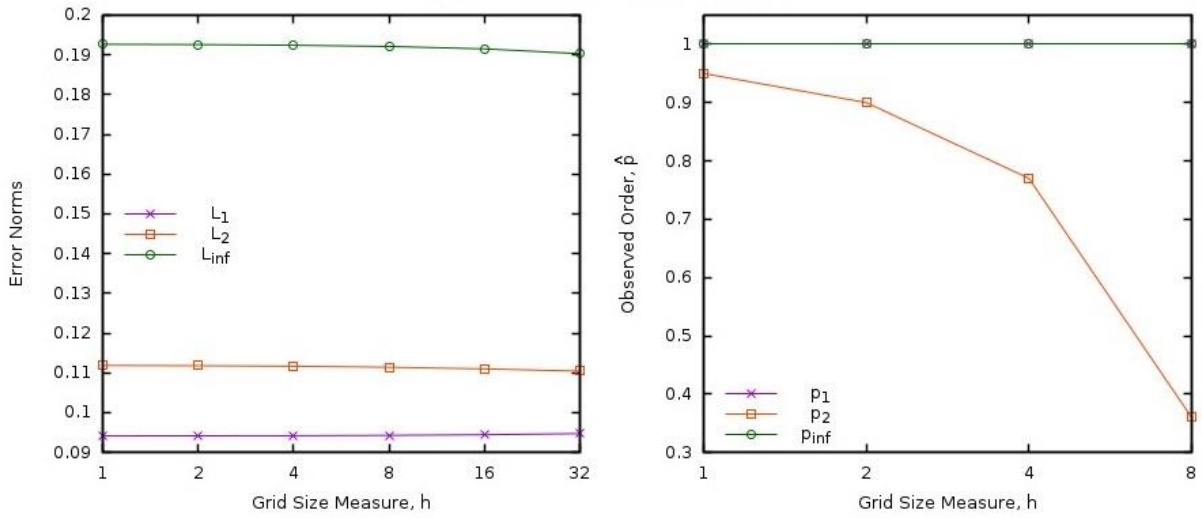

Figure 2-4: Observed Temporal Order of Accuracy, MMS Solution to 1-D transient heat equation in MFIX

Spatial order of accuracy

Likewise, spatial order of accuracy is estimated by maintaining a constant time step, 0.005s in this case. On a spatial domain of $x\epsilon[0,1]$, grid sizes were 3.12E-2m, 1.56E-2m, 7.81E-3m, 3.91E-3m and 1.95E-3m, resulting in a refinement factor, *r*, equal to 2. The observed order of accuracy, $\hat{p}$, converges to 2 which is equal to the formal order of the centered differencing scheme (diffusion term).

[4] Significant digits shown in table may not result in shown values of $\hat{p}$ because of round-off error. If the reader runs these simulations and holds all significant digits for calculation, $\hat{p}$ values will match those shown.

Table 2-7: L norms and the observed order for the unsteady heat equation – spatial order of accuracy[5]

h	L_1-norm	L_2-norm	L_∞-norm	$\hat{p}$ (from L_1)	$\hat{p}$ (from L_2)	$\hat{p}$ (from L_∞)
1	5.7762E-01	6.2875E-01	8.4644E-01	2.00	2.01	1.99
2	5.7783E-01	6.2884E-01	8.4627E-01	2.00	2.03	2.01
4	5.7867E-01	6.2920E-01	8.4559E-01	2.00	2.11	2.04
8	5.8204E-01	6.3068E-01	8.4285E-01	N/A	N/A	N/A
16	5.9554E-01	6.3708E-01	8.3158E-01	N/A	N/A	N/A

An example calculation, using h = 1, 2, 4 and L_1-norm is given:

$$\hat{p} = \frac{ln\left(\frac{\|DE_{\ell+2}\|-\|DE_{\ell+1}\|}{\|DE_{\ell+1}\|-\|DE_{\ell}\|}\right)}{ln(r)} = \frac{ln\left(\frac{5.7867\text{E-}01-5.7783\text{E-}01}{5.7783\text{E-}01-5.7762\text{E-}01}\right)}{ln\left(\frac{3.12\text{e-}2}{1.56\text{e-}2}\right)} = 2.00$$

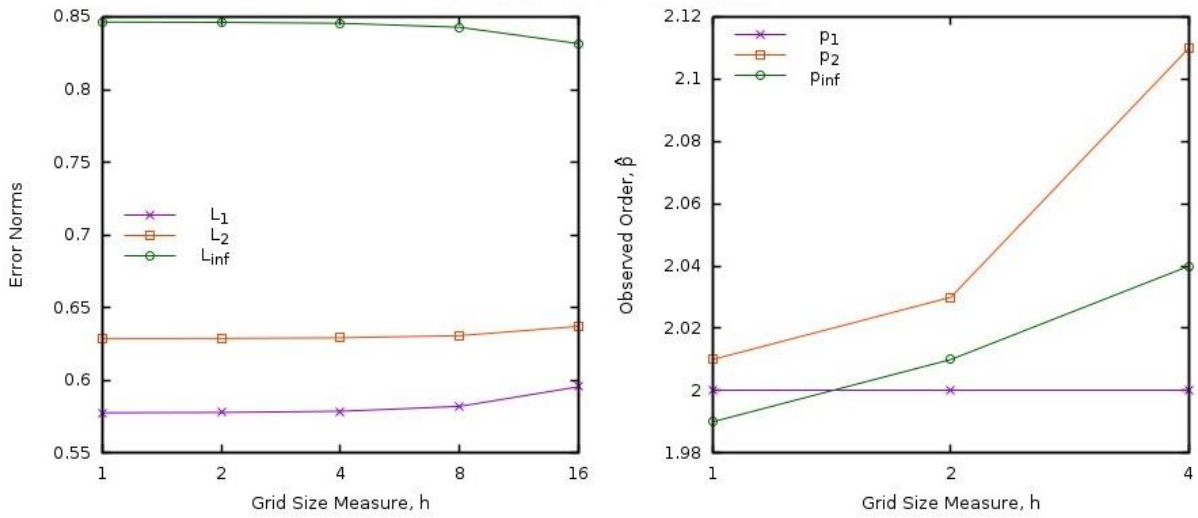

Figure 2-5: Observed Spatial Order of Accuracy, MMS Solution to 1-D transient heat equation in MFIX

Combined order analysis

Having tested temporal and spatial discretization independently, a combined order analysis is performed by choosing grid size, Δx, and time step size, Δt, according to the descriptions in section 2.4.3. Based on the observed order of accuracies, it can be concluded that the energy equation in MFiX is reduced to a Forward Time Centered Space numerical scheme. In such a case, the pertinent non-dimensional number is the Fourier number given by,

[5] Significant digits shown in table may not result in shown values of $\hat{p}$ because of round-off error. If the reader runs these simulations and holds all significant digits for calculation, $\hat{p}$ values will match those shown.

$$Fo = \alpha \frac{\Delta t}{\Delta x^2} \tag{2-43}$$

where α represents a diffusivity constant.

The stability criterion for a Forward Time Centered Space scheme is $Fo < {}^{1}/_{2}$. $Fo = 0.32$ was chosen in this study, while α is set to 1. The grid sizes used were 1.25E-1m, 6.25E-2m, 3.13E-2m, 1.56E-2m and 7.81E-3m. The corresponding time-step sizes are obtained as,

$$\Delta t = Fo \frac{\Delta x^2}{\alpha} \tag{2-44}$$

Note that this observation is in complete agreement with the table presented in section 2.4.3 where the analysis expectation is a problem with spatial order equal 2, and temporal order equal 1, thereby producing $r_t = (r_x)^{\frac{p}{q}} \rightarrow \Delta t = Fo(\Delta x)^{\frac{2}{1}}$.

The orders of accuracy were calculated using Equations (2-42). The tables below show that the results from combined order analysis are consistent with the individual verification tests, giving a calculated observed temporal order, $\hat{q} = 1$ and a calculated observed spatial order, $\hat{p} = 2$.

Regardless of temporal or spatial analysis, the calculated norms used in combined order analysis are identical. This idea is illustrated in the following figure and tables.

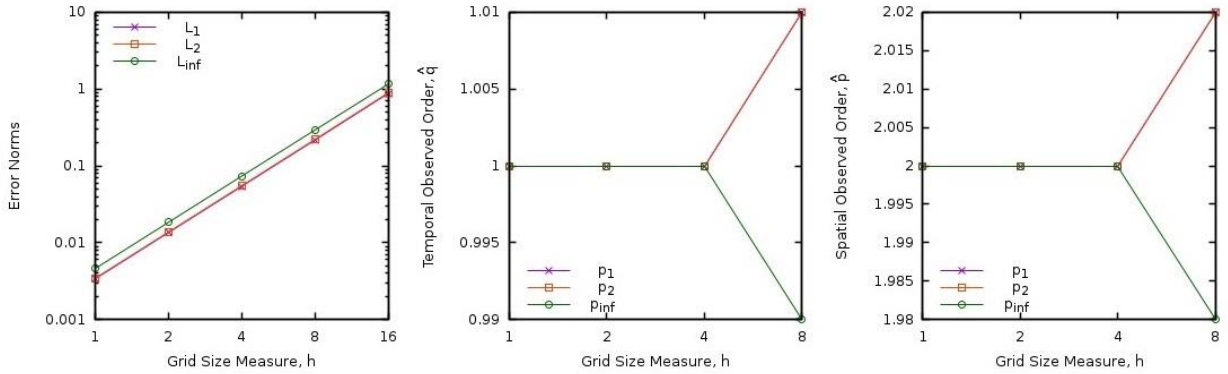

Figure 2-6: Observed Temporal and Spatial Orders of Accuracy using Combined order analysis, MMS Solution to 1-D transient heat equation in MFIX

The key difference in calculation is the management of the denominator (related to refinement factor) for $\hat{q}$ and $\hat{p}$. As explained previously, in this case, the refinement factor for time is $r_t = 4$, and the refinement factor for space is $r_x = 2$.

Table 2-8: L norms and the observed order in combined order analysis for the unsteady heat equation – temporal order of accuracy

h	L_1-norm	L_2-norm	L_∞-norm	$\hat{q}$ (from L_1)	$\hat{q}$ (from L_2)	$\hat{q}$ (from L_∞)
1	3.3848E-03	3.4552E-03	4.6133E-03	1.00	1.00	1.00
2	1.3542E-02	1.3823E-02	1.8453E-02	1.00	1.00	1.00
4	5.4204E-02	5.5336E-02	7.3780E-02	1.00	1.00	1.00
8	2.1741E-01	2.2202E-01	2.9422E-01	1.01	1.01	0.99
16	8.7873E-01	8.9901E-01	1.1638E+00	N/A	N/A	N/A

Table 2-9: L norms and the observed order in combined order analysis for the unsteady heat equation – spatial order of accuracy

h	L_1-norm	L_2-norm	L_∞-norm	$\hat{p}$ (from L_1)	$\hat{p}$ (from L_2)	$\hat{p}$ (from L_∞)
1	3.3848E-03	3.4552E-03	4.6133E-03	2.00	2.00	2.00
2	1.3542E-02	1.3823E-02	1.8453E-02	2.00	2.00	2.00
4	5.4204E-02	5.5336E-02	7.3780E-02	2.00	2.00	2.00
8	2.1741E-01	2.2202E-01	2.9422E-01	2.02	2.02	1.98
16	8.7873E-01	8.9901E-01	1.1638E+00	N/A	N/A	N/A

An example calculation, using h = 2 and 4, with L_1-norm is given:

$$\hat{q} = \frac{ln\left(\frac{5.4204\text{E-}02}{1.3542\text{E-}02}\right)}{ln(4)} = 1.00 \quad \text{and} \quad \hat{p} = \frac{ln\left(\frac{5.4204\text{E-}02}{1.3542\text{E-}02}\right)}{ln(2)} = 2.00$$

2.5 MMS01: Single-phase, 2D, sinusoidal functions

2.5.1 Description

A sinusoidal divergence-free manufactured solution [12, 13] for the fluid pressure, P_g, and x and y velocity components, u_g and v_g, respectively, is used for the verification of steady-state, single-phase flows on a 2D grid.

$$u_g = u_{g0} \sin^2\big(2\pi(x+y)\big) \tag{2-45.a}$$

$$v_g = v_{g0} \cos^2\big(2\pi(x+y)\big) \tag{2-45.b}$$

$$P_g = P_{g0} \cos\big(2\pi(x+y)\big) \tag{2-45.c}$$

Figure 2-4 shows a color contour of the pressure field and velocity streamlines for the manufactured solution using constants $P_{g0} = 100$ Pa, $u_{g0} = 5.0$ m·sec^{-1}, and , $v_{g0} = 5.0$ m·sec^{-1}.

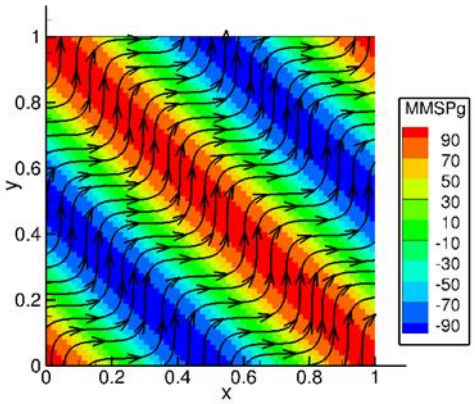

Figure 2-4: Pressure contours and velocity streamlines for 2D, single-phase, simple sinusoidal manufactured solution on a 64x64 cell grid.

2.5.2 Setup

Computational/Physical model

2D, Steady-state, incompressible
Single phase (no solids)
No gravity
Thermal energy equation is not solved
Turbulence equations are not solved (Laminar)
Uniform mesh
Superbee and Central discretization schemes

Geometry

Coordinate system	Cartesian
x-length	1.0 (m)
y-length	1.0 (m)

Material[†]

Fluid density, ρ_g	1.0 (kg·m^{-3})
Fluid viscosity, μ_g	1.0 (Pa·s)

Initial Conditions

Pressure *(gauge)*, P_g	0 (Pa)
x-velocity, u_g	5.0 (m·sec^{-1})
y-velocity, v_g	5.0 (m·sec^{-1})

Boundary Conditions[‡]

All boundaries	Mass inflow

[†] Material properties selected to ensure comparable contribution from convection and diffusion terms.
[‡] The manufactured solution is imposed on all boundaries (i.e., Dirichlet specification).

2.5.3 Results

Numerical solutions were obtained using both Superbee and Central discretization schemes for 8x8, 16x16, 32x32, 64x64, and 128x128 grid meshes. The Superbee scheme order of accuracy tests show a first-order rate of convergence for pressure under the L_∞ norm as illustrated in Figure 2-5(a), whereas the formal order for this scheme is two. The largest errors in pressure are local to boundary cells along the West (y=0) and South (x=0) edges of the domain as shown in Figure 2-6(a). This is an artifact of the staggered grid implementation in MFIX where only a single ghost cell layer is present along West and South boundaries, reducing higher-order upwind schemes to first-order. This effect also occurs along the Bottom (z=0) edge of the domain for three-dimensional simulations. Further investigation is needed to determine to what extent the errors introduced at the boundary propagate into the domain interior.

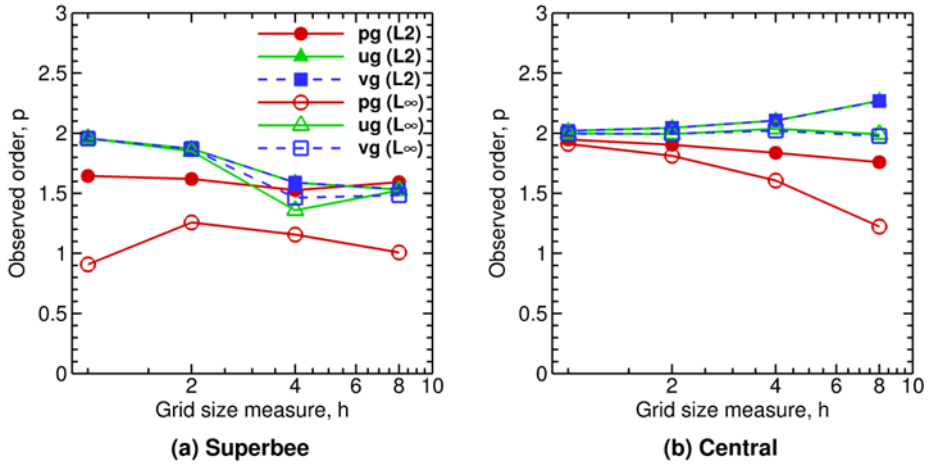

Figure 2-5: Observed orders of accuracy for 2D, single-phase, sinusoidal manufactured solution. (a) Superbee scheme, (b) Central scheme.

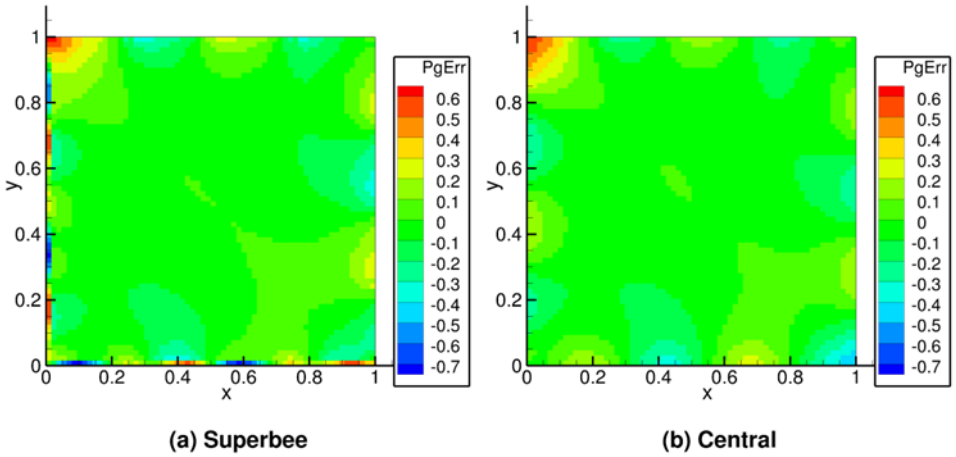

Figure 2-6: Errors in pressure for 2D, single-phase, sinusoidal manufactured solution for grid resolution (64x64). (a) Superbee scheme, (b) Central scheme

The Central scheme results, depicted in Figure 2-5(b), show second order accuracy for all variables. The formal order for the Central scheme is recovered because no up-winding is

performed, thereby averting solution deterioration at the boundaries. The errors in pressure near the boundaries are consistent with the scheme's formal order as can be seen from Figure 2-6(b).

2.5.4 Notes

During initial testing, it was discovered that the strain-tensor cross terms for the momentum equations were not calculated within steady-state sub-iterations which lead to large errors (not shown). These errors do not appear in cases with zero shear at the boundaries. Transient simulations recalculate these cross-terms at the start of each time-step making it difficult to determine the effect on the solution. The significance of this simplification (likely done to reduce computational expense) on real-world application problems is unknown and should be investigated. For MMS tests, this issue was circumvented by recalculating the cross-terms of the strain-tensor at each sub-iteration.

2.6 MMS02: Two-phase, 3D, curl-based functions with constant volume fraction

2.6.1 Description

Assuming that gas and solid volume fractions (i.e., ε_g and ε_s) remain constant, we can see from gas and solid continuity equations that both fluid and solid velocity fields are divergence-free (for constant density of fluid and solids). A manufactured solution for the fluid-phase velocity field is defined using the curl-based approach developed in [12]. For the solid-phase velocity field, a set of simple sinusoidal functions is selected (same as those shown in Eq. (2-45.a,b,c)). The manufactured solutions for scalar quantities (pressure, gas temperature, and solid temperature) can be multivariate functions of sines and cosines as defined in Appendix A Equation (A-1). The selected functions for all concerned variables are shown over a 3D domain in Figure 2-7 through Figure 2-9.

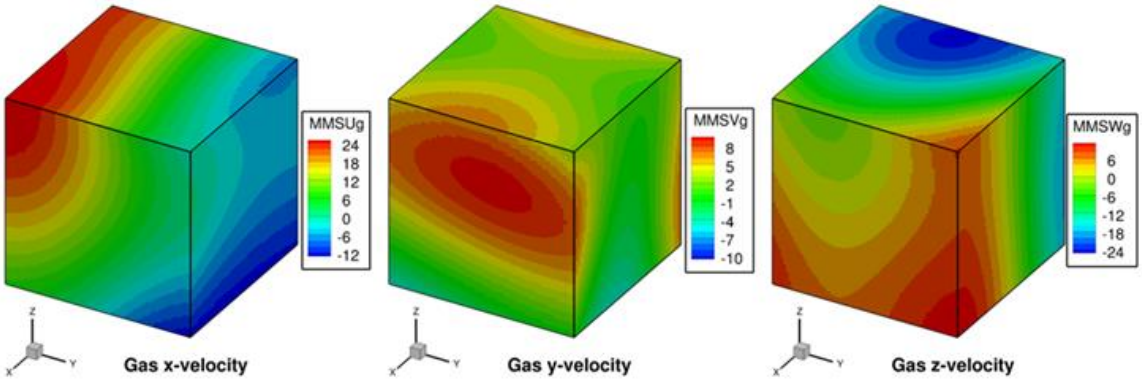

Figure 2-7: Gas phase momentum equation manufactured solutions for 3D, steady-state, two-phase flow verification test case.

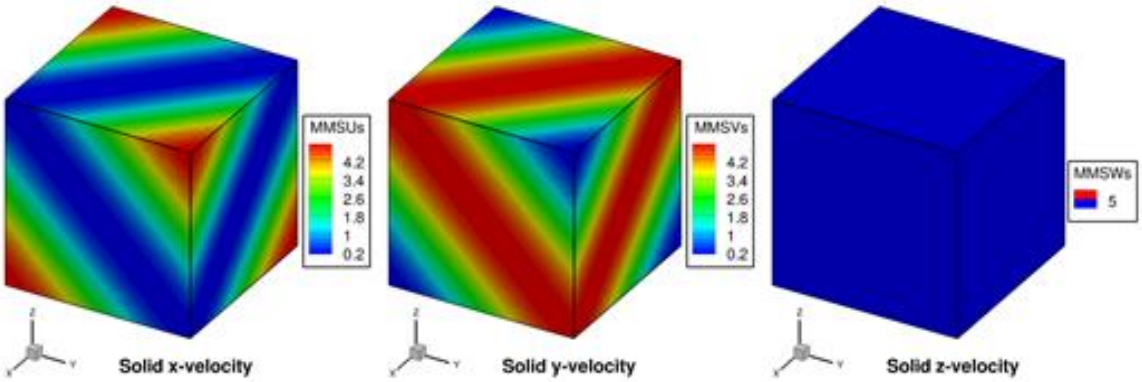

Figure 2-8: Solids phase momentum equation manufactured solutions for 3D, steady-state, two-phase flow verification test case.

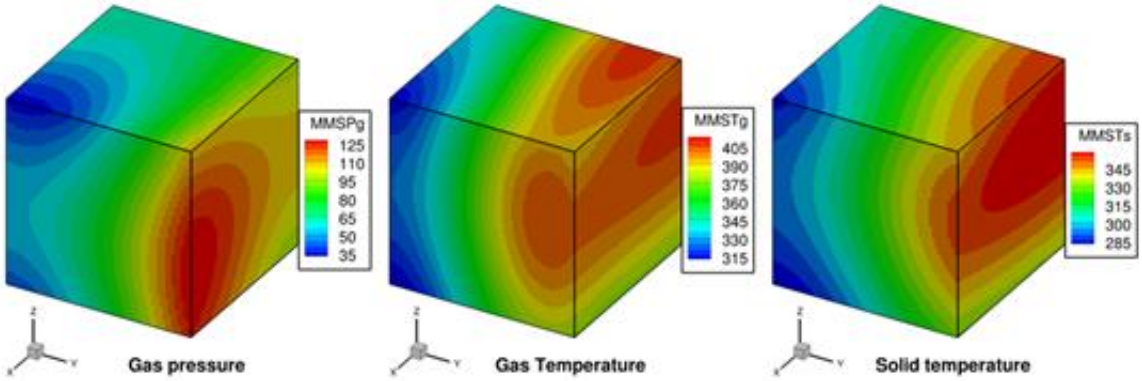

Figure 2-9: Scalar field manufactured solutions for 3D, steady-state, two-phase flow verification test case.

2.6.2 Setup

Computational/Physical model

3D, Steady-state, incompressible
Two-phase
No gravity
Drag model is turned off
Friction model is turned off
Thermal energy equations are solved
Granular energy equation is not solved
Turbulence equations are not solved (Laminar)
Central scheme

Geometry

Coordinate system	Cartesian
Domain length, L (x)	1.0 (m)
Domain height, H (y)	1.0 (m)
Domain width, W (z)	1.0 (m)

Material†

Fluid density, ρ_g	1.0 (kg·m^{-3})
Fluid viscosity, μ_g	1.0 (Pa·s)
Fluid specific heat, C_{pg}	0.05 (J·kg^{-1}·K^{-1})
Fluid thermal conductivity, k_g	1.0 (J·kg^{-1}·K^{-1}·s^{-1})
Solids density, ρ_s	2.0 (kg·m^{-3})
Solids viscosity, μ_s	2.0 (Pa·s)
Solids specific heat, C_{ps}	0.1 (J·kg^{-1}·K^{-1})
Solids thermal conductivity, k_s	2.0 (J·kg^{-1}·K^{-1}·s^{-1})

Initial Conditions

Pressure *(gauge)*, P_g	0.0 (Pa)
Fluid x-velocity, u_g	10.0 (m·sec^{-1})
Fluid y-velocity, v_g	10.0 (m·sec^{-1})
Fluid z-velocity, w_g	10.0 (m·sec^{-1})
Solids x-velocity, u_s	5.0 (m·sec^{-1})
Solids y-velocity, v_s	5.0 (m·sec^{-1})
Solids z-velocity, w_s	5.0 (m·sec^{-1})
Fluid temperature, T_g	350 (K)
Solids temperature, T_s	300 (K)
Gas volume fraction, ε_g	0.7 --

Boundary Conditions‡

All boundaries	Mass inflow

† Material properties selected to ensure comparable contribution from convection and diffusion terms. Specified values are constant to avoid the introduction of constitutive laws.

‡ The manufactured solution is imposed on all boundaries (i.e., Dirichlet specification).

2.6.3 Results

Numerical solutions were obtained using the Central discretization scheme for 8x8, 16x16, 32x32, 64x64, and 128x128 grid meshes. The observed order approaches second order for both L_2 and L_∞ norms using the Central scheme, as shown in Figure 2-10. This indicates that the numerical discretization terms have been implemented correctly for all derivative terms within the gas momentum equations, solid momentum equations, gas pressure correction equation, gas energy equation, and solid energy equation.

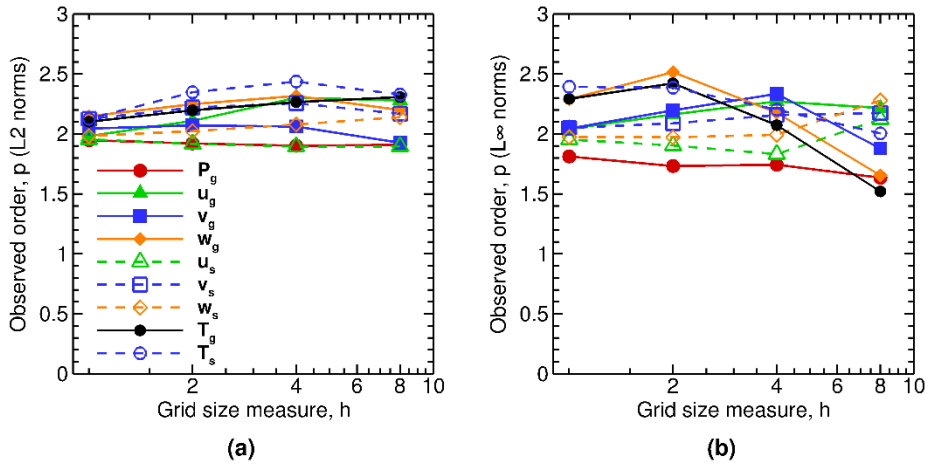

Figure 2-10: Observed orders of accuracy for 3D, two-phase flows (constant volume fraction) using (a) L_2 norms, and (b) L_∞ norms of the discretization error.

2.7 MMS03: Two-phase, 3D, curl-based functions with variable volume fraction

2.7.1 Description

The volume fraction is selected as a function with sufficient variation in all directions while ensuring that the packed bed volume fraction ($\varepsilon_g = 0.42$) is not reached. The velocity manufactured solutions are now selected to satisfy the continuity equations (not divergence-free velocity conditions as in Section 2.6). The resulting manufactured solutions for gas volume fraction and fluid velocity variables are shown in Figure 2-11. The mathematical form of the manufactured solutions is discussed in Appendix A.

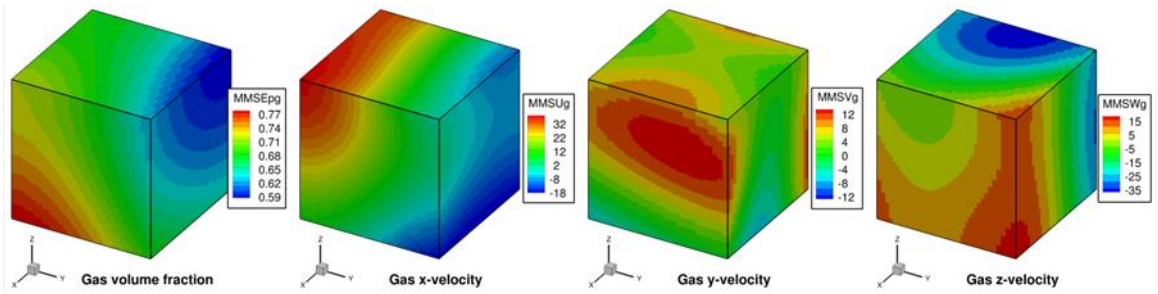

Figure 2-11: Manufactured solutions for 3D, variable volume fraction, two-phase verification.

2.7.2 Setup

Computational/Physical model

3D, Steady-state, incompressible
Two-phase
No gravity

Drag model is turned off
Friction model is turned off
Thermal energy equations are solved
Granular energy equation is not solved
Turbulence equations are not solved (Laminar)
Non-uniform mesh
Central scheme

Geometry

Coordinate system	Cartesian
Domain length, L (x)	1.0 (m)
Domain height, H (y)	1.0 (m)
Domain width, W (z)	1.0 (m)

Material[†]

Fluid density, ρ_g	1.0 ($kg \cdot m^{-3}$)
Fluid viscosity, μ_g	1.0 ($Pa \cdot s$)
Fluid specific heat, C_{pg}	0.05 ($J \cdot kg^{-1} \cdot K^{-1}$)
Fluid thermal conductivity, k_g	1.0 ($J \cdot kg^{-1} \cdot K^{-1} \cdot s^{-1}$)
Solids density, ρ_s	2.0 ($kg \cdot m^{-3}$)
Solids viscosity, μ_s	2.0 ($Pa \cdot s$)
Solids specific heat, C_{ps}	0.1 ($J \cdot kg^{-1} \cdot K^{-1}$)
Solids thermal conductivity, k_s	2.0 ($J \cdot kg^{-1} \cdot K^{-1} \cdot s^{-1}$)

Initial Conditions

Pressure *(gauge)*, P_g	MMS
Fluid x-velocity, u_g	10.0 ($m \cdot sec^{-1}$)
Fluid y-velocity, v_g	10.0 ($m \cdot sec^{-1}$)
Fluid z-velocity, w_g	10.0 ($m \cdot sec^{-1}$)
Solids x-velocity, u_s	5.0 ($m \cdot sec^{-1}$)
Solids y-velocity, v_s	5.0 ($m \cdot sec^{-1}$)
Solids z-velocity, w_s	5.0 ($m \cdot sec^{-1}$)
Fluid temperature, T_g	350 (K)
Solids temperature, T_s	300 (K)
Gas volume fraction, ε_g	MMS

Boundary Conditions[‡]

All boundaries	Mass inflow

[†] Material properties selected to ensure comparable contribution from convection and diffusion terms. Specified values are constant to avoid the introduction of constitutive laws.

[‡] The manufactured solution is imposed on all boundaries (i.e., Dirichlet specification).

2.7.3 Results

Numerical solutions were obtained using the Central discretization scheme for 8x8, 16x16, 32x32, 64x64, and 128x128 grid meshes. Iterative convergence was not achieved when continuity equations were solved with a variable volume fraction field. To achieve convergence, the continuity variables (ε_g, ρ_g', and P_g) were kept fixed by specifying the fields for these variables using the manufactured solution in the initial conditions routine, and discarding their iterative solution within the main solver routine. Thus, the continuity and pressure equations were not solved in this case. This restricts the ability to make any observations about the accuracy of these equations. The observed order of accuracy matches the formal order as shown in Figure 2-12 for both velocity and energy variables.

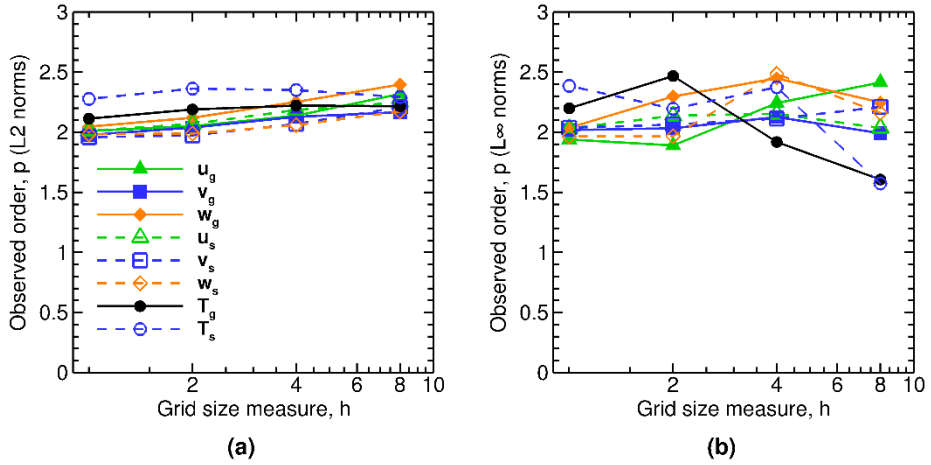

Figure 2-12: Observed orders of accuracy for 3D, two-phase flows (variable volume fraction) using (a) L_2 norms, and (b) L_∞ norms of the discretization error.

2.8 MMS04: No-slip wall BC, single-phase, 3D, curl-based functions

2.8.1 Description

The no-slip wall boundary condition in MFIX is verified using the techniques described in [12]; the manufactured solution is selected such that it satisfies both the divergence-free constraint and the no-slip wall boundary condition. Specifically, the no-slip wall boundary condition requires that the velocity at the (stationary) no-slip wall is zero. The manufactured solution is generated using the curl-based derivation to ensure divergence-free velocity fields [12] along with the technique given in [14] to ensure that the velocity component functions approach the value of zero at each boundary tested. The manufactured solution for the velocity field used for the verification of no-slip wall is given as [15]:

$$\vec{V} = S^2\left(\vec{\nabla} \times \vec{H}\right) + 2S\left(\nabla S \times \vec{H}\right) \tag{2-46}$$

where, $\vec{V}$ is the velocity field vector, S is the mathematical equation of the boundary being tested, and $\vec{H}$ is a general vector field consisting of sinusoidal expressions. The manufactured solution for pressure is selected as in Appendix A, Equation (A-1) since there are no constraints on pressure with this boundary condition.

2.8.2 Setup

This case is setup for single-phase flows on a domain with unit dimensions; the boundary tested is the West boundary (i.e., $x = 0$).

Computational/Physical model

3D, Steady-state, incompressible
Single-phase (no solids)
No gravity
Turbulence equations are not solved (Laminar)
Non-uniform mesh
Central scheme

Geometry

Coordinate system	Cartesian
Domain length, L (x)	1.0 (m)
Domain height, H (y)	1.0 (m)
Domain width, W (z)	1.0 (m)

Material†

Fluid density, ρ_g	1.0 (kg·m^{-3})
Fluid viscosity, μ_g	1.0 (Pa·s)

Initial Conditions

Pressure *(gauge)*, P_g	MMS
Fluid x-velocity, u_g	5.0 (m·sec^{-1})
Fluid y-velocity, v_g	5.0 (m·sec^{-1})
Fluid z-velocity, w_g	5.0 (m·sec^{-1})

Boundary Conditions‡

West boundary	No-slip wall
All other boundaries	Mass inflow (MMS)

† Material properties selected to ensure comparable contribution from convection and diffusion terms.
‡ The manufactured solution is imposed on all boundaries (i.e., Dirichlet specification).

2.8.3 Results

Numerical solutions were obtained using the Central discretization scheme for 8x8, 16x16, 32x32, 64x64, and 128x128 grid meshes. Iterative convergence was not achieved for this case

when pressure was solved. Hence, the pressure variable (P_g) was fixed by specifying pressure using the manufactured solution in the initial conditions routine and discarding the pressure solution in the main solver routine. The observed order of accuracy matches the formal order as shown in Figure 2-13 for the velocity variables.

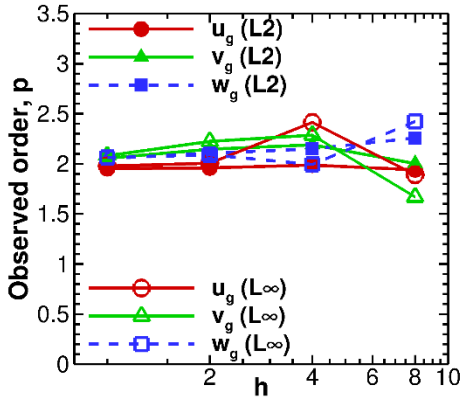

Figure 2-13: Observed orders of accuracy for no-slip wall verification (3D, single-phase flows) using L_2 and L_∞ norms of the discretization error.

2.9 MMS05: Free-slip wall BC, single-phase, 3D, curl-based functions

2.9.1 Description

The free-slip wall boundary condition in MFIX is verified using the techniques described in [12] where the manufactured solution is selected such that it satisfies both the divergence-free constraint and the free-slip wall boundary condition. Specifically, the normal velocity component is zero at the (stationary) free-slip wall while the tangential velocity component is imposed by specifying appropriate values in the ghost cells adjacent to the wall. This results in a zero gradient condition normal to the free-slip wall for the tangential velocity components only. The manufactured solution for the velocity field used for the verification of a free-slip wall is given as [15]:

$$\vec{V} = \vec{V}_0 + S^3\left(\vec{\nabla} \times \vec{H}\right) + 3S^2\left(\nabla S \times \vec{H}\right) \tag{2-47}$$

where, $\vec{V}$ is the velocity field vector, $\vec{V}_0 = \{0, v_0, w_0\}^T$ consists of non-zero scalar constants for v_0 and w_0, S is the mathematical equation of the boundary tested (i.e., $S \equiv x = 0$), and $\vec{H}$ is a general vector field consisting of sinusoidal expressions. The pressure manufactured solution is selected as in Appendix A, Equation (A-1) since there are no constraints on pressure with this boundary condition.

2.9.2 Setup

This case is setup for single-phase flows on a domain with unit dimensions; the boundary tested is the West boundary (i.e., $x = 0$).

Computational/Physical model

3D, Steady-state, incompressible
Single-phase (no solids)
No gravity
Turbulence equations are not solved (Laminar)
Non-uniform mesh
Central scheme

Geometry

Coordinate system	Cartesian
Domain length, L (x)	1.0 (m)
Domain height, H (y)	1.0 (m)
Domain width, W (z)	1.0 (m)

Material†

Fluid density, ρ_g	1.0 (kg·m^{-3})
Fluid viscosity, μ_g	1.0 (Pa·s)

Initial Conditions

Pressure *(gauge)*, P_g	MMS
Fluid x-velocity, u_g	5.0 (m·sec^{-1})
Fluid y-velocity, v_g	5.0 (m·sec^{-1})
Fluid z-velocity, w_g	5.0 (m·sec^{-1})

Boundary Conditions‡

West boundary	Free-slip wall
All other boundaries	Mass inflow (MMS)

† Material properties selected to ensure comparable contribution from convection and diffusion terms.
‡ The manufactured solution is imposed on all boundaries (i.e., Dirichlet specification).

2.9.3 Results

Numerical solutions were obtained using the Central discretization scheme for 8x8, 16x16, 32x32, 64x64, and 128x128 grid meshes. Iterative convergence could not be achieved for this case when pressure was solved. Hence, the pressure variable (P_g) was fixed by specifying pressure using the manufactured solution in the initial conditions routine and discarding the pressure solution in the main solver routine. The observed order of accuracy matches the formal order as shown in Figure 2-14 for the velocity variables.

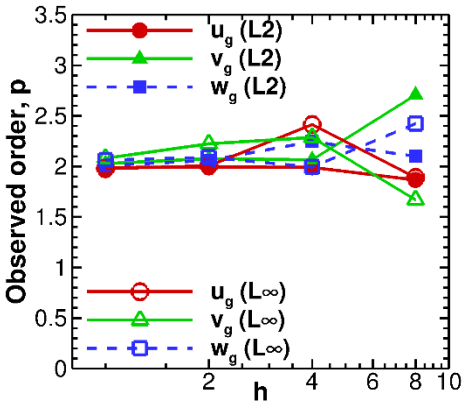

Figure 2-14: Observed orders of accuracy for free-slip wall verification (3D, single-phase flows) using L_2 and L_∞ norms of the discretization error.

2.10 MMS06: Pressure outflow BC, single-phase, 3D, curl-based functions

2.10.1 Description

The pressure outflow boundary condition in MFIX is verified using the techniques described in [12] where the manufactured solution is selected such that it satisfies both the divergence-free constraint and the pressure outflow condition. Specifically, this boundary condition requires that the pressure and all velocity components at the outflow have zero gradients normal to the wall at the boundary. For verification of the pressure outflow condition, the manufactured solution for the velocity field is given by Equation (2-48) while that for pressure is given by Equation (2-49) [15].

$$\vec{V} = \vec{V}_0 + S^3\left(\vec{\nabla} \times \vec{H}\right) + 3S^2\left(\nabla S \times \vec{H}\right) \tag{2-48}$$

$$P = P_0 + S^2 P_1 \tag{2-49}$$

Here, $\vec{V}$ is the velocity field vector, S is the mathematical equation of the boundary tested (here, $S \equiv y = 1$), P_0 is a non-zero scalar constant, P_1 represents the sinusoidal terms of the general manufactured solution, and $\vec{H}$ is a general vector field consisting of sinusoidal expressions.

2.10.2 Setup

This case is setup for single-phase flows on a domain with unit dimensions; the boundary tested is the North boundary (i.e., $y = 1$).

Computational/Physical model

3D, Steady-state, incompressible
Single-phase (no solids)
No gravity

Turbulence equations are not solved (Laminar)
Non-uniform mesh
Central scheme

Geometry

Coordinate system	Cartesian
Domain length, L (x)	1.0 (m)
Domain height, H (y)	1.0 (m)
Domain width, W (z)	1.0 (m)

Material†

Fluid density, ρ_g	1.0 ($kg \cdot m^{-3}$)
Fluid viscosity, μ_g	1.0 ($Pa \cdot s$)

Initial Conditions

Pressure *(gauge)*, P_g	0.0 (Pa)
Fluid x-velocity, u_g	5.0 ($m \cdot sec^{-1}$)
Fluid y-velocity, v_g	5.0 ($m \cdot sec^{-1}$)
Fluid z-velocity, w_g	5.0 ($m \cdot sec^{-1}$)

Boundary Conditions‡

North boundary	Pressure outflow
All other boundaries	Mass inflow (MMS)

† Material properties selected to ensure comparable contribution from convection and diffusion terms.
‡ The manufactured solution is imposed on all boundaries (i.e., Dirichlet specification).

2.10.3 Results

Numerical solutions were obtained using the Central discretization scheme for 8x8, 16x16, 32x32, 64x64, and 128x128 grid meshes. The observed order of accuracy matches the formal order as shown in Figure 2-15 for both the velocity variables and the pressure. Unlike the test cases verifying the no-slip and free-slip boundary conditions, no convergence issues were encountered since the problem has a physically-realistic outflow boundary.

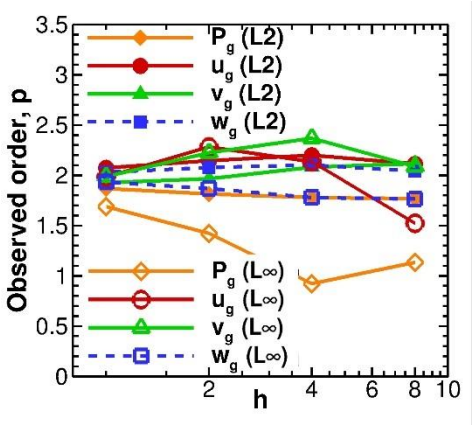

Figure 2-15: Observed orders of accuracy for pressure outflow verification using L_2 and L_∞ norms of the discretization error.

Chapter 3: Fluid Model Code Verification Test Cases

The test cases presented in this chapter for the MFIX fluid solver are summarized in Table 3-1. Test cases were selected based on the criteria for verification test selection outlined in Chapter 1. All cases are executed in serial mode unless explicitly noted.

Table 3-1: Summary of MFIX-FLD tests by feature

	Frequency†	Reference Dataset‡	Dimension	Momentum	Thermal Energy	Species Mass	Turbulence	Spatial Discretization										Distributed Memory	Shared Memory
								FOUP	FOUP w/DWF	Superbee	SMART	ULTRA-QUICK	QUICKEST	MUSCL	van Leer	Minmod	Central		
FLD01	C	A	2D	✓						✓									
FLD02	C	A	1D		✓					✓									
FLD03	C	P	2D	✓						✓								✓	
FLD04	C	A	2D	✓				✓		✓	✓		✓	✓	✓	✓	✓		
FLD05		A	2D	✓						✓									
FLD06		A	2D	✓		✓					✓								
FLD07		P	2D	✓			✓			✓									
FLD08		P	2D	✓			✓			✓									
FLD09		P	2D	✓			✓			✓									

† C-Incorporated into the continuous integration server; M-Monthly; Q-Quarterly; X-Manual; D-Disabled

‡ A-Analytical solution; P-Published benchmark data; R-Regression data from previous code versions

3.1 FLD01: Steady, 2D Poiseuille flow

3.1.1 Description

Plane Poiseuille flow is defined as a steady, laminar flow of a viscous fluid between two horizontal parallel plates separated by a distance, H. Flow is induced by a pressure gradient across the length of the plates, L, and is characterized by a 2D parabolic velocity profile symmetric about the horizontal mid-plane as illustrated in Figure 3-1.

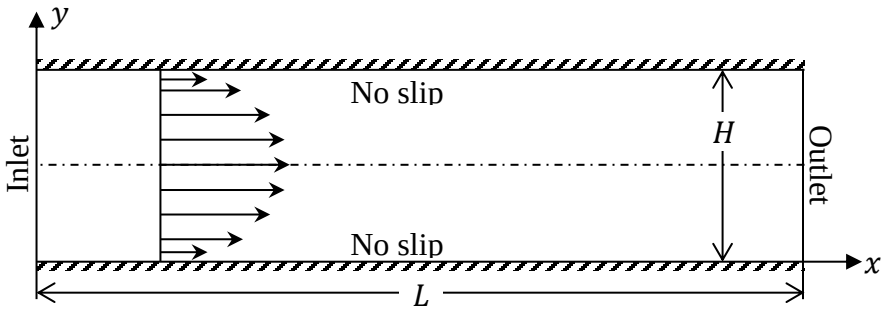

Figure 3-1: Plane Poiseuille flow between two flat plates of length L, separated by a distance H.

In this problem, the Navier-Stokes equations reduce to a second order, linear, ordinary differential equation (ODE),

$$\mu_g \frac{d^2 u_g}{dy^2} = \frac{dP_g}{dx}, \tag{3-1}$$

where μ_g and P_g are correspondingly the fluid viscosity and pressure, and u_g and v_g are respectively the x and y velocity components. Furthermore, it is assumed that gravitational forces are negligible, the pressure gradient is constant, i.e., $dP_g/dx = C$, and all velocity components are zero at the channel walls. The resulting analytical solution to (3-1) is given as

$$u_g(y) = -\frac{dP_g}{dx}\frac{1}{2\mu_g} y(H - y). \tag{3-2}$$

3.1.2 Setup

Computational/Physical model

2D, Steady-state
Single phase (no solids)
No gravity
Thermal energy equation is not solved
Turbulence equations are not solved (Laminar)
Uniform mesh
Superbee discretization scheme

Geometry

Coordinate system	Cartesian	Grid partitions
Channel length, L (x)	0.2 (m)	8, 16, 32, 64
Channel height, H (y)	0.01 (m)	8, 16, 32, 64

Material

Fluid density, ρ_g	1.0 (kg·m^{-3})
Fluid viscosity, μ_g	0.001 (Pa·s)

Initial Conditions

Pressure *(gauge)*, P_g	101325 (Pa)
x-velocity, u_g	10.0 (m·sec^{-1})
y-velocity, v_g	0.0 (m·sec^{-1})

Boundary Conditions

South boundary	0.0 (m·s^{-1})	No-Slip wall
North boundary	0.0 (m·s^{-1})	No-Slip wall
Cyclic West-East boundary with pressure drop, ΔP_g	240.0 (Pa)	

3.1.3 Results

The analytical and numerical solutions for x-velocity, u_g, are shown in Figure 3-2. Only a subset of the numerical solution data points are plotted causing the appearance of a slight shift in presented data points. The observed error demonstrates a second-order rate of convergence with respect to grid size in the y-axial direction. This is attributed to the second-order discretization of the viscous stress term as convection/diffusion terms do not contribute to the solution.

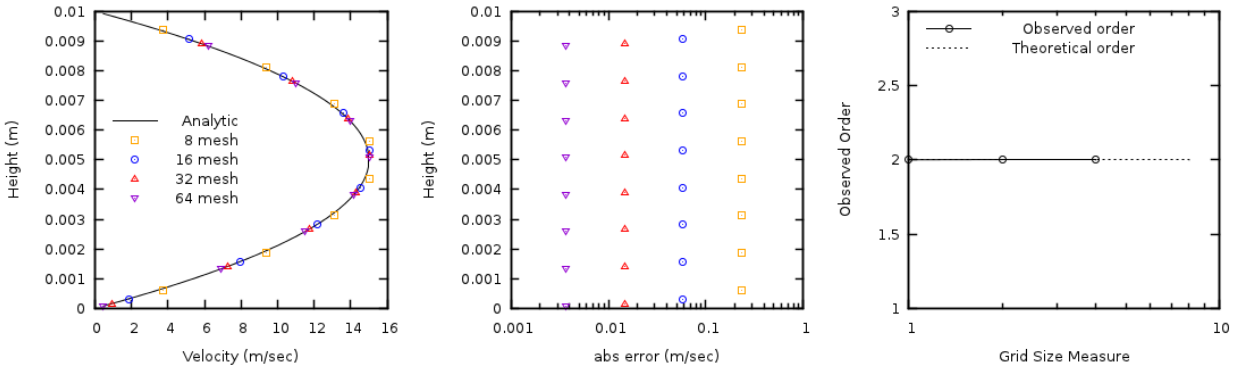

Figure 3-2: Steady, 2D channel flow x-velocity profile (left), absolute error in x-velocity solution (center), and observed order of accuracy (right) using four grid levels (JMAX = 8, 16, 32, 64).

The fluid pressure, P_g, varies linearly along the length of the plates as shown in Figure 3-3. The largest observed absolute error is bounded above by 10^{-12} and occurs for the finest mesh. This error is attributed to the convergence criteria of the linear equation system.

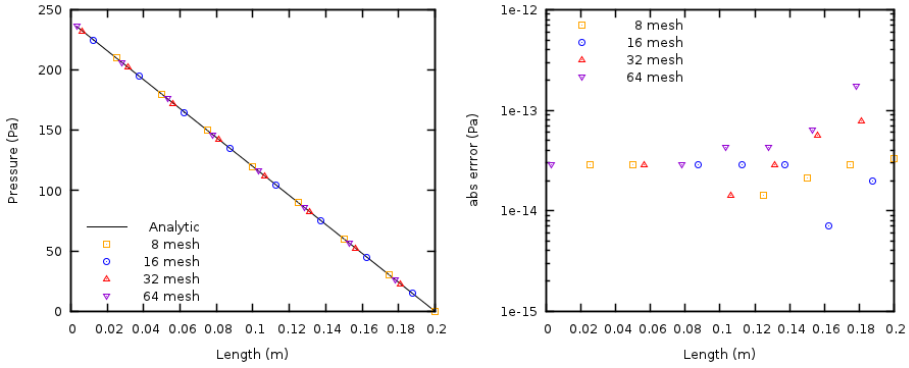

Figure 3-3: Steady, 2D channel flow pressure profile (left) and absolute error in pressure solution (right) using four grid levels (IMAX = 8, 16, 32, 64).

3.2 FLD02: Steady, 1D heat conduction

3.2.1 Description

Steady-state, one-dimensional heat conduction occurs across a rectangular plane-shaped slab of length *L* with constant material properties. As shown in Figure 3-4, two opposing slab boundaries are maintained at constant temperatures. All other faces are perfectly insulated such

that the heat flux along these boundaries is zero. Without heat generation, heat transfer through the $x = 0$ face must equal that through the $x = L$ face.

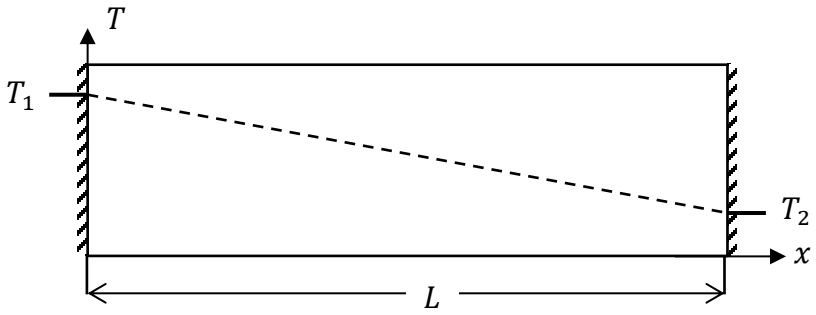

Figure 3-4: Plane-shaped slab with constant material properties and no internal heat generation is shown with constant temperatures specified on opposing faces. The slab is assumed to be perfectly insulated along all other faces.

For constant thermal conductivity, the energy equation reduces to a second order ODE with Dirichlet boundary conditions as given by Eq. (3-3). The analytical solution for temperature distribution within the slab follows a line as given by Eq. (3-4).

$$\frac{d}{dx}\left(\lambda_g \frac{dT}{dx}\right) = 0; \quad T(x=0) = T_1; \quad T(x=L) = T_2 \tag{3-3}$$

$$T(x) = T_1 + \frac{(T_2 - T_1)}{L} x \tag{3-4}$$

3.2.2 Setup

Computational/Physical model

1D, Steady-state
Single phase (no solids)
No gravity
Momentum equations are not solved
Thermal energy equation is solved
Uniform mesh
Superbee discretization scheme

Geometry

Coordinate system	Cartesian	Grid partitions
Slab length, L (x)	1.0 (m)	8, 16, 32, 64
Slab height, H (y)	1.0 (m)	1

Material

Thermal conductivity, λ_g	1.0 ($W \cdot m^{-1} \cdot K^{-1}$)

Initial Conditions

Temperature, T_g	350.0 (K)	

Boundary Conditions

West boundary	400.0 (K)	Constant temperature
East boundary	300.0 (K)	Constant temperature
North/South boundaries	0.0 ($J \cdot s^{-1} \cdot m^{-2}$)	Constant heat flux

3.2.3 Results

The analytical and numerical solutions for temperature, T_g, are shown in Figure 3-5. Only a subset of the numerical solution data points are plotted causing the appearance of a slight shift in presented data points. The largest observed absolute error is bounded above by 10^{-12} and occurs for the finest mesh. This error is attributed to convergence criteria of the linear equation solver.

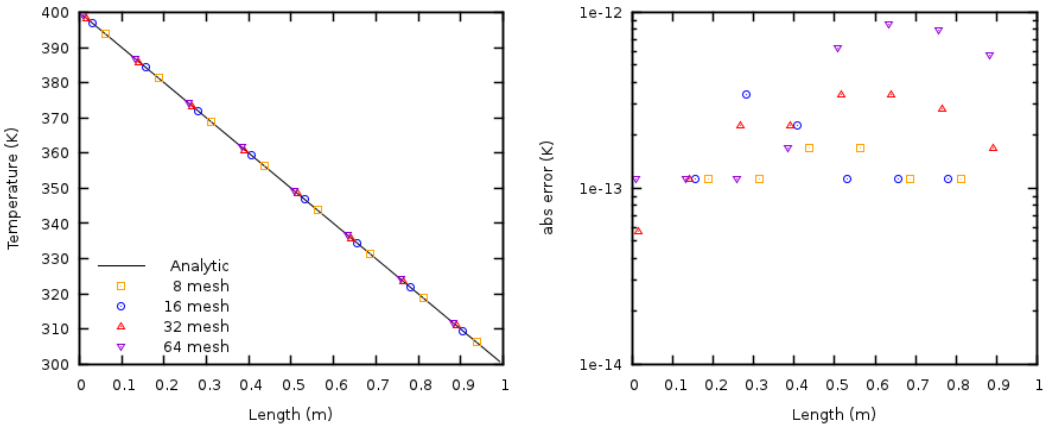

Figure 3-5: Steady, 1D heat-conduction. (Left) numerical solution vs analytical solution, and (right) absolute error between the analytical and numerical solutions.

3.3 FLD03: Steady, lid-driven square cavity

3.3.1 Description

Lid-driven flow in a 2D square cavity in the absence of gravity is illustrated in Figure 3-6. The problem definition follows the work of Ghia et al. [16] where the domain is bounded on three sides with stationary walls while one wall, the lid, is prescribed a constant velocity. The cavity is completely filled with a fluid of selected viscosity and the flow is assumed to be incompressible and laminar.

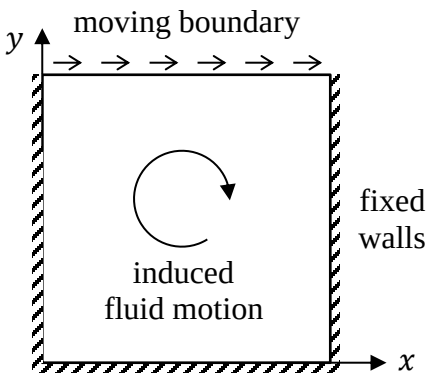

Figure 3-6: Schematic of the lid-driven square cavity.

3.3.2 Setup

Computational/Physical model

2D, Pseudo steady-state, incompressible
Single phase (no solids)
Turbulence equations are not solved (i.e., Laminar)
Uniform mesh
Superbee discretization scheme

Geometry

Coordinate system	Cartesian	Grid partitions
Cavity length, L (x)	1.0 (m)	128
Cavity width, W (y)	1.0 (m)	128

Material

Fluid density, ρ_g	1.0 (kg·m^{-3})
Fluid viscosity, μ_g	*varied* (Pa·s)

Initial Conditions

x-velocity, u_g	-0.01 (m·s^{-1})
y-velocity, v_g	0.00 (m·s^{-1})

Boundary Conditions

North boundary	1.0 (m·s^{-1})	Partial slip wall
East, West, South boundaries	0.0 (m·s^{-1})	No-slip wall

3.3.3 Results

Numerical solutions were obtained on a 128x128 grid mesh for Reynolds numbers of 100 and 400 by specifying fluid viscosities of 1/100 and 1/400 Pa·s, respectively. A time step of 0.01 second was used and the simulations considered converged when the average L_2 Norms for the x-axis and y-axis velocity components, u_g and v_g, were less than 10^{-8}.

The horizontal velocity at the vertical centerline ($x = 0.5$) and the vertical velocity at the horizontal centerline ($y = 0.5$) are compared with those of Ghia et al. [16] in Figure 3-7 and Figure 3-8.

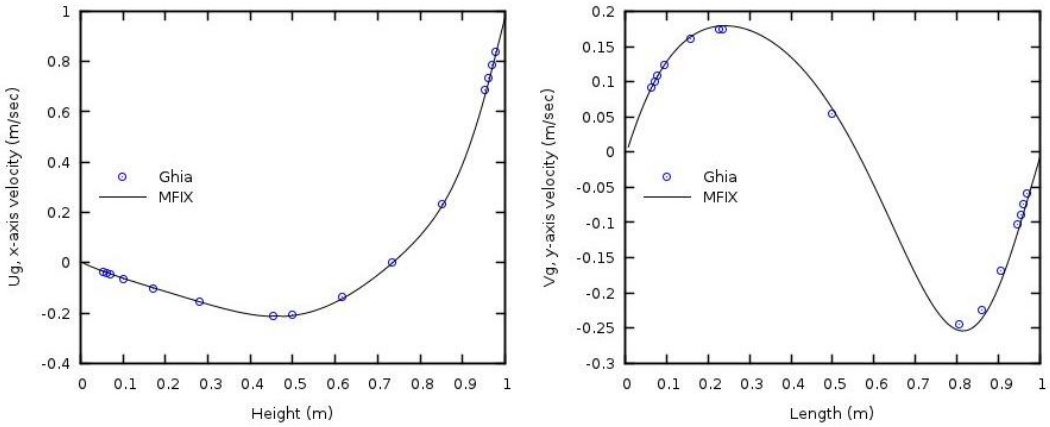

Figure 3-7: Comparison of velocities at the vertical (x=0.5) and horizontal centerlines (y=0.5) of the cavity with Ghia et al. [16] for Reynolds number of 100 (128x128 grid).

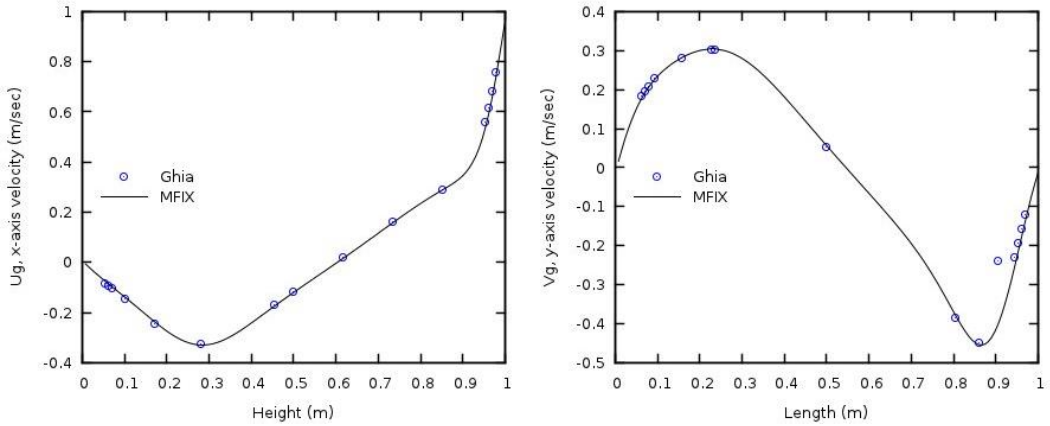

Figure 3-8: Comparison of velocities at the vertical (x=0.5) and horizontal centerlines (y=0.5) of the cavity with Ghia et al. [16] for Reynolds number of 400 (128x128 grid).

Similarly, numerical solutions were obtained on a 128x128 grid mesh for Reynolds numbers of 1000 and 3200 by specifying fluid viscosities of 1/1000 and 1/3200 Pa·s, respectively. The horizontal velocity at the vertical centerline ($x = 0.5$) and the vertical velocity at the horizontal centerline ($y = 0.5$) are compared with those of Ghia et al. [16] in Figure 3-9 and Figure 3-10. These cases are not included in the continuous integration server test suite.

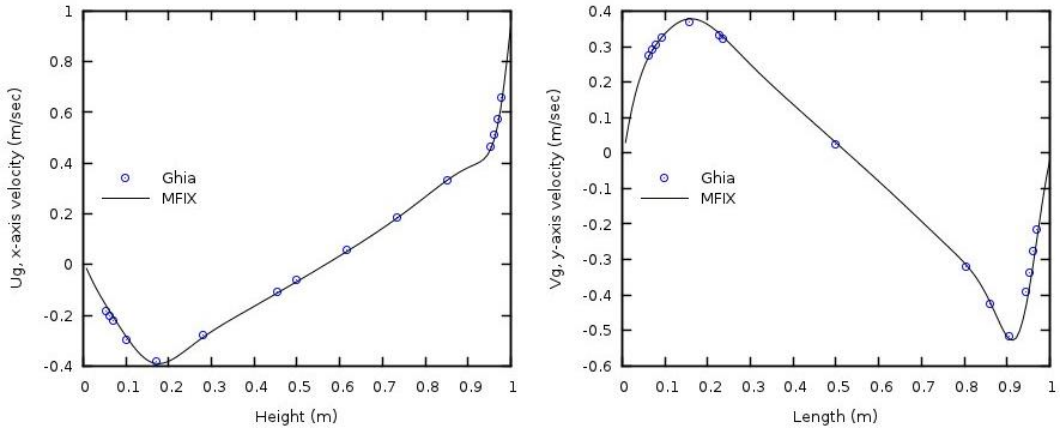

Figure 3-9: Comparison of velocities at the vertical (x=0.5) and horizontal centerlines (y=0.5) of the cavity with Ghia et al. [16] for Reynolds number of 1000 (128x128 grid).

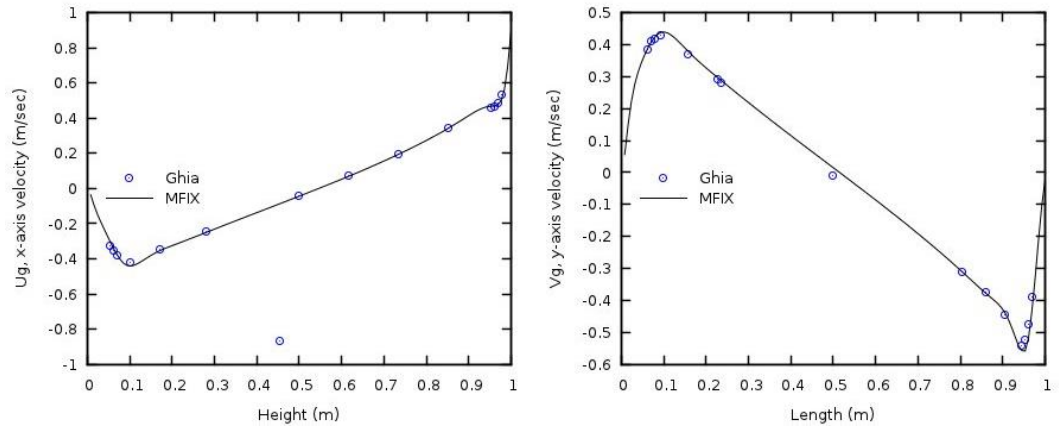

Figure 3-10: Comparison of velocities at the vertical (x=0.5) and horizontal centerlines (y=0.5) of the cavity with Ghia et al. [16] for Reynolds number of 3200 (128x128 grid).

3.4 FLD04: Gresho vortex problem

3.4.1 Description

The Gresho vortex problem [17] involves a stationary rotating vortex for which the centrifugal forces are exactly balanced by pressure gradients. The angular velocity and pressure distribution varies with radius as given by Eq. (3-5) [18] while the radial velocity is zero everywhere and the density is one everywhere.

$$u_\phi(r) = \begin{cases} 5r \\ 2 - 5r \\ 0 \end{cases}, \qquad p(r) = \begin{cases} 5 + 12.5r^2 & 0 \le r < 0.2 \\ 9 - 4\ln 0.2 + {}^{25}/_{2}\, r^2 - 20r + 4\ln r & 0.2 \le r < 0.4 \\ 3 + 4\ln 2 & 0.4 \le r \end{cases} \quad (3\text{-}5)$$

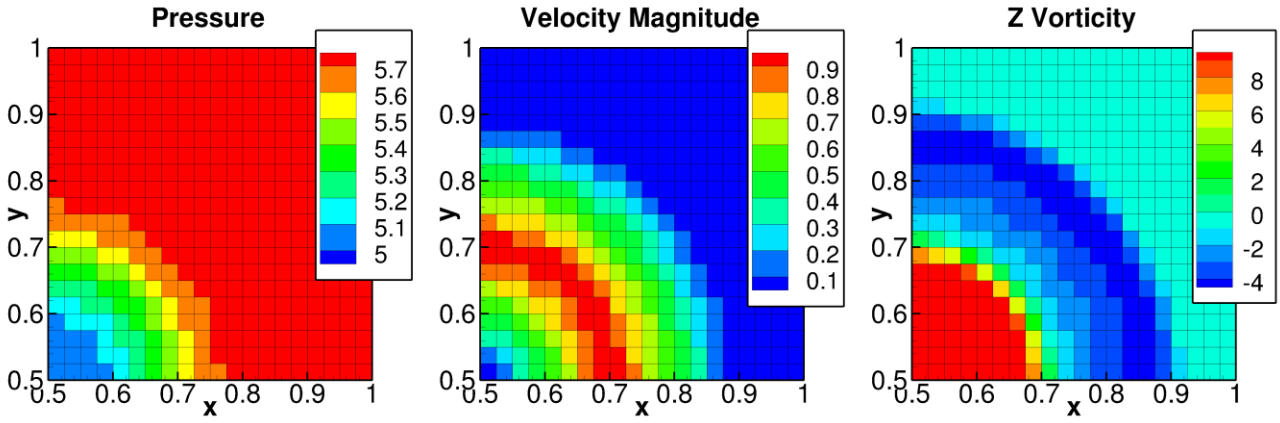

Figure 3-11: Exact solution for the Gresho vortex problem (shown for $(x, y) \in (0.5, 1) \times (0.5, 1)$)

This problem is setup as a time-independent solution to the incompressible, homogeneous Euler equations. The exact solution is symmetric about the horizontal and the vertical axes and is shown for the quadrant of $(x, y) \in (0.5,1) \times (0.5,1)$ in Figure 3-11, where $(0.5,0.5)$ is the center of the vortex. The simulation is initialized with the exact solution and periodic conditions on all boundaries of a 2D domain of unit dimensions (i.e., $(x, y) \in (0,1) \times (0,1)$)). Different numerical schemes in MFIX are used to find the numerical solution after three seconds which are then compared with an exact solution to assess the quality of the results.

3.4.2 Setup

Computational/Physical model

2D, Unsteady, incompressible
Single phase (no solids)
No gravity
Turbulence equations are not solved (i.e., laminar flow)
Viscosity is zero (i.e., inviscid flow)
Uniform mesh
Different discretization schemes:
FOUP, Smart, Superbee, Quickest, VanLeer, Muscl, Minmod, Central
Grid: (imax=40, jmax=40)

Geometry

Coordinate system	Cartesian
Domain length, L (x)	1.0 (m)
Domain width, W (y)	1.0 (m)

Time-stepping

Initial time	0.0 (s)
Final time	3.0 (s)
Time step	0.01 (s)

Variable time-stepping disabled.

Material

Fluid density, ρ_g	1.0 (kg·m^{-3})
Fluid viscosity, μ_g	0.0 (Pa·s)

Initial Conditions

x-velocity, u_g	(set using Eq. (3-5))
y-velocity, v_g	(set using Eq. (3-5))
Pressure, p_g	(set using Eq. (3-5))

Boundary Conditions

All boundaries	Cyclic BC

3.4.3 Results

MFIX simulations of the Gresho vortex problem were carried out with nine spatial discretization schemes. The final flow vorticity is illustrated in Figure 3-12 with the exact vorticity provided for reference at left. FOUP and FOUP using downwind factors are identical as expected, therefore only results for FOUP are shown. FOUP clearly fails to capture the vorticity distribution over the entire domain; Minmod and QUICKEST fail to accurately capture this distribution in the region of 0.1 m $\leq r \leq$ 0.3 m (e.g., $0.6m \leq x \leq 0.8m$ along $y = 0.5$).

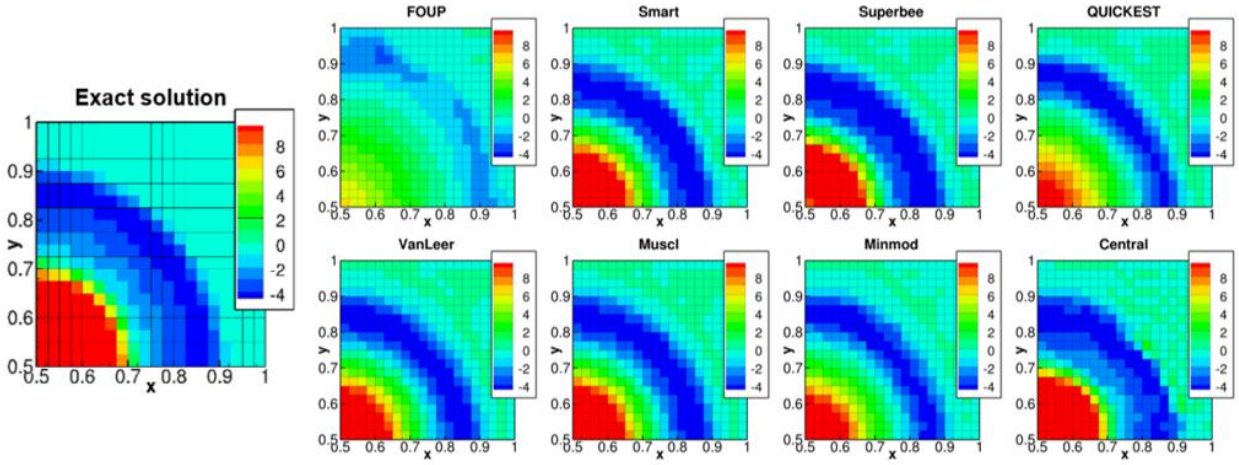

Figure 3-12: Comparison of vorticity by different numerical schemes with the exact solution (at $T = 3$ s).

The total kinetic energy of the flow is included in Table 3-2. FOUP has the greatest loss of kinetic energy, followed by QUICKEST, and Minmod. Central scheme maintains the best agreement followed by SMART and MUSCL.

Table 3-2: Total kinetic energy of the flow field compared to the exact (initial) value for various spatial discretization schemes.

Scheme	Calculated TKE	Absolute Error	Percent Relative Error
FOUP	42.64	91.25	68.15
FOUP w/DWF	42.64	91.25	68.15
Superbee	144.57	10.66	7.69
SMART	130.46	3.44	2.57
QUICKEST	93.47	40.43	30.19
MUSCL	128.45	5.45	4.07
van Leer	125.79	8.11	6.05
Minmod	112.95	20.94	15.64
Central	133.70	0.20	0.15

As a final measure of solution accuracy, the average L_2 Norm is shown in Table 3-3. Again, FOUP, QUICKEST, and Minmod demonstrate greatest amount of solution error whereas Central, SMART, and Superbee have the least amount of error.

Table 3-3: Average L2 Norms for the gas pressure (Pg), x-axial velocity (Ug) and y-axial velocity (Vg) for various spatial discretization schemes.

Scheme	Pg L_2-Norm	Ug L_2-Norm	Vg L_2-Norm
FOUP	0.1430	0.1468	0.1468
FOUP w/DWF	0.1430	0.0822	0.0822
Superbee	0.0184	0.0182	0.0182
SMART	0.0078	0.0163	0.0163
QUICKEST	0.0647	0.0612	0.0612
MUSCL	0.0109	0.0200	0.0200
van Leer	0.0149	0.0107	0.0107
Minmod	0.0343	0.0408	0.0408
Central	0.0076	0.0161	0.0161

3.5 FLD05: Steady, 2D Couette flow

3.5.1 Description

Couette flow is a laminar flow of a viscous fluid between two parallel plates separated by a distance, H, with the upper wall moving at velocity, U. Different velocity distributions are obtained depending on the pressure gradient applied to the flow field. The schematic of the problem is shown in Figure 3-13.

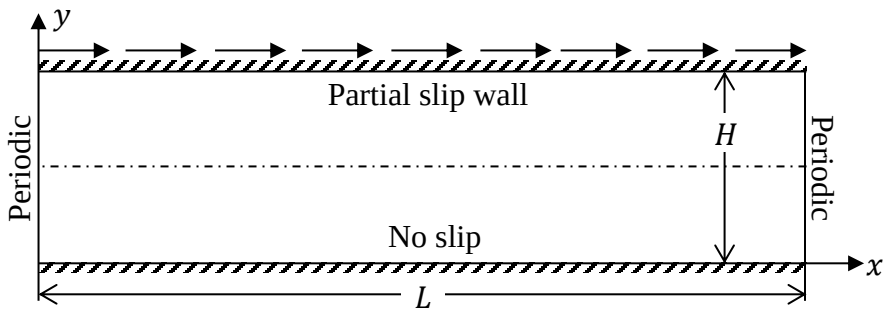

Figure 3-13: Couette flow between two flat plates of length L, separated by a distance H with the upper wall moving at velocity U.

In this problem, the Navier-Stokes equations reduce to a second order, linear, ordinary differential equation (ODE),

$$\frac{d^2 u_g}{dy^2} = \frac{1}{\mu_g}\frac{dp}{dx} \tag{3-6}$$

where μ_g is the fluid viscosity, and dp/dx is the prescribed pressure drop across the length of the pipe. The no-slip and partial-slip boundary conditions are specified by

$$\begin{aligned} u_g(0) &= 0, \\ u_g(H) &= U. \end{aligned} \tag{3-7}$$

The analytical solution is given by,

$$u_g(y) = \frac{1}{2\mu}\frac{dp}{dx}(y^2 - yH) + U\frac{y}{H} \tag{3-8}$$

where the non-dimensional pressure gradient P is defined as,

$$P = -\frac{H^2}{2\mu_g}\frac{dp_g}{dx}. \tag{3-9}$$

3.5.2 Setup

Computational/Physical model

2D, Unsteady, incompressible
Single phase (no solids)
No gravity
Turbulence equations are not solved (i.e., laminar flow)
Uniform mesh
Different grids: imax=4, jmax=8,16,32,64
Discretization scheme: Superbee

Geometry

Coordinate system	Cartesian
Domain length, L (x)	1.00 (m)
Domain width, W (y)	0.01 (m)

Material		
Fluid density, ρ_g	1.0 (kg·m^{-3})	
Fluid viscosity, μ_g	5.0E-06 (Pa·s)	
Initial Conditions		
x-velocity, u_g	0.0 (m·s^{-1})	
y-velocity, v_g	0.0 (m·s^{-1})	
Boundary Conditions		
North wall	10.0 (m·s^{-1})	Partial-slip wall
South wall	0.0 (m·s^{-1})	No-slip wall
East and west boundaries	Cyclic	Specified pressure drop

3.5.3 Results

Simulations were conducted for seven pressure drops, $[-3.0, -2.0, -1.0,\ 0.0, 1.0, 2.0, 3.0]$ Pa, specified across the x-axial cyclic boundaries. Four mesh levels [8, 16, 32, 64] in the y-axial direction were used to assess discretization error.

The analytical and numerical solutions for the zero pressure drop case are shown in Figure 3-14. For clarity, only a subset of the numerical solutions is presented, resulting in a slight offset/shift in displayed data points. Note that the analytical solution reduces to a linear variation in velocity between the lower and upper walls when the specified pressure drop is zero. For this case, the absolute error in velocity is bounded above by 10^{-6} m·sec^{-1} and is observed for the finest grid resolution (64 mesh). Further investigation (not presented) indicated that the increase in numerical error is attributed to the solution mechanism of the linear equation system. This error can be reduced by modifying the default linear equation solver settings (e.g., tighten convergence criteria, increase number of iterations, etc.).

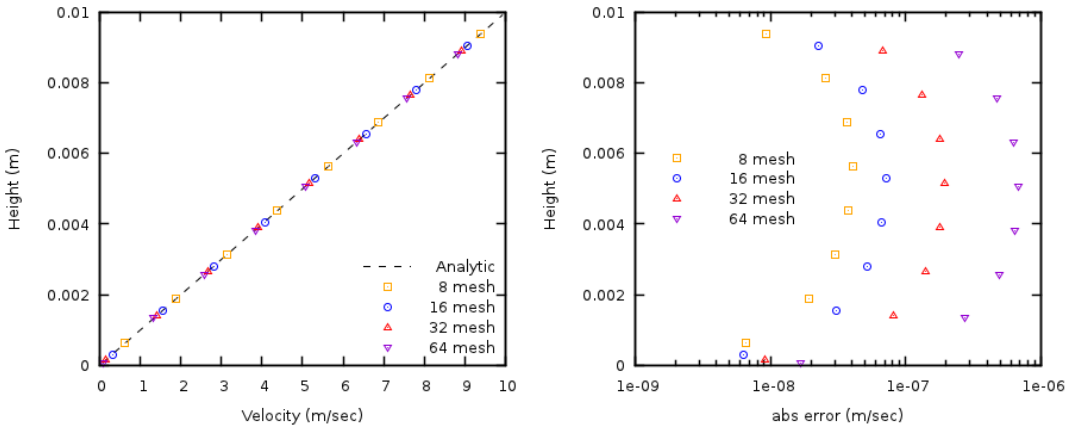

Figure 3-14: Couette flow with a zero pressure gradient with four grid resolutions.

The analytical and numerical solutions for the adverse and favorable pressure drops are shown in Figure 3-15 and Figure 3-16. Again, only a subset of the numerical solutions is presented resulting in a slight offset/shift in displayed data points. These cases demonstrate a second order rate of convergence with respect to grid size which is attributed to the second-order discretization of the viscous stress term.

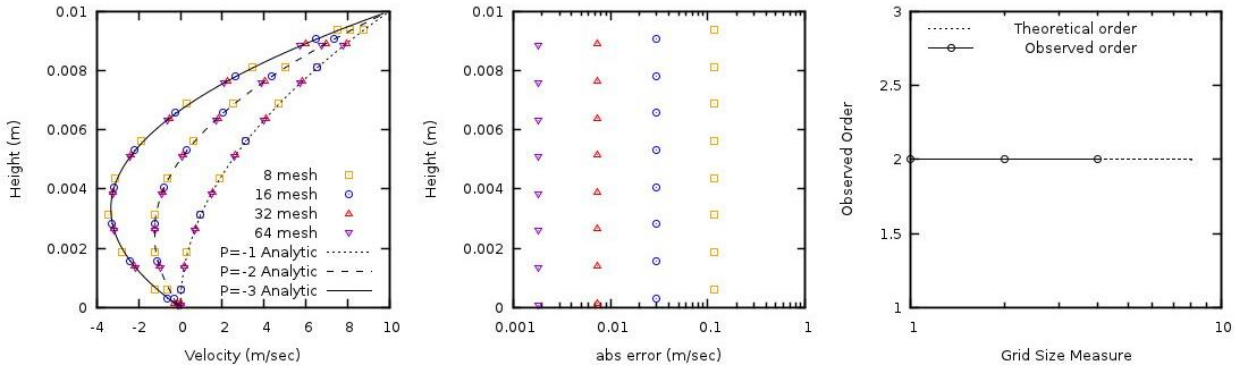

Figure 3-15: Adverse pressure gradient (-1, -2, -3 Pa) Couette flow with four grid resolutions. Absolute error and observed order of accuracy only shown for -3 Pa pressure gradient.

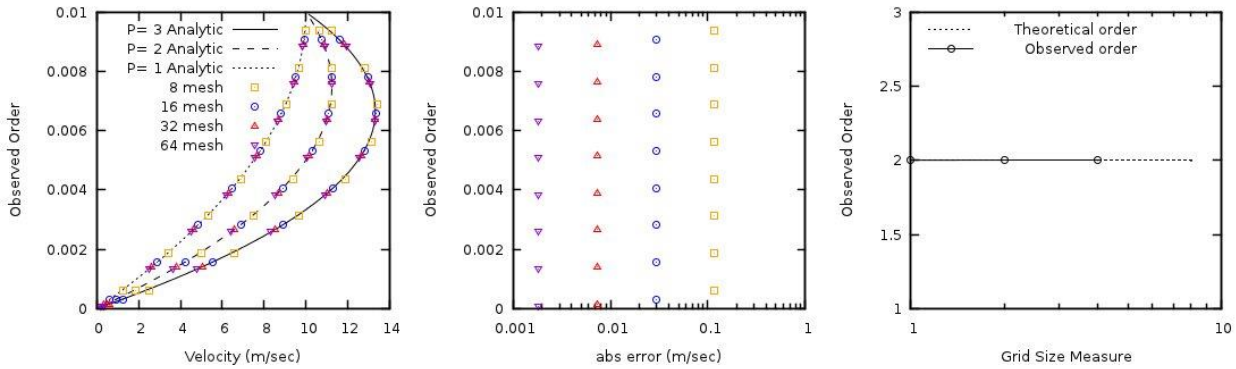

Figure 3-16: Favorable pressure gradient (1, 2, 3 Pa) Couette flow with four grid resolutions. Absolute error and observed order of accuracy only shown for 3 Pa pressure gradient.

3.6 FLD06: Steady, 2D multi-component species transport

3.6.1 Description

The 2D multi-component species problem investigates the transport of three non-reacting fluid phase species that follow ideal gas behavior. Illustrated in Figure 3-17, three separate mass inflows are used to inject three distinct gas species into the system. The species mix as the fluid passes through the domain such that they are well-mixed when the fluid reaches the outlet. The resulting species mass fractions, X_{gi}, for the well-mixed flow are given analytically by,

$$X_{gi} = \frac{MW_{gi}}{\sum_k MW_{gk}} \tag{3-10}$$

where MW_{gi} is the molecular weight of the i^{th} gas phase species.

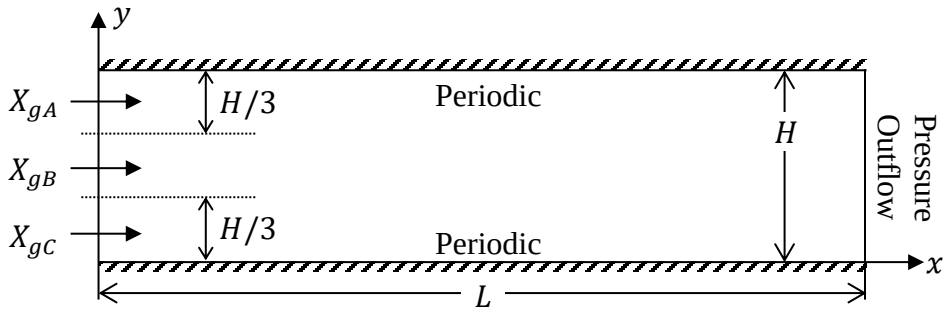

Figure 3-17: Multicomponent species transport.

3.6.2 Setup

Computational/Physical model

2D, Unsteady, incompressible
Single phase with three species (no solids)
No gravity
Turbulence equations are not solved (i.e., laminar flow)
Uniform mesh
Grid size: imax=200, jmax=3
Time step: 0.01 sec (fixed)
Discretization scheme: SMART with χ correction

Geometry

Coordinate system	Cartesian
Domain length, L (x)	2.0 (m)
Domain width, W (y)	0.03 (m)

Material

Fluid density, ρ_g	*Ideal gas law* (kg·m^{-3})
Fluid viscosity, μ_g	*Sutherlands law* (Pa·s)

Species Molecular Weight

Species A	1.0 (kg·kmol^{-1})
Species B	5.0 (kg·kmol^{-1})
Species C	25.0 (kg·kmol^{-1})

Initial Conditions

x-velocity, u_g	0.00 (m·s^{-1})
y-velocity, v_g	0.00 (m·s^{-1})
Species A Mass fraction, X_{gA}	0.03
Species B Mass fraction, X_{gB}	0.27
Species C Mass fraction, X_{gC}	0.70

Boundary Conditions		
West wall mass inflow 1	0.25 ($m \cdot s^{-1}$)	Specified velocity
Location	$[0, H/3]$ (m)	
Species A, X_{gA}	1.0	
Species A, X_{gB}	0.0	
Species A, X_{gC}	0.0	
West wall mass inflow 2	0.25 ($m \cdot s^{-1}$)	Specified velocity
Location	$[H/3,2H/3]$ (m)	
Species A, X_{gA}	0.0	
Species A, X_{gB}	1.0	
Species A, X_{gC}	0.0	
West wall mass inflow 3	0.25 ($m \cdot s^{-1}$)	Specified velocity
Location	$[2H/3, H]$ (m)	
Species A, X_{gA}	0.0	
Species A, X_{gB}	0.0	
Species A, X_{gC}	1.0	
North and South walls	Cyclic	
East wall	Pressure Outflow	

3.6.3 Results

The simulation was performed using the SMART discretization scheme with the χ correction to ensure species conservation. The average L_2 norm for the three species mass fractions were calculated for consecutive time steps. The simulation was considered converged when all three norms were less than 10^{-8}. The species mass fractions at the outflow plane and the L_2 norm between the MFIX and analytical solution are shown in Table 3-4. Two additional simulations were carried out where the solution order of the species equations was varied (e.g., ABC, BCA, CAB). No dependence was found on the solution order of the species equations (results not shown).

Table 3-4: Average species mass fractions at the outflow and average L_2 Norms between the analytical and MFIX species mass fraction for the well-mixed fluid.

Species	MFIX	L_2 Norm
A	0.027778	5.86e-7
B	0.277776	2.07e-6
C	0.694446	1.48e-6

3.7 FLD07: Steady, 2D fully-developed, turbulent channel flow

3.7.1 Description

This case uses 2D, fully-developed turbulent channel flow between two horizontal, parallel plates separated by a width, W, to assess the single phase *k-ϵ* model in MFIX. Periodic

boundaries with a specified pressure drop are imposed in the y-direction as shown in Figure 3-18.

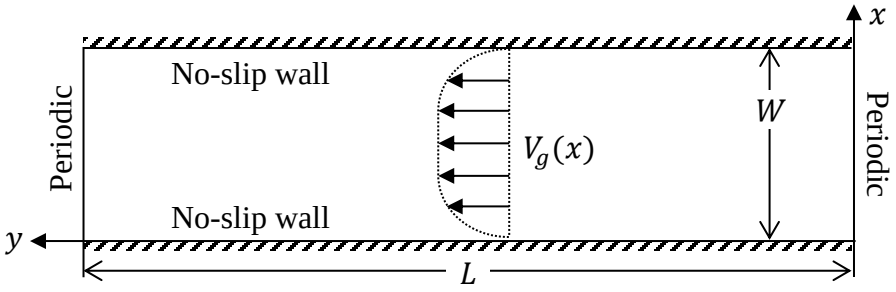

Figure 3-18: Turbulent flow in a 2D channel

The pressure drop along the channel is equated to the shear stress at the walls, τ_w.

$$W\frac{dP_g}{dy} = 2\tau_w \tag{3-11}$$

The shear stress is related to the gas density, ρ_g, and friction velocity, v_*,

$$\tau_w = \rho_g v_*^2, \tag{3-12}$$

where, the friction velocity, is given by the Reynolds number.

$$Re_\tau = \frac{\rho_g v_* (W/2)}{\mu_g} \tag{3-13}$$

3.7.2 Setup

Computational/Physical model

2D, unsteady, incompressible
Single phase (no solids)
No gravity
Thermal energy equation is not solved
Turbulent, *k-ϵ* model
Uniform mesh
Time step: 0.02 s
Discretization scheme: Superbee

Geometry

Coordinate system	Cartesian	Grid partitions
Domain width, W (x)	2.0 (m)	6, 12, 18
Domain length, L (y)	1.0 (m)	4

Material

Fluid density, ρ_g	1.0 (kg·m^{-3})
Fluid viscosity, μ_g	1.0E-04 (Pa·s)

Initial Conditions		
x-velocity, u_g	0.00 (m·s^{-1})	
y-velocity, v_g	0.00 (m·s^{-1})	
Turbulent kinetic energy, k_g	0.01 (m^2 s^{-2})	
Turbulence dissipation rate, ϵ_g	0.01 (m^2 s^{-3})	
Boundary Conditions		
West boundary	0.0 (m·s^{-1})	No-slip wall
East boundary	0.0 (m·s^{-1})	No-slip wall
Cyclic North-South boundary with pressure drop, ΔP_g	2.95E-3 (Pa)	

3.7.3 Results

The pressure drop in the y-axial direction, domain length and width, and gas density were chosen to reflect the conditions of Lee and Moser [19] for $Re_\tau = 543$. The DNS dataset was accessed on November 10, 2016 from http://turbulence.ices.utexas.edu/channel2015/data/LM_Channel_0550_mean_prof.dat.

Transient simulations were performed for better numerical stability. The solution was considered converged when the L_2 norms for the gas velocity components, u_g and v_g, turbulent kinetic energy, k_g, and rate of turbulent kinetic energy dissipation, ϵ_g, were all less than 10^{-10}.

Simulations were conducted for three mesh levels [6, 12, 18] in the x-axial direction. Mesh levels were selected to ensure that the stream-ways velocity components in computational cells adjacent to the wall were located outside the buffer layer. Specifically, the first stream-ways velocity component should be located at least 30 *wall units* from the wall to be consistent with the $k-\epsilon$ model wall function implementation.

$$\frac{\Delta x}{2}\frac{v_* \rho_g}{\mu_g} > 30 \tag{3-14}$$

The MFIX results are shown in Figure 3-19 along with the direct numerical simulation (DNS) data of Lee and Moser [19] for $Re_\tau = 543$. The velocity profiles for the three mesh levels are shown on the left whereas the normalized velocity profiles with respect to wall units are shown on the right.

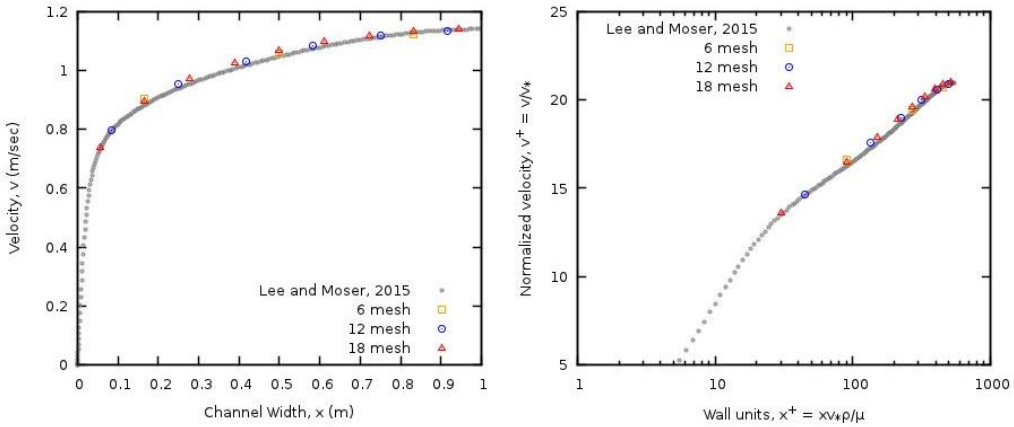

Figure 3-19: 2D, fully developed, turbulent channel flow with the DNS data of Lee and Moser [19]; (Left) Velocity profile; (Right) Non-dimensionalized channel width and velocity profile.

3.8 FLD08: Steady, 2D turbulent pipe flow

3.8.1 Description

This case uses turbulent flow in a pipe of length L and radius R to assess the single phase k-ϵ model in MFIX. A 2D axisymmetric domain is used to define the pipe geometry, and pressure boundaries are used to induce flow in the positive y-axial direction as shown in Figure 3-20. The results are compared with the experimental data of Zagarola and Smits [20].

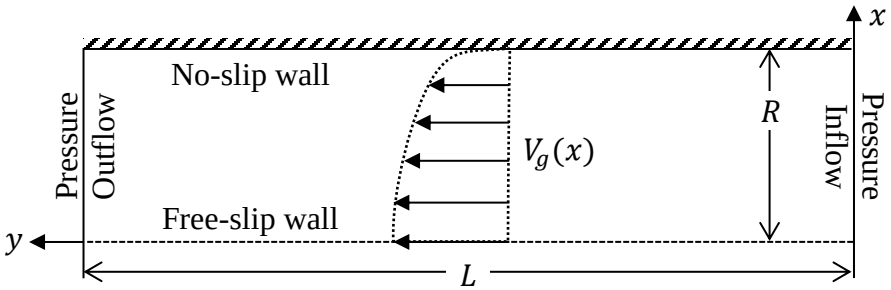

Figure 3-20: Turbulent flow in a pipe

3.8.2 Setup

Computational/Physical model

2D axisymmetric, unsteady, incompressible
Single phase (no solids)
No gravity
Thermal energy equation is not solved
Turbulent, standard k-ϵ model
Uniform mesh
Time step: 0.1 s
Discretization scheme: First-order upwind

Geometry		
Coordinate system	Cartesian	Grid partitions
Domain length, L (y)	8.00 (m)	100
Domain radius, R (x)	0.06468 (m)	16
Material		
Fluid density, ρ_g	1.1620 (kg·m^{-3})	
Fluid viscosity, μ_g	1.8487E-05 (Pa·s)	
Initial Conditions		
x-velocity, u_g	0.00 (m·s^{-1})	
y-velocity, v_g	5.00 (m·s^{-1})	
Turbulent kinetic energy, k_g	0.047 (m^2 s^{-2})	
Turbulence dissipation rate, ϵ_g	0.213 (m^2 s^{-3})	
Boundary Conditions		
West boundary	Free-slip wall	
East boundary	No-slip wall	
South wall, Pressure inflow	20.684 (Pa)	Specified pressure
Turbulent kinetic energy, k_g	0.047 (m^2 s^{-2})	
Turbulence dissipation rate, ϵ_g	0.213 (m^2 s^{-3})	
North wall, pressure outflow	0.00 (Pa)	

3.8.3 Results

Pressure drop in the y-axial direction, domain width, gas density and viscosity were chosen to reflect the conditions of Zagarola and Smits [20] for $Re = 41727$. A transient simulation was performed for better numerical stability. The solution was considered converged when the L_2 norms for the gas velocity components, u_g and v_g, turbulent kinetic energy, k_g, and rate of turbulent kinetic energy dissipation, ϵ_g, were all less than 10^{-10}.

The simulation was conducted with 16 cells in the x-axial direction. The mesh level ensures that the stream-ways velocity components in computational cells adjacent to the wall were located outside the buffer layer. Specifically, the first stream-ways velocity component was located at least 30 *wall units* from the wall to be consistent with the $k-\epsilon$ model wall function implementation.

$$\frac{\Delta x}{2}\frac{v_* \rho_g}{\mu_g} > 30 \tag{3-15}$$

Here, the friction velocity, v_*, is given by the Karman number, R^+ [20],

$$R^+ = \frac{D v_*}{\nu} \tag{3-16}$$

where D is pipe diameter, and ν is the kinematic viscosity.

The MFIX results are shown in Figure 3-21 along with the experimental data of Zagarola and Smits [20] for $Re = 41727$. The experimental dataset was accessed on November 10, 2016 from http://www.princeton.edu/~gasdyn/Superpipe_data/4.1727E+04.txt

The velocity profile is shown on the left, and the normalized velocity profile with respect to wall units is shown on the right. The velocity profile is given for two locations near the pipe exit, 7.2 m and 8.0 m respectively, with the maximum difference less than 10^{-2} m·sec^{-1}, indicating that the flow is fully developed. The largest discrepancy between the experimental measurements and the simulation results occurs at the centerline of the domain where the simulation under-predicts the observed velocity by 0.3 m·sec^{-1}.

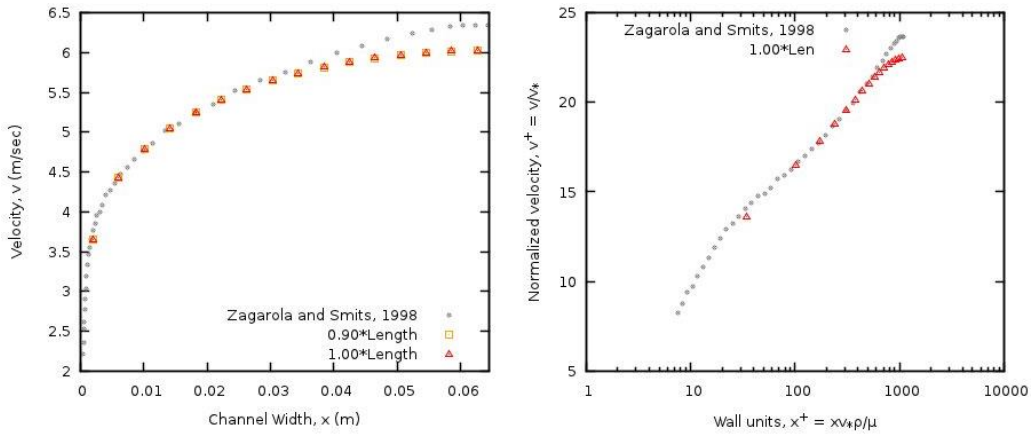

Figure 3-21: 2D, turbulent pipe flow with the experimental data of DNS data of Zagarola and Smits [20]; (Left) Velocity profiles; (Right) Nondimensionalized channel width and velocity profile.

Chapter 4: MFIX-DEM Code Verification Test Cases

The test cases presented in this chapter for the MFIX-DEM are summarized in Table 4-1. Test cases have been selected based the criteria for verification test selection outlined in Chapter 1. All cases are executed in serial mode unless explicitly noted.

Table 4-1: Summary of MFIX-DEM tests by feature

	Frequency†	Reference Dataset‡	Dimension	Coupled	Momentum	Thermal Energy	Particle Mass	Species Mass	Time-Stepping		Spring-Dashpot		Collisions		Friction		Distributed Memory	Shared Memory
									Euler	Adams-Bashforth	Linear	Hertzian	Particle-Particle	Particle-Wall	Particle-Particle	Particle-Wall		
DEM01	C	A	1D		✓				✓	✓	✓			✓				
DEM02	C	A	1D		✓					✓	✓			✓				
DEM03	C	A	1D		✓					✓	✓		✓	✓				
DEM04	C	A	1D		✓					✓	✓			✓				
DEM05	C	P	2D							✓	✓	✓	✓	✓				
DEM06	C	A	1D	✓														

† C-Incorporated into the continuous integration server; M-Monthly; Q-Quarterly; X-Manual; D-Disabled

‡ A-Analytical solution; P-Published benchmark data; R-Regression data from previous code versions

4.1 DEM01: Freely-falling particle

This case serves to verify the MFIX-DEM linear spring-dashpot collision model as well as the accuracy of the time-stepping methods. This case is based on the work of Chen et al. [21] and the MFIX-DEM case was originally reported in [22].

4.1.1 Description

A smooth (frictionless), spherical particle falls freely under gravity from an initial height, h_0, and bounces upon collision with a fixed wall. The translating motion of the particle is described in three stages, as depicted in Figure 4-1: free fall, contact and rebound. An analytic expression for particle motion during each stage is obtained.

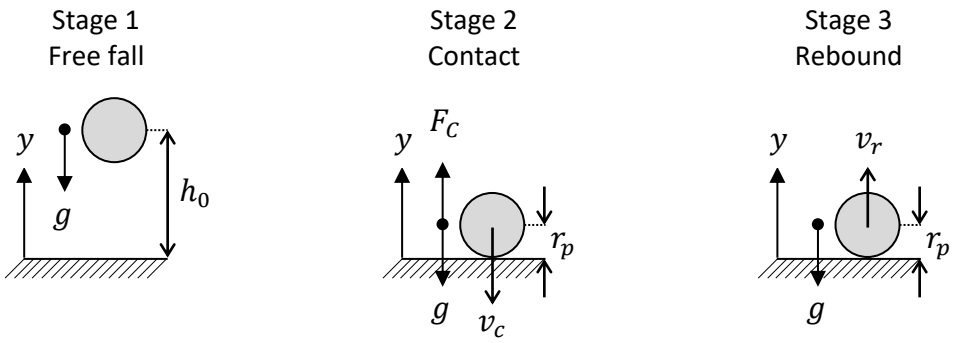

Figure 4-1: A particle with radius r_p falling onto a fixed wall from an initial height of h_0 where g is the gravitational force, F_C is repulsive particle-wall collision force, v_c is the pre-collision particle velocity, and v_r is the post-collision particle velocity.

Stage 1: Free fall

A force balance on the particle provides an expression for particle motion during free fall,

$$\frac{d^2y}{dt^2} = -g; \quad y(0) = h_0; \; \frac{dy}{dt}(0) = 0 \tag{4-1}$$

where y is the center position of the particle with respect to the wall and g is the acceleration due to gravity. The particle is initially at rest with a center distance of h_0 above the wall. The instantaneous velocity, v, and particle center position are given by

$$v(t) = -gt \tag{4-2}$$

$$y(t) = h_0 - \frac{1}{2}gt^2 \tag{4-3}$$

Stage 2: Contact

The free fall stage ends and the contact stage begins when the particle center position is equal to the particle radius. The particle-wall collision is treated using the linear spring-dashpot model such that the force balance on the particle during contact gives

$$\frac{d^2y}{dt^2} + 2\beta\omega_o\frac{dy}{dt} + \omega_o^2 y = \omega_o^2 r_p - g; \quad y(0) = r_p; \; \frac{dy}{dt}(0) = -\sqrt{2g\left(h_0 - r_p\right)} \tag{4-4}$$

where $\beta = \eta_n/\left(2\sqrt{k_n m_p}\right)$ and $\omega_o = \sqrt{k_n/m_p}$. Here, k_n and η_n are the normal spring coefficient and damping coefficients for the particle-wall collision, and m_p is the particle mass. The initial particle velocity is obtained from combining (4-2) and (4-3) when the particle center position is equal to its radius. The instantaneous velocity and particle center position during contact for an underdamped system, $\beta < 1$, are given by

$$v(t) = \left[-\sqrt{2g\left(h_0 - r_p\right)}\cos\left(\sqrt{1-\beta^2}\omega_o t\right) + \frac{\beta\omega_o\sqrt{2g\left(h_0 - r_p\right)} - g}{\omega_o\sqrt{1-\beta^2}}\sin\left(\sqrt{1-\beta^2}\omega_o t\right)\right]\exp(-\beta\omega_o t) \tag{4-5}$$

$$y(t) = \left[\frac{g}{\omega_o^2}\cos\left(\sqrt{1-\beta^2}\omega_o t\right) + \frac{-\sqrt{2g\left(h_0 - r_p\right)} - \frac{\beta g}{\omega_o}}{\omega_o\sqrt{1-\beta^2}}\sin\left(\sqrt{1-\beta^2}\omega_o t\right)\right]\exp(-\beta\omega_o t) + \left(r_p - \frac{g}{\omega_o^2}\right) \tag{4-6}$$

Stage 3: Rebound

The contact stage ends and the rebound stage begins when the particle center position is again equal to the particle radius. A force balance on the particle leads to an expression for the particle motion,

$$\frac{d^2y}{dt^2} = -g; \quad y(0) = r_p; \; \frac{dy}{dt}(0) = v_c. \tag{4-7}$$

The velocity at the start of the rebound stage is equal to the velocity at the end of the contact stage, v_c. It is obtained by solving equation (4-6) for time when the particle center position is equal to the particle radius, then substituting the result into equation (4-5). The instantaneous velocity, v, and particle center position, y, are given by

$$v(t) = v_c - gt \tag{4-8}$$

$$y(t) = r_p + v_c t - \frac{1}{2}gt^2. \tag{4-9}$$

4.1.2 Setup

Computational/Physical model

1D, Transient
Granular Flow (no gas)
Gravity
Thermal energy equation is not solved

Geometry	
Coordinate system	Cartesian
x-length	1.0 (m)
z-length	1.0 (m)
y-length	1.0 (m)
Solids Properties	
Normal spring coefficient, k_n	*varied* (N·m^{-1})
Restitution coefficient, e_n	*varied* (-)
Friction coefficient, μ	0.0 (-)
Solids 1 Type	DEM
Diameter, d_p	0.2 (m)
Density, ρ_s	2,600 (kg·m^{-3})
Boundary Conditions	
All boundaries	Solid Walls

4.1.3 Results

Simulations of a freely-falling particle dropped from an initial height of 0.5m were conducted for four particle-wall normal spring coefficients, $[1.0, 2.5, 5.0, 10.0] \times 10^4$ N·m^{-1}, and five restitution coefficients, [0.6, 0.7, 0.8, 0.9, 1.0]. The test using a normal spring coefficient of 10^4 N·m^{-1} and restitution coefficient 0.6 were unsuccessful because this combination leads to the particle center crossing the fixed boundary indicating that the particle is located outside of the domain. The following results were obtained using the Euler time stepping method.

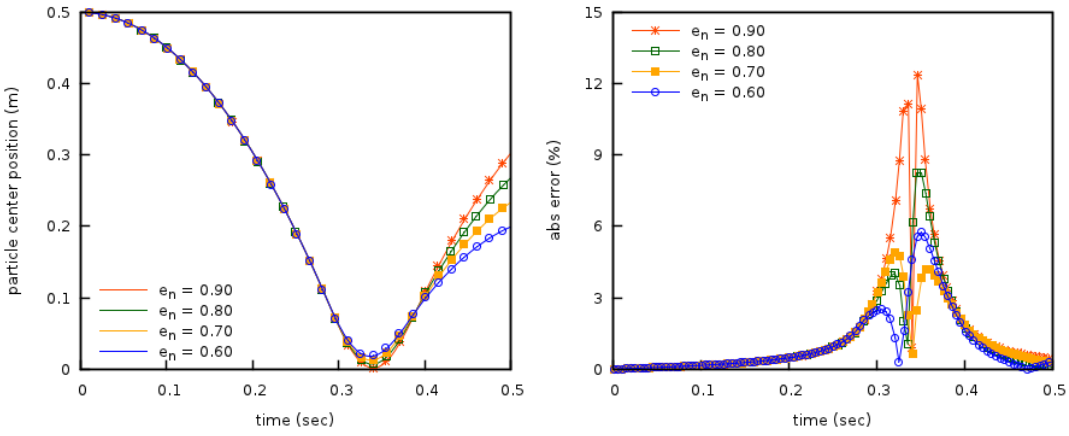

Figure 4-2: Comparison of analytical solution and DEM results for a freely-falling particle using the Euler time-stepping method for varying restitution coefficient, normal spring coefficient, $k_n = 10^4$ N•m^{-1}. (Left) Particle center position; analytical solutions shown as continuous lines, MFIX-DEM results as points. (Right) Percent absolute relative error between the analytical and MFIX-DEM particle center positions.

The particle center position for cases using a normal spring coefficient of 10^4 N·m^{-1} are shown in Figure 4-2. These cases demonstrate the largest errors in particle center position during the

contact stage. The large error is attributed to the particle center position approaching the fixed boundary, $y \rightarrow 0$, during the contact stage. This leads to near-zero values used in the absolute value of the relative error calculations. In all other cases, the absolute percent relative error remains below 3% with errors decreasing with increasing normal spring coefficient.

The particle velocity for cases using a slightly stiffer normal spring coefficient of 10^5 N·m^{-1} are shown in Figure 4-3. Again, the large errors are primarily attributed to near-zero values used in the relative error calculations. The initial spike in error arises at the peak of the contact stage when the particle trajectory reverses, passing through zero. Similarly, large relative errors occur at the peak of the rebound stage when the particle trajectory again reverses direction.

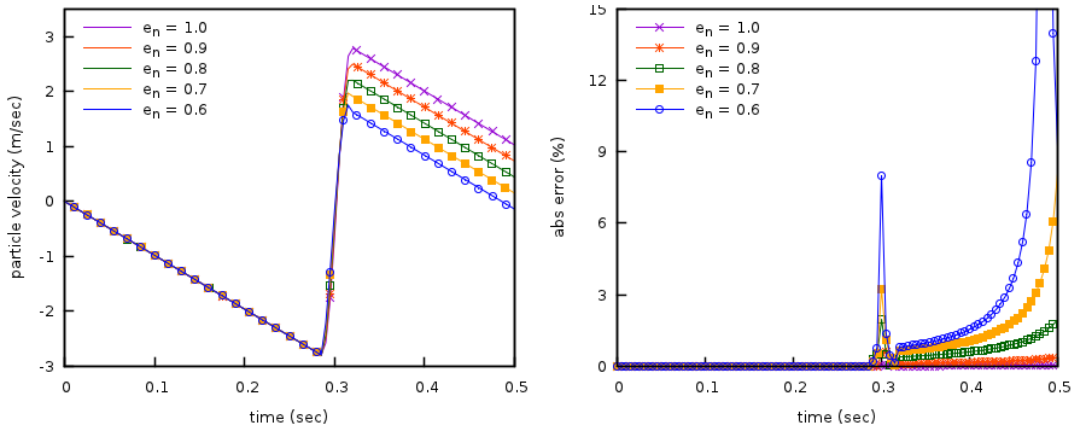

Figure 4-3: Comparison of analytical solution and DEM results for a freely-falling particle using the Euler time-stepping method for varying restitution coefficients, and normal spring coefficient, $k_n = 10^5$ N•m^{-1}. (Left) Particle velocities; analytical solutions shown as continuous lines, MFIX-DEM results as points. (Right) Percent absolute relative error between the analytical and MFIX-DEM particle velocities.

Analysis of the time-stepping methods is limited to the free-fall stage and excludes error arising from the collision model. Pre- and post-collision results using the Euler and Adams-Bashforth methods with a normal spring coefficient of 10^5 N·m^{-1} are shown in Figure 4-3. During the free fall stage (pre-collision), the Euler method shows a linear accumulation of error in particle position whereas the error in particle velocity is zero. The Adams-Bashforth method shows no (zero) error for both particle position and velocity. These results are consistent across all cases.

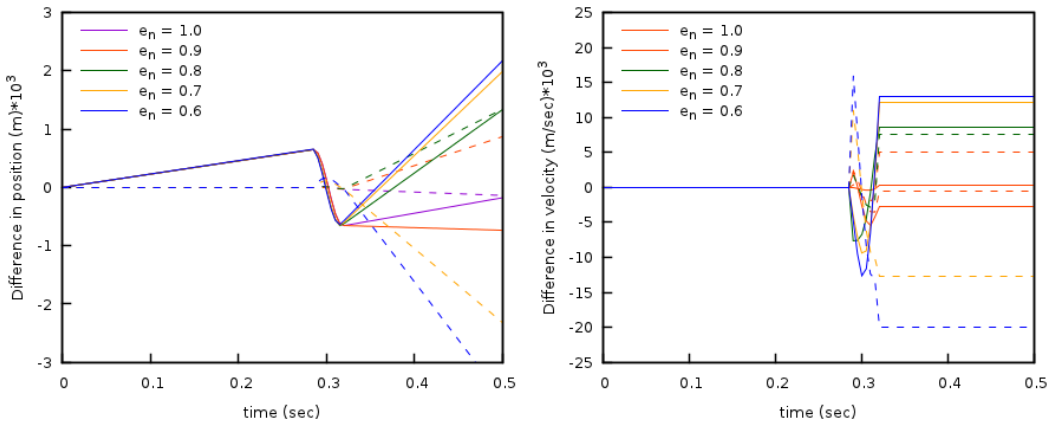

Figure 4-4: Difference between analytical solution and MFIX-DEM results for a freely-falling particle with varying restitution coefficient and normal spring coefficient, $k_n = 10^5$ N•m^{-1}. Euler method shown as solid line. Adams-Bashforth method shown as dashed lines. (Left) Difference in particle position. (Right) Difference in particle velocity.

4.2 DEM02: Bouncing particle

This case provides a comparison between the MFIX-DEM linear spring-dashpot collision model and the *hard sphere* model where collisions are instantaneous. The hard sphere model can be seen as the limiting case where the normal spring coefficient is large, $k_n \to \infty$. This case was originally reported in [22].

4.2.1 Description

A smooth (frictionless), spherical particle falls freely under gravity from an initial height, h_0, and bounces upon collision with a fixed wall (see Figure 4-1). Assuming that the collision is instantaneous, the maximum height the particle reaches after the first collision (bounce), $h_1^{\max}$, is given by

$$h_1^{\max} = (h_0 - r_p)e_n^2 \tag{4-10}$$

where r_p is the particle radius, and e_n is the restitution coefficient. A general expression for the maximum height following the k^{th} bounce is

$$h_k^{\max} = (h_0 - r_p)e_n^{2k} + r_p. \tag{4-11}$$

4.2.2 Setup

Computational/Physical model

1D, Transient
Granular Flow (no gas)
Gravity
Thermal energy equation is not solved

Geometry

Coordinate system	Cartesian
x-length	1.0 (m)
z-length	1.0 (m)
y-length	1.0 (m)

Solids Properties

Normal spring coefficient, k_n	*varied* ($N \cdot m^{-1}$)
Restitution coefficient, e_n	*varied* (-)
Friction coefficient, μ	0.0 (-)

Solids Type DEM

Diameter, d_p	0.2 (m)
Density, ρ_s	2,600 ($kg \cdot m^{-3}$)

Boundary Conditions

All boundaries	Solid Walls

4.2.3 Results

Simulations of a freely-falling particle dropped from an initial height of 0.5m were conducted for three normal spring coefficients, $[0.5, 5.0, 50.0] \times 10^5$ $N \cdot m^{-1}$, and six restitution coefficients, [0.5, 0.6, 0.7, 0.8, 0.9, 1.0]. All simulations employed the Adams-Bashforth time-stepping method. The maximum height attained after the k^{th} collision for all cases is shown in Figure 4-5.

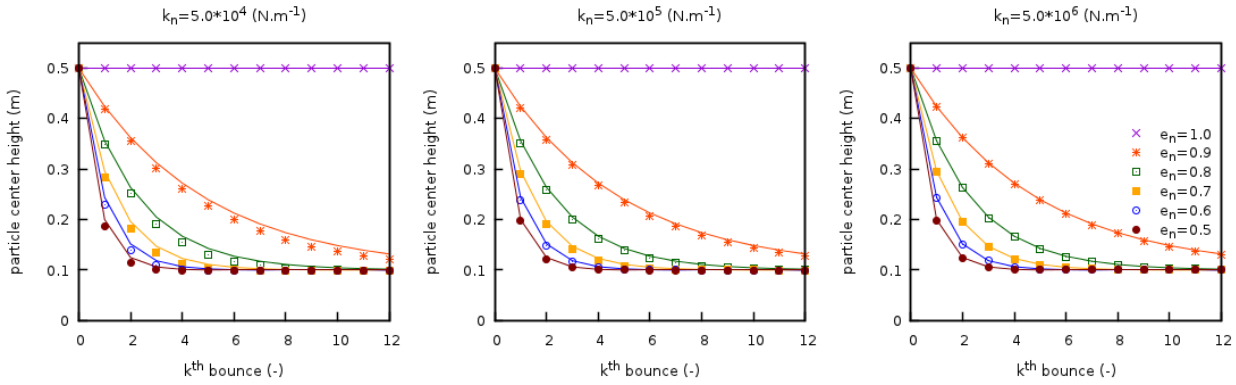

Figure 4-5: Comparison between the analytic solution from a hard-sphere model (solid lines) and MFIX-DEM (symbols) of the maximum height reached after the k^{th} wall collision for a freely falling particle. Three values for the normal spring coefficient are used (left to right) with six restitution coefficients.

Figure 4-6 illustrates the percent relative difference between the analytical solution for a hard-sphere model and the MFIX-DEM simulation. In the limit of the hard-sphere model (shown left to right by an increasing spring coefficient), the difference between the two collision models decreases.

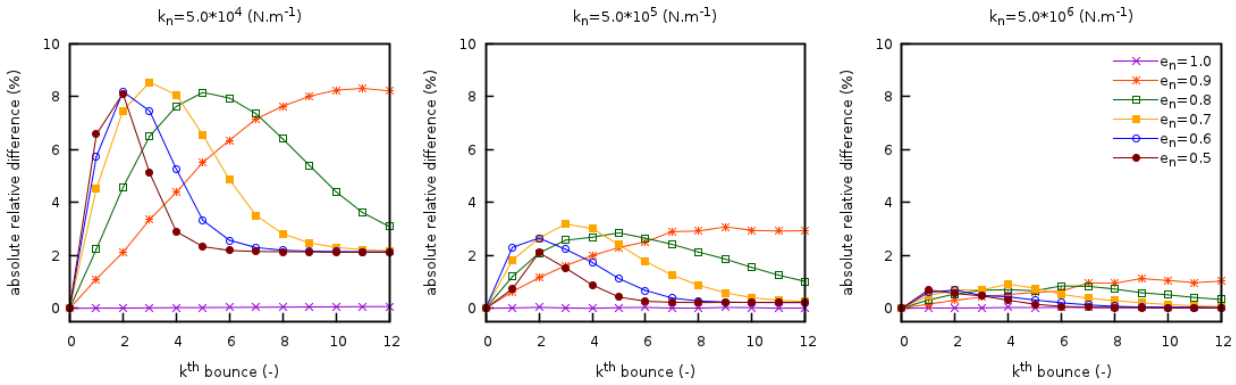

Figure 4-6: Percent relative difference between the analytic solution for a hard-sphere model and MFIX-DEM of the maximum height reached after the k^{th} wall collision for a freely falling particle. Three values for the normal spring coefficient are used (left to right) with six restitution coefficients.

4.3 DEM03: Two stacked, compressed particles

This case serves to verify the MFIX-DEM linear spring-dashpot collision model through analysis of a multi-particle, enduring collision. This test case is based on the work of Chen et al. [21] and the MFIX-DEM test case was originally reported in [22].

4.3.1 Description

Two particles of equal radius, r_p, are stacked between two fixed walls such that the particles are compressed. The lower and upper walls are located at $y_l = 0.0$ and $y_w = 3.6r_p$ and the particle centers are initially located at $y_{10} = 0.25y_w$ and $y_{20} = 0.75y_w$. This configuration, illustrated in Figure 4-7, ensures that the particles remain in contact and compressed.

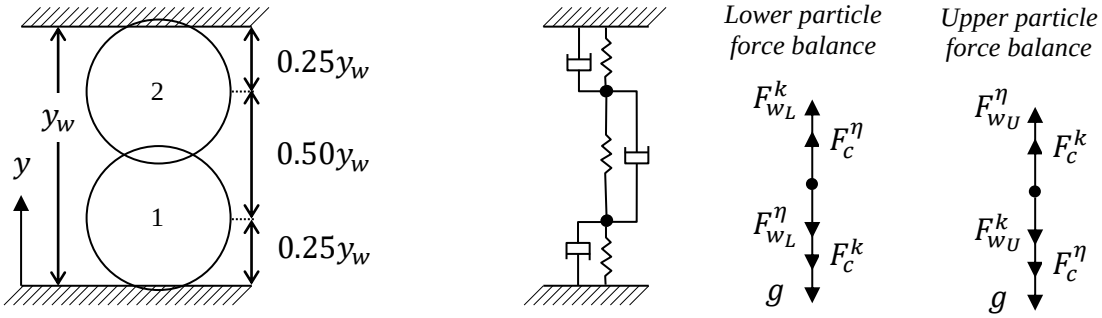

Figure 4-7: Two smooth spherical particles stacked between two fixed walls so that the system is always under compression. A sketch of the problem mechanics is provided along with force balances for the lower and upper particles.

An expression for the acceleration of the lower particle (*particle 1*) is

$$\frac{d^2y_1}{dt^2} = -g - \frac{k_{nw}}{m_1}\left(y_1 - r_p\right) - \frac{\eta_{n1w}}{m_1}\frac{dy_1}{dt} - \frac{k_{n12}}{m_1}\left(2r_p - (y_2 - y_1)\right) - \frac{\eta_{n12}}{m_1}\left(\frac{dy_1}{dt} - \frac{dy_2}{dt}\right) \tag{4-12}$$

where y_1 and y_2 are the particle center positions measured from the lower wall, g is the acceleration due to gravity, k_{nw} and k_{n12} are the particle-wall and particle-particle spring coefficients, η_{n1w} and η_{n12} are the particle-wall and particle-particle damping coefficients, and m_1 is the mass of particle 1. Similarly, acceleration of the upper particle (*particle 2*) is given by

$$\frac{d^2y_2}{dt^2} = -g - \frac{k_{nw}}{m_2}\left(r_p - (y_w - y_2)\right) - \frac{\eta_{n2w}}{m_2}\frac{dy_2}{dt} + \frac{k_{n12}}{m_2}\left(2r_p - (y_2 - y_1)\right) + \frac{\eta_{n12}}{m_2}\left(\frac{dy_1}{dt} - \frac{dy_2}{dt}\right) \tag{4-13}$$

where η_{n2w} is the particle-wall damping coefficient for the upper particle, and m_2 is the mass of the upper particle.

4.3.2 Setup

Computational/Physical model

1D, Transient
Granular Flow (no gas)
Gravity
Thermal energy equation is not solved

Geometry

Coordinate system	Cartesian
x-length	1.0 (m)
z-length	0.0010 (m)
y-length	0.0018 (m)

Solids Properties

Normal spring coefficient, k_n	10^3 (N·m^{-1})
Restitution coefficient, e_n	*varied* (-)
Friction coefficient, μ	0.0 (-)

Solids 1 Type	DEM
Diameter, d_{p1}	0.001 (m)
Density, ρ_{s1}	20,000 (kg·m^{-3})

Solids 2 Type	DEM
Diameter, d_{p2}	0.001 (m)

Density, ρ_{s2}	10,000 ($kg \cdot m^{-3}$)

Boundary Conditions

All boundaries	Solid Walls

4.3.3 Results

Analytical solutions to equations (4-12) and (4-13) describing the motion of the particles are readily obtainable for perfectly elastic ($\eta_{n12} = \eta_{n1w} = \eta_{n2w} = 1.0$) particles of equal mass ($m_1 = m_2$). This is not the case for inelastic particles of different mass, therefore a fourth-order Runge-Kutta method is used to calculate a secondary numerical solution which is considered to be the analytical solution during the analysis.

Simulations were conducted for six friction coefficients, [0.5, 0.6, 0.7, 0.8, 0.9, 1.0], using the Adams-Bashforth time-stepping method. Figure 4-8 shows the motion of the lower (left) and upper (right) particles as well as the absolute value of the relative error for a restitution coefficient of 1. The percent relative difference in results remains below 0.1% for this case. This is the largest observed difference across all cases with the difference in relative error decreasing with decreasing restitution coefficient.

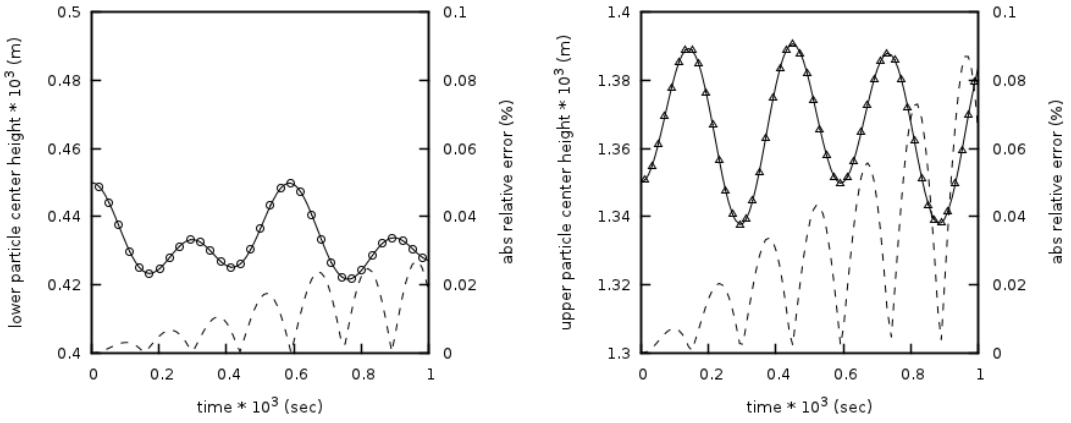

Figure 4-8: Comparison between the fourth-order Runge-Kutta solution (solid line) and MFIX-DEM simulation (open symbols) for the center position of two stacked particles compressed between fixed walls for a restitution coefficient of 1. The absolute percent relative errors are shown as dashed lines.

4.4 DEM04: Slipping on a rough surface

This case serves to verify the MFIX-DEM soft-spring collision model through the analysis of the rolling friction model. This test case was originally reported in [22].

4.4.1 Description

A spherical particle of radius, r_p, finite translation velocity, u_0, and zero angular velocity, ω_0, is placed on a rough surface as illustrated in Figure 4-9. The particle begins to roll while the translational velocity decreases because of rolling friction attributed to slip between the particle and the rough surface at the point of contact ($u \neq \omega r_p$). The rolling friction converts translation velocity to angular velocity until there is no slip at the contact point ($u = \omega r_p$). After the no-slip condition is reached, rolling friction ceases and the particle continues to move with constant translational and rotational velocities.

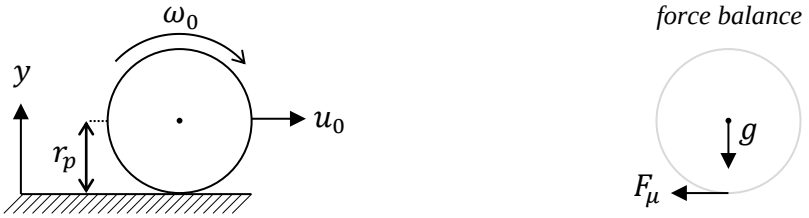

Figure 4-9: A spherical particle with finite translational velocity and zero angular velocity is placed on a rough surface. Forces acting on the particle are indicated.

Kinetic friction is the only translational force acting on the particle and is given by

$$\frac{du}{dt} = \frac{d^2x}{dt^2} = -\mu g. \tag{4-14}$$

where g is the acceleration due to gravity, and μ is the coefficient of friction. Similarly, the angular velocity is given by

$$\frac{d\omega}{dt} = \frac{\mu g m r_p}{I} \tag{4-15}$$

where $I = 2mr_p^2/5$ and m are the particle moment of inertia and mass, respectively. Integrating equations (4-14) and (4-15) with initial conditions u_0 and ω_0, an expression for the time when rolling friction ceases ($u = \omega r_p$) is obtained,

$$t_s = \frac{2u_0}{7\mu g} \tag{4-16}$$

4.4.2 Setup

Computational/Physical model

1D, Transient
Granular Flow (no gas)
Gravity
Thermal energy equation is not solved

Geometry

Coordinate system	Cartesian
x-length	1.0 (m)
z-length	1.0 (m)
y-length	1.0 (m)
Solids Properties	
Normal spring coefficient, k_n	10^4 (N·m^{-1})
Restitution coefficient, e_n	1.0 (-)
Friction coefficient, μ	*varied* (-)
Solids 1 Type	DEM
Diameter, d_p	0.001 (m)
Density, ρ_s	10,000 (kg·m^{-3})
Boundary Conditions	
All boundaries	Solid Walls

4.4.3 Results

Simulations were conducted for nine restitution coefficients, [0.2, 0.3, 0.4, 0.4, 0.6, 0.7, 0.8, 0.9 1.0], using the Adams-Bashforth time-stepping method with the results shown in Figure 4-10. The absolute relative percent error between the MFIX-DEM and analytical value for the non-dimensionalized time when rolling friction ceases, $t_s/(\mu g/u_0)$, is less than 1% for all reported conditions. Similarly, the absolute relative percent error between the MFIX-DEM and analytical value for the non-dimensionalized tangential and angular velocities is less than 0.1% for all reported conditions. Error between the MFIX-DEM and analytical values can be further reduced (not shown) by increasing the normal spring coefficient, k_n, which decreases the DEM solids time-step size.

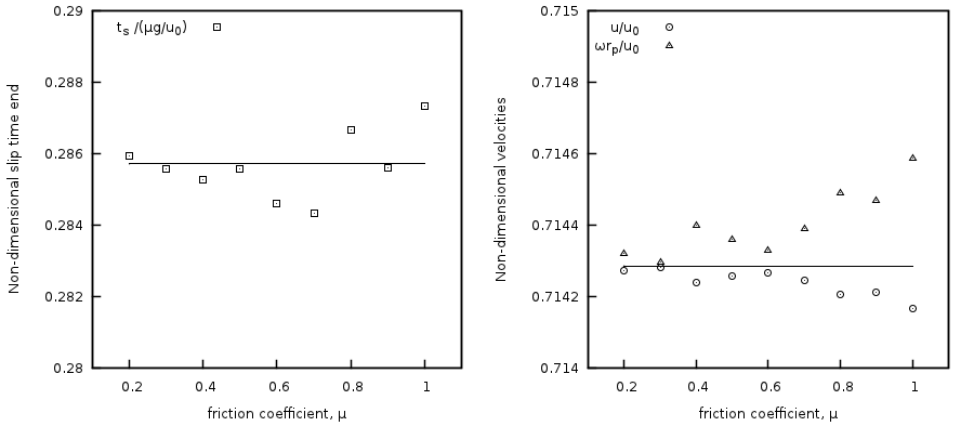

Figure 4-10: Comparison between the analytical solution (solid line) and MFIX-DEM simulation (open symbols) of a particle with radius r_p slipping on a rough surface for various friction coefficients. (left) Dimensionless slip time end and (right) dimensionless equilibrium tangential, u, and angular, ω, velocities.

4.5 DEM05: Oblique particle collision

This case serves to verify the normal and tangential components of both the linear spring-dashpot and Hertzian collision models in MFIX DEM. This case is based on the modeling work of Di Renzo and Di Maio [23] and utilizes the experimental data of Kharaz, Gorham, and Salman [24].

4.5.1 Description

In the experiments of Kharaz, Gorham, and Salman [24], a spherical particle is dropped from a fixed height such that it collides with a rigid surface at a known velocity. The angle of the ridged surface is varied to test impact angles ranging from normal to glancing. The rebound angle, post-collision angular velocity, and observed tangential restitution coefficient were reported.

In the experiment, the particle strikes an angled anvil as illustrated in Figure 4-11(a). Rather than modeling an angled surface, the wall is kept level (flat) and the particle is given an initial trajectory corresponding to the angle found in the experiment as shown in Figure 4-11(b). The particle is initially positioned close to the wall and gravity is suppressed in the simulations to eliminate the effects of the rotated geometry with respect to the experimental apparatus.

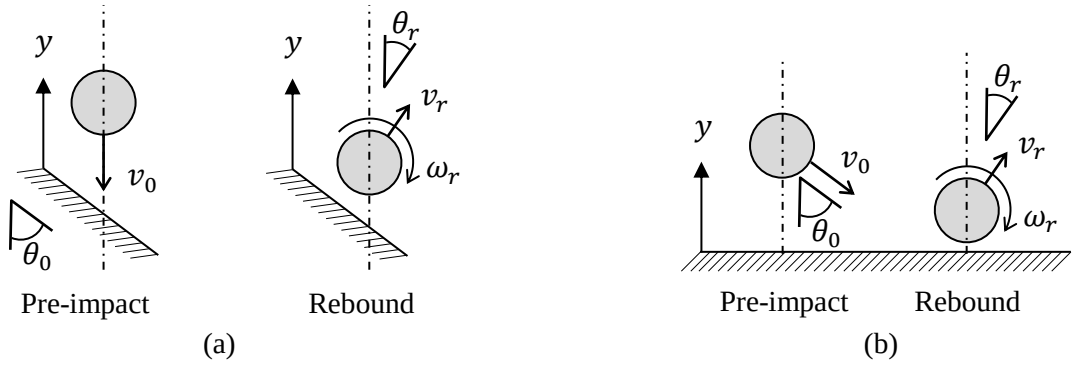

Figure 4-11: (a) Experimental setup of Kharaz, Gorham, and Salman [24] of a particle striking a fixed, angled anvil. (b) Simulation setup whereby the particle is given an initial velocity to replicate the particle striking an angled surface.

4.5.2 Setup

Computational/Physical model

3D, Transient
Granular Flow (no gas)
No gravity
Thermal energy equation is not solved

Geometry

Coordinate system	Cartesian
x-length	0.5 (m)
z-length	0.5 (m)
y-length	0.1 (m)

Solids Phase 1	DEM
Diameter, d_p	0.005 (m)
Density, ρ_s	5,000 (kg·m^{-3})
Solids Phase 2	DEM
Diameter, d_p	0.005 (m)
Density, ρ_s	5,000 (kg·m^{-3})
Boundary Conditions	
All boundaries	No Slip Walls

The mechanical properties for the particle (solids phase 1) and the anvil (solids phase 2 and wall) are provided for both the linear spring-dashpot and Hertzian collision models. The second solids phase is given the same properties as the anvil for verification of both the particle-particle and particle-wall collision model implementations.

Solids Phase 1	**Linear**	**Hertzian**
Normal spring coefficient, (N·m^{-1})	1.72×10^{7}	—
Restitution coefficient, (N·m^{-1})	1.48×10^{7}	—
Young's modulus, (Pa)	—	380×10^{9}
Poisson ratio	—	0.23
Friction coefficient	0.092	0.092
Solids Phase 2 & Wall		
Normal spring coefficient, (N·m^{-1})	1.72×10^{7}	—
Restitution coefficient, (N·m^{-1})	1.48×10^{7}	—
Young's modulus, (Pa)	—	70×10^{9}
Poisson ratio	—	0.25
Friction coefficient	0.092	0.092

4.5.3 Results

Simulations were conducted using the linear spring-dashpot and Hertzian collision models. Each simulation contained a total of 93 particles. The particle-particle and particle-wall collision models were tested by varying the initial collision angles between 0 (normal) and 65 degrees (glancing). Gravity was suppressed in the simulations to eliminate the effects of the rotated geometry with respect to the experimental apparatus.

The rebound angle, observed tangential restitution coefficient, and post-collision angular velocity for particle-wall collisions are given in Figure 4-12 with particle-particle collision results shown in Figure 4-13. There is good agreement between the simulation results and experimental data for the rebound angle and post-collision angular velocity. Although both models over predict the

observed tangential coefficient for steep (near-normal) collision angles, better agreement is observed with the linear spring-dashpot model for the parameters used.

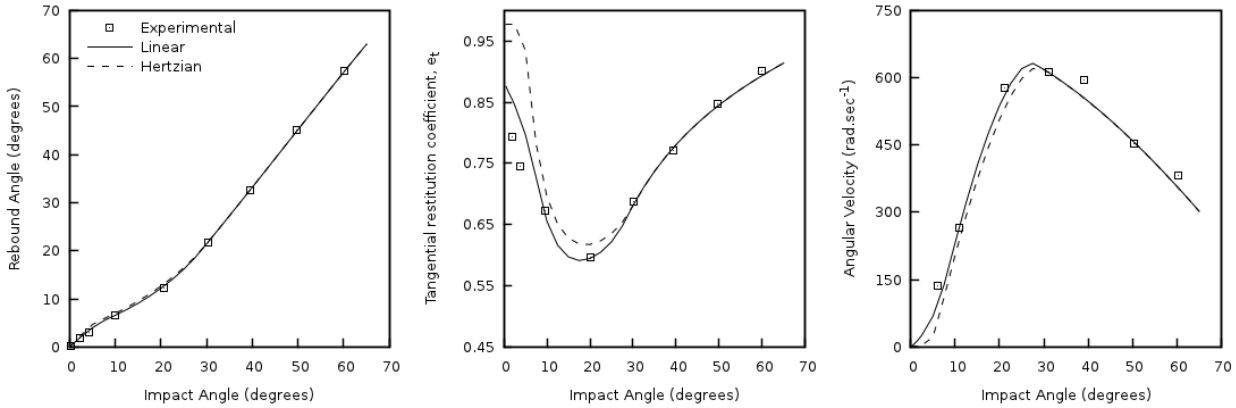

Figure 4-12: Particle-wall oblique collision results for the linear spring-dashpot model (solid line), Hertzian model (dashed line), and experimental data (symbols) of Kharaz, Gorham, and Salman [24].

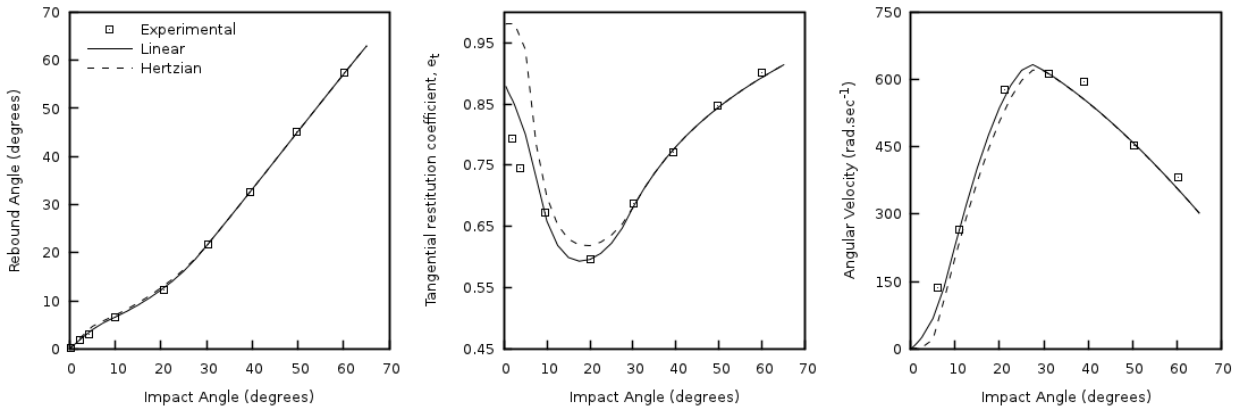

Figure 4-13: Particle-particle oblique collision results for the linear spring-dashpot model (solid line), Hertzian model (dashed line), and experimental data (symbols) of Kharaz, Gorham, and Salman [24].

4.6 DEM06: Single particle, terminal velocity

This case investigates the interphase coupling of momentum equations though the gas-solids drag force. The original case was reported in [22] and has been expanded to test additional coupling schemes.

4.6.1 Description

A single particle initially at rest is released in a uniform gas stream as illustrated in Figure 4-14 where the gravitational and gas-solids drag forces are the dominant forces acting on the particle. The velocity of the particle increases until it reaches its *terminal velocity* where the gravitational force is equal to the gas-solids drag force.

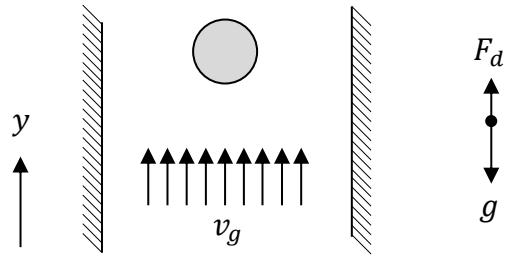

Figure 4-14: A single spherical particle initially at rest is released in a uniform, vertical air flow. The dominant forces acting on the particle are the gas-solids drag force, F_d, and the gravitational force, g.

For a sufficiently small particle, the evolution of the particle velocity is given by

$$\frac{d^2y}{dt^2} = \frac{dv_p}{dt} = \frac{g(\rho_p - \rho_g)}{\rho_p} - \frac{3}{4}\frac{\rho_g \|v_p - v_g\|_2}{d_p \rho_p} C_d; \quad y(0) = h_0; \quad \frac{dy}{dt}(0) = 0 \tag{4-17}$$

where y is the particle center position measured from the bottom wall, v_p and v_g are the particle and gas velocities, ρ_p and ρ_g are the particle and gas densities, d_p is the particle diameter, h_0 is the initial height of the particle, g is the acceleration due to gravity, and C_d is the drag coefficient. The drag coefficient is estimated here using the Schiller and Naumann [25] correlation for a single particle in an unbounded medium,

$$C_d = \frac{24}{\mathrm{N_{Re}}}(1 + 0.15 N_{\mathrm{Re}}^{0.687}) \tag{4-18}$$

where N_{Re} is the Reynolds number based on the slip velocity between the particle and gas defined as

$$N_{\mathrm{Re}} = \frac{\rho_g \|v_p - v_g\|_2 d_p}{\mu_g}. \tag{4-19}$$

4.6.2 Setup

Computational/Physical model

1D, Transient, incompressible
Multiphase flow (gas-solids)
Gravity
Thermal energy equation is not solved

Geometry

Coordinate system	Cartesian
x-length	0.01 (m)
z-length	0.10 (m)
y-length	0.01 (m)

Solids Properties

Normal spring coefficient, k_n	10^{-1} (N·m^{-1})

Restitution coefficient, e_n	1.0 (-)
Friction coefficient, μ	0.0 (-)
Solids 1 Type	DEM
Diameter, d_p	10^{-4} (m)
Density, ρ_s	2,000 (kg·m^{-3})
Boundary Conditions	
South face (XZ-plane; y=0.00m)	Gas Mass Inflow
Pressure (gauge)	0.00 (Pa)
Gas velocity, v_g	0.40 (m·s^{-1})
North face (XZ-plane; y=0.10m)	Pressure Outflow
Pressure (gauge)	0.00 (Pa)
Top, Bottom, East, West faces	Free Slip Walls

4.6.3 Results

A fourth-order Runge-Kutta method was used to calculate the solution to (4-17) which was subsequently compared with the solutions of the seven MFIX-DEM simulations outlined below. The first set of simulations were one-way coupled such that only the gas phase volume fraction was affected by the presence of the particle. Specifically, gas-solids drag force was omitted from the gas phase momentum equations. This case best captured the above problem description where a single particle is freely falling through a uniform gas field. In the second group of tests the gas and solids were fully coupled. Three interpolation methods were used with both the one-way and fully coupled tests.

Interpolation Scheme	Coupling	Filter Size
Centroid	one-way	—
Garg_2012	one-way	—
DPVM_Square	one-way	2.0×10^{-3}
Centroid	full	—
Garg_2012	full	—
DPVM_Square	full	3.0×10^{-3}
DPVM_Square	full	4.0×10^{-3}

Figure 4-15 illustrates a typical comparison of analytical particle velocity evolution over time obtained by Equation (4-17) and the numerical solution. A comparison of the absolute percent relative difference between the solutions is shown in Figure 4-16. The numerical solution from simulations employing one-way coupling (left) compare well with the analytical solution of Equation (4-17) with the maximum absolute relative difference bounded above by 5×10^{-3} percent for the three cases. Additionally, the maximum absolute relative difference for cases with full coupling is bounded from above by 5 percent.

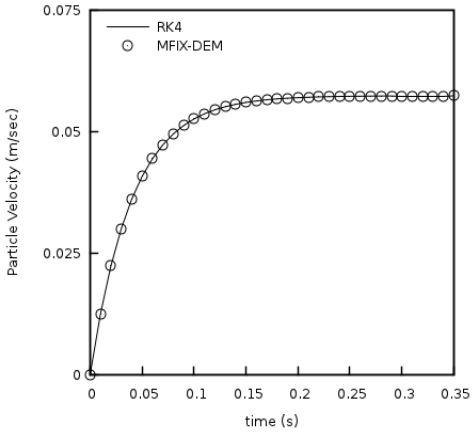

Figure 4-15: Comparison of the particle velocity evolution obtained by equation (4-17) and MFIX-DEM.

The large difference in results for the fully coupled cases should not be interpreted as error because the assumption of a uniform gas velocity used to establish Equation (4-17) is no longer valid when the gas-solids drag is allowed to affect the gas velocity as is the case in the fully coupled simulations. The suitability of this assumption, or lack thereof, is apparent from inspecting the results from different coupling schemes. The centroid method concentrates the gas-solids drag force in the fluid cell containing the particle center. As a result, gas velocity is impacted the most when compared to the other methods available. The divided particle volume method (DVPM) diffuses the gas-solids drag force over an area based on the filter width providing better agreement. Finally, the GARG_2012 scheme shows the best agreement as it diffuses the gas-solids drag force over the greatest area thereby providing greater consistency with the uniform flow field assumption.

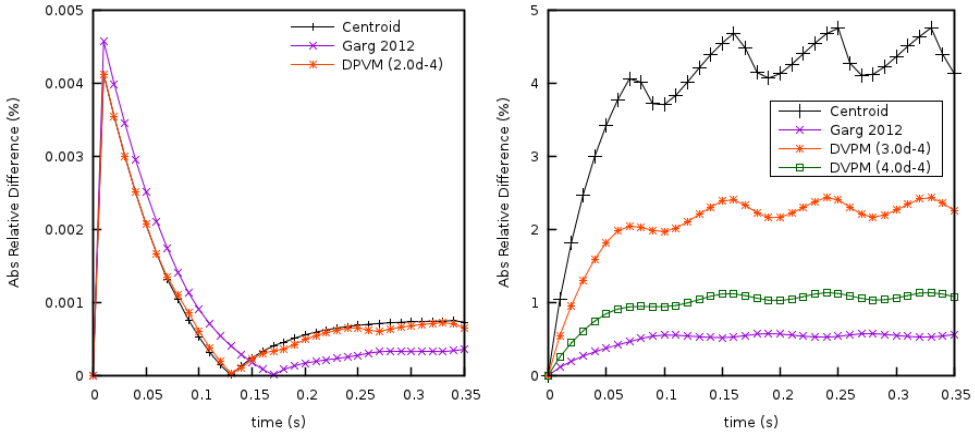

Figure 4-16: Absolute percent relative difference between particle velocity evolution obtained by equation (4-17) and MFIX-DEM. (left) Simulations with one-way gas-solids coupling. (right) Fully coupled simulations.

References

[1] AIAA, "Guide for the Verification and Validation of Computational Fluid Dynamics Simulations (AIAA G-077-1998(2002))," American Institute of Aeronautics and Astronautics (AIAA), 1998.

[2] P. J. Roache, "Quantification of uncertainty in computational fluid dynamics," *Annual Review of Fluid Mechanics,* vol. 29, pp. 123-160, 1997.

[3] S. Schlesinger, "Terminology for model credibility," *SIMULATION,* vol. 32, no. 3, pp. 103-104, 1979.

[4] W. Oberkampf and T. Trucano, "Verification and Validation in Computational Fluid Dynamics," Sandia National Laboratories, 2002.

[5] P. J. Roache, Fundamentals of Verification and Validation, Socorro, NM: Hermosa Publishers, 2009.

[6] M. Syamlal, T. O'Brien, S. Benyahia, A. Gel and S. Pannala, "Open-Source Software in Computational Research: A Case Study," *Modelling and Simulation in Engineering,* vol. 937542, 2008.

[7] P. J. Roache and S. Steinberg, "Symbolic manipulation and computational fluid dynamics," *AIAA Journal,* vol. 22, no. 10, pp. 1390-1394, October 1984.

[8] C. J. Roy, "Review of code and solution verification procedures for computational simulation," *Journal of Computational Physics,* vol. 205, no. 1, pp. 131-156, 2005.

[9] W. L. Oberkampf and C. J. Roy, Verification and validation in scientific computing, Cambridge: Cambridge University Press, 2010.

[10] W. L. Oberkampf and C. J. Roy, Verification and Validation in Scientific Computing, New York: Cambridge University Press, 2010.

[11] S. Richards, "Completed Richardson extrapolation in space and time," *Communications in Nuemerical Methods in Engineering,* vol. 13, pp. 573-582, 1997.

[12] A. Choudhary, C. Roy, J. Dietiker, M. Shahnam and R. Garg, "Code Verification for Multiphase Flows Using the Method of Manufactured Solutions," in *ASME 2014 4th Joint US-European Fluids Engineering Division Summer Meeting*

collocated with the ASME 2014 12th International Conference on Nanochannels, Microchannels, and Minichannels, Chicago, Illinois, USA, August 3–7, 2014.

[13] J. M. Vedovoto, A. da Silveira Neto, A. Mura and L. da Silva, "Application of the method of manufactured solutions to the verification of a pressure-based finite-volume numerical scheme," *Computers & Fluids*, vol. 51, no. 1, pp. 85-99, 2011.

[14] R. B. Bond, C. C. Ober, P. M. Knupp and S. W. Bova, "Manufactured Solution for Computational Fluid Dynamics Boundary Condition Verification," *AIAA Journal*, vol. 45, no. 9, pp. 2224-2236, 2007.

[15] A. Choudhary, C. J. Roy, E. A. Luke and S. Veluri, "Code verification of boundary conditions for compressible and incompressible computational fluid dynamics codes," *Computers and Fluids*, In review.

[16] U. Ghia, K. N. Ghia and C. T. Shin, "High-Re solutions for incompressible flow using the Navier-Stokes equations and a multigrid method," *Journal of Computational Physics*, vol. 48, no. 3, pp. 387-411, 1982.

[17] P. M. Gresho and S. T. Chan, "On the theory of semi-implicit projection methods for viscous incompressible flow and its implementation via a finite element method that also introduces a nearly consistent mass matrix. Part 2: Implementation," *International Journal for Numerical Methods in Fluids*, vol. 11, no. 5, pp. 621-659, 1990.

[18] R. Liska and B. Wendroff, "Comparison of Several Difference Schemes on 1D and 2D Test Problems for the Euler Equations," *SIAM J. Sci. Comput.*, vol. 25, no. 3, pp. 995-1017, 2003.

[19] M. Lee and R. D. Moser, "Direct numerical simulation of turbulent channel flow up to Re_tau = 5200," *Journal of Fluid Mechanics*, vol. 774, pp. 395-415, 2015.

[20] M. V. Zagarola and A. J. Smits, "Mean Flow Scaling of Turbulent Pipe Flow," *Journal of Fluid Mechanics*, vol. 373, pp. 33-79, 1998.

[21] F. Chen, E. C. Drumm and G. Guiochon, "Prediction/Verification of Particle Motion in One Dimension with the Discrete-Element Method," *International Journal of Geomechanics*, vol. 7, no. 5, p. 344–352, 2007.

[22] R. Garg, J. Galvin, T. Li and S. Pannala, "Open-source MFIX-DEM software for gas–solids flows: Part I—Verification studies," *Powder Technology,* vol. 220, pp. 122-137, 2012.

[23] A. Di Renzo and F. P. Di Maio, "Comparison of contact-force models for the simulation of collisions in DEM-based granular flow codes," *Chemical Engineering Science,* vol. 59, no. 3, pp. 525-541, 2004.

[24] A. H. Kharaz, D. A. Gorham and A. D. Salman, "An experimental study of the elastic rebound of spheres," *Powder Technology,* vol. 120, no. 3, pp. 281-291, 2001.

[25] L. Schiller and A. Naumann, "Fundamental calculations in gravitational processing," *Zeitschrift Des Vereines Deutscher Ingenieure,* vol. 77, pp. 318-320, 1933.

[26] C. J. Roy, C. C. Nelson, T. M. Smith and C. C. Ober, "Verification of Euler/Navier-Stokes codes using the method of manufactured solutions," *International Journal for Numerical Methods in Fluids,* vol. 44, no. 6, pp. 599-620, 2004.

[27] A. Choudhary, "Verification of Compressible and Incompressible Computational Fluid Dynamics Codes and Residual-based Mesh Adaptation," Ph.D. Dissertation, Virginia Tech, Blacksburg, 2015.

[28] S. B. Pope, "An Explanation of the Turbulent Round-Jet/Plane-Jet Anomaly," *AIAA Journal,* vol. 16, no. 3, 1978.

[29] D. C. Wilcox, Turbulence Modeling for CFD, DCW Industries, 1994.

[30] C. J. Roy, "Grid Convergence Error Analysis for Mixed-Order Numerical Schemes," *AIAA Journal,* vol. 41, no. 4, pp. 595-604, 2003.

[31] J. W. Banks, T. Aslam and W. J. Rider, "On sub-linear convergence for linearly degenerate waves in capturing schemes," *Journal of Computational Physics,* vol. 227, p. 6985–7002, 2008.

Appendix A: Manufactured Solution Mathematical Forms

(Note: All solution variables are in SI units.)

A.1 Baseline 3D Manufactured Solutions

The baseline manufactured solution selected for the verification study is a combination of sine and cosine functions and takes the following general form [26, 27]

$$\begin{aligned}\phi(x,y,z) = \phi_0 &+ \phi_x f_{\phi x}\left(\frac{a_{\phi x}\pi x}{L}\right) + \phi_y f_{\phi y}\left(\frac{a_{\phi y}\pi y}{L}\right) + \phi_z f_{\phi z}\left(\frac{a_{\phi z}\pi z}{L}\right) \\ &+ \phi_{xy} f_{\phi xy}\left(\frac{a_{\phi xy}\pi xy}{L^2}\right) + \phi_{yz} f_{\phi yz}\left(\frac{a_{\phi yz}\pi yz}{L^2}\right) \\ &+ \phi_{zx} f_{\phi zx}\left(\frac{a_{\phi zx}\pi zx}{L^2}\right)\end{aligned} \tag{A-1}$$

where, L is a characteristic length (herein, selected equal to the domain length or $L = 1$), and $\phi = \left[P_g, u_g, v_g, w_g, u_s, v_s, w_s, T_g, T_s\right]^T$ represents the set of primitive variables being tested for order of accuracy. The sinusoidal functions ($f_{\phi x}$, $f_{\phi y}$, etc.) selected are shown in the table below

Variable, ϕ	$f_{\phi x}$	$f_{\phi y}$	$f_{\phi z}$	$f_{\phi xy}$	$f_{\phi yz}$	$f_{\phi zx}$
u_g	sin	cos	cos	cos	sin	cos
v_g	sin	cos	cos	cos	sin	cos
w_g	cos	sin	cos	sin	sin	cos
P_g	cos	cos	sin	cos	sin	cos
T_g	cos	cos	sin	cos	sin	cos
T_s	cos	cos	sin	cos	sin	cos
ε_s	cos	cos	sin	--	--	--

The frequency constants ($a_{\phi x}$, $a_{\phi y}$, $a_{\phi xy}$, etc.) and the amplitude constants (ϕ_0, ϕ_x, ϕ_{xy}, etc.) are selected to ensure functions that are smooth but show reasonable periodicity and magnitude within the domain. The frequency constants selected are shown in the following table.

Variable, ϕ	$a_{\phi x}$	$a_{\phi y}$	$a_{\phi z}$	$a_{\phi xy}$	$a_{\phi yz}$	$a_{\phi zx}$
u_g	0.5	0.85	0.4	0.6	0.8	0.9
v_g	0.8	0.8	0.5	0.9	0.4	0.6
w_g	0.85	0.9	0.5	0.4	0.8	0.75
P_g	0.4	0.45	0.85	0.75	0.7	0.8
T_g	0.75	1.25	0.8	0.65	0.5	0.6
T_s	0.5	0.9	0.8	0.5	0.65	0.4
ε_s	0.4	0.5	0.5	--	--	--

The amplitude constants selected are shown in the following table.

Variable, ϕ	ϕ_0	ϕ_x	ϕ_y	ϕ_z	ϕ_{xy}	ϕ_{yz}	ϕ_{zx}
u_g	7	3	-4	-3	2	1.5	2
v_g	9	-5	4	5	-3	2.5	3.5
w_g	8	-4	3.5	4.2	-2.2	2.1	2.5
P_g	100	20	-50	20	-25	-10	10
T_g	350	10	-30	20	-12	10	8
T_s	300	15	-20	15	-10	12	10
ε_s	0.3	0.06	0.1	0.06	--	--	--

A.2 Two-Phase, 3D, Manufactured Solutions

The baseline manufactured solutions presented above are used to generate manufactured solutions for the two-phase flow test cases. As an example, the manufactured solution for the test case presented in Section 2.6 is provided next.

The manufactured solutions for the scalar variables (P_g, T_g, and T_s) are simply obtained from Eq. (A-1) and by substituting the appropriate functions and constants described above. For example, for the pressure variable (P_g), this function is as follow:

$$P_g = 100 + 20\cos(0.4\pi x) - 50\cos(0.45\pi y) + 20\sin(0.85\pi z) - 25\cos(0.75\pi xy) - 10\sin(0.7\pi yz) + 10\cos(0.8\pi zx) \quad \text{(A-2)}$$

The manufactured solutions for velocity components of the gas phase are obtained by taking the curl of the baseline velocity vector field, i.e.,

$$\vec{V}_g = u_g\hat{\imath} + v_g\hat{\jmath} + w_g\hat{k} = \begin{vmatrix} \hat{\imath} & \hat{\jmath} & \hat{k} \\ \dfrac{\partial}{\partial x} & \dfrac{\partial}{\partial y} & \dfrac{\partial}{\partial y} \\ \phi(u_g) & \phi(v_g) & \phi(w_g) \end{vmatrix} \quad \text{(A-3)}$$

where, for example, $\phi(u_g)$ is the baseline manufactured solution obtained from Eq. (A-1), the functions, and the constants described above for the variable u_g. This results in a divergence free velocity field because $\nabla \cdot (\nabla \times \vec{H})$ is identically zero for any vector field, $\vec{H}$. Thus, the manufactured solution for u_g is given as:

$$u_g = -\pi y \cos(0.4\pi yz) + 2.5\pi \sin(0.5\pi z) + 2.1\pi x \sin(0.6\pi zx) - 0.88\pi x \cos(0.4\pi xy) + 3.15\pi \cos(0.9\pi y) + 0.68\pi z \cos(0.8\pi yz) \quad \text{(A-4)}$$

Similarly, the manufactured solution for v_g and w_g can be derived.

Finally, the manufactured solution for velocity components of the solids phase is selected as simply the following divergence free field:

$$u_s = 5 \sin^2\big(0.5\pi(x + y + z)\big) \quad \text{(A-5)}$$

$$v_s = 5 \cos^2\big(0.5\pi(x + y + z)\big) \quad \text{(A-6)}$$

$$w_s = 5 \quad \text{(A-7)}$$

Manufactured solutions for other MMS test cases presented are derived using the baseline manufactured solutions and appropriate constraints (divergence free field, boundary conditions, etc.). For a complete look at the MMS function and MMS source terms, please see the `MMS_MOD.f` file under the respective test case of the MFIX distribution.

A.3 MMS02 manufactured solutions

The manufactured solutions for the two-phase, 3D, curl-based functions with constant volume fraction are listed below.

Gas pressure:

$$p_g = p_{g0} + p_{gx} \cos\left(A_{p_{gx}}\pi x\right) + p_{gy} \cos\left(A_{p_{gy}}\pi y\right) + p_{gxy} \cos\left(A_{p_{gxy}}\pi xy\right) + p_{gz} \sin\left(A_{p_{gz}}\pi z\right) + p_{gyz} \sin\left(A_{p_{gyz}}\pi yz\right) + p_{gzx} \cos\left(A_{p_{gzx}}\pi zx\right) \quad \text{(A-8)}$$

Gas velocity components:

$$u_g = A_{w_{gy}}\pi w_{gy} \cos\left(A_{w_{gy}}\pi y\right) + A_{w_{gxy}}\pi w_{gxy} x \cos\left(A_{w_{gxy}}\pi xy\right) - A_{v_{gyz}}\pi v_{gyz} y \cos\left(A_{v_{gyz}}\pi yz\right) + A_{w_{gyz}}\pi w_{gyz} z \cos\left(A_{w_{gyz}}\pi yz\right) + A_{v_{gz}}\pi v_{gz} \sin\left(A_{v_{gz}}\pi z\right) + A_{v_{gzx}}\pi v_{gzx} x \sin\left(A_{v_{gzx}}\pi zx\right) \quad \text{(A-9)}$$

$$v_g = -A_{w_{gxy}}\pi w_{gxy} y \cos\left(A_{w_{gxy}}\pi xy\right) + A_{u_{gyz}}\pi u_{gyz} y \cos\left(A_{u_{gyz}}\pi yz\right) + A_{w_{gx}}\pi w_{gx} \sin\left(A_{w_{gx}}\pi x\right) - A_{u_{gz}}\pi u_{gz} \sin\left(A_{u_{gz}}\pi z\right) - A_{u_{gzx}}\pi u_{gzx} x \sin\left(A_{u_{gzx}}\pi zx\right) + A_{w_{gzx}}\pi w_{gzx} z \sin\left(A_{w_{gzx}}\pi zx\right) \quad \text{(A-10)}$$

$$w_g = A_{v_{gx}}\pi v_{gx} \cos\left(A_{v_{gx}}\pi x\right) - A_{u_{gyz}}\pi u_{gyz} z \cos\left(A_{u_{gyz}}\pi yz\right) + A_{u_{gy}}\pi u_{gy} \sin\left(A_{u_{gy}}\pi y\right) + A_{u_{gxy}}\pi u_{gxy} x \sin\left(A_{u_{gxy}}\pi xy\right) - A_{v_{gxy}}\pi v_{gxy} y \sin\left(A_{v_{gxy}}\pi xy\right) - A_{v_{gzx}}\pi v_{gzx} z \sin\left(A_{v_{gzx}}\pi zx\right) \quad \text{(A-11)}$$

Solids velocity components:

$$u_m = u_{m0} \sin^2\left(\frac{\pi}{2}(x+y+z)\right) \quad \text{(A-12)}$$

$$v_m = v_{m0} \cos^2\left(\frac{\pi}{2}(x+y+z)\right) \quad \text{(A-13)}$$

$$w_m = w_{m0} \quad \text{(A-14)}$$

Gas and solids temperature:

$$T_g = T_{g0} + T_{gx} \cos\left(A_{T_{gx}}\pi x\right) + T_{gy} \cos\left(A_{T_{gy}}\pi y\right) + T_{gxy} \cos\left(A_{T_{gxy}}\pi xy\right) + T_{gz} \sin\left(A_{T_{gz}}\pi z\right) + T_{gyz} \sin\left(A_{T_{gyz}}\pi yz\right) + T_{gzx} \cos\left(A_{T_{gzx}}\pi zx\right) \quad \text{(A-15)}$$

$$T_m = T_{m0} + T_{mx} \cos\left(A_{T_{mx}}\pi x\right) + T_{my} \cos\left(A_{T_{my}}\pi y\right) + T_{mxy} \cos\left(A_{T_{mxy}}\pi xy\right) + T_{mz} \sin\left(A_{T_{mz}}\pi z\right) + T_{myz} \sin\left(A_{T_{myz}}\pi yz\right) + T_{mzx} \cos\left(A_{T_{mzx}}\pi zx\right) \quad \text{(A-16)}$$

Gas and solids volume fractions:

$$\varepsilon_g = 1 - \left(\varepsilon_{m0} + \varepsilon_{mx} \cos\left(A_{\varepsilon_{mx}}\pi x\right) + \varepsilon_{my} \cos\left(A_{\varepsilon_{my}}\pi y\right) + \varepsilon_{mxy} \cos\left(A_{\varepsilon_{mxy}}\pi xy\right) + \varepsilon_{mz} \sin\left(A_{\varepsilon_{mz}}\pi z\right) + \varepsilon_{myz} \sin\left(A_{\varepsilon_{myz}}\pi yz\right) + \varepsilon_{mzx} \cos\left(A_{\varepsilon_{mzx}}\pi zx\right)\right) \quad \text{(A-17)}$$

$$\varepsilon_m = \varepsilon_{m0} + \varepsilon_{mx}\cos\left(A_{\varepsilon_{mx}}\pi x\right) + \varepsilon_{my}\cos\left(A_{\varepsilon_{my}}\pi y\right) + \varepsilon_{mxy}\cos\left(A_{\varepsilon_{mxy}}\pi xy\right) + \varepsilon_{mz}\sin\left(A_{\varepsilon_{mz}}\pi z\right) + \varepsilon_{myz}\sin\left(A_{\varepsilon_{myz}}\pi yz\right) + \varepsilon_{mzx}\cos\left(A_{\varepsilon_{mzx}}\pi zx\right) \quad \text{(A-18)}$$

Solids granular temperature:

$$\theta_m = \theta_{m0} + \theta_{mx}\cos\left(A_{\theta_{mx}}\pi x\right) + \theta_{my}\cos\left(A_{\theta_{my}}\pi y\right) + \theta_{mxy}\cos\left(A_{\theta_{mxy}}\pi xy\right) + \theta_{mz}\sin\left(A_{\theta_{mz}}\pi z\right) + \theta_{myz}\sin\left(A_{\theta_{myz}}\pi yz\right) + \theta_{mzx}\cos\left(A_{\theta_{mzx}}\pi zx\right) \quad \text{(A-19)}$$

The parameters appearing in the manufactured solutions are as follows:

p_{g0}	100.0	v_{gx}	-5.0	w_{m0}	5.0	ε_{m0}	0.3
p_{gx}	20.0	v_{gy}	4.0	T_{g0}	350	ε_{mx}	0.0
p_{gy}	-50.0	v_{gz}	5.0	T_{gx}	10	ε_{my}	0.0
p_{gz}	20.0	v_{gxy}	-3.0	T_{gy}	-30	ε_{mz}	0.0
p_{gxy}	-25.0	v_{gyz}	2.5	T_{gz}	20	ε_{mxy}	0.0
p_{gyz}	-10.0	v_{gzx}	3.5	T_{gxy}	-12	ε_{myz}	0.0
p_{gzx}	10.0	$A_{v_{gx}}$	0.8	T_{gyz}	10	ε_{mzx}	0.0
$A_{p_{gx}}$	0.4	$A_{v_{gy}}$	0.8	T_{gzx}	8	$A_{\varepsilon_{mx}}$	0.5
$A_{p_{gy}}$	0.45	$A_{v_{gz}}$	0.5	$A_{T_{gx}}$	0.75	$A_{\varepsilon_{my}}$	0.5
$A_{p_{gz}}$	0.85	$A_{v_{gxy}}$	0.9	$A_{T_{gy}}$	1.25	$A_{\varepsilon_{mz}}$	0.5
$A_{p_{gxy}}$	0.75	$A_{v_{gyz}}$	0.4	$A_{T_{gz}}$	0.8	$A_{\varepsilon_{mxy}}$	0.4
$A_{p_{gyz}}$	0.7	$A_{v_{gzx}}$	0.6	$A_{T_{gxy}}$	0.65	$A_{\varepsilon_{myz}}$	0.4
$A_{p_{gzx}}$	0.8	w_{g0}	8.0	$A_{T_{gyz}}$	0.5	$A_{\varepsilon_{mzx}}$	0.4
u_{g0}	7.0	w_{gx}	-4.0	$A_{T_{gzx}}$	0.6	θ_{m0}	100.0
u_{gx}	3.0	w_{gy}	3.5	T_{m0}	300	θ_{mx}	5.0
u_{gy}	-4.0	w_{gz}	4.2	T_{mx}	15	θ_{my}	-10.0
u_{gz}	-3.0	w_{gxy}	-2.2	T_{my}	-20	θ_{mz}	12.0
u_{gxy}	2.0	w_{gyz}	2.1	T_{mz}	15	θ_{mxy}	-8.0
u_{gyz}	1.5	w_{gzx}	2.5	T_{mxy}	-10	θ_{myz}	10.0
u_{gzx}	-2.0	$A_{w_{gx}}$	0.85	T_{myz}	12	θ_{mzx}	7.0
$A_{u_{gx}}$	0.5	$A_{w_{gy}}$	0.9	T_{mzx}	10	$A_{\theta_{mx}}$	0.8
$A_{u_{gy}}$	0.85	$A_{w_{gz}}$	0.5	$A_{T_{mx}}$	0.5	$A_{\theta_{my}}$	1.25
$A_{u_{gz}}$	0.4	$A_{w_{gxy}}$	0.4	$A_{T_{my}}$	0.9	$A_{\theta_{mz}}$	0.7

$A_{u_{gxy}}$	0.6	$A_{w_{gyz}}$	0.8	$A_{T_{mz}}$	0.8	$A_{\theta_{mxy}}$	0.5
$A_{u_{gyz}}$	0.8	$A_{w_{gzx}}$	0.75	$A_{T_{mxy}}$	0.5	$A_{\theta_{myz}}$	0.6
$A_{u_{gzx}}$	0.9	u_{m0}	5.0	$A_{T_{myz}}$	0.65	$A_{\theta_{mzx}}$	0.7
v_{g0}	9.0	v_{m0}	5.0	$A_{T_{mzx}}$	0.4		

A.4 MMS03 manufactured solutions

The manufactured solutions for the two-phase, 3D, curl-based functions with variable volume fraction are listed below.

Gas pressure:

$$p_g = p_{g0} + p_{gx}\cos\left(A_{p_{gx}}\pi x\right) + p_{gy}\cos\left(A_{p_{gy}}\pi y\right) + p_{gxy}\cos\left(A_{p_{gxy}}\pi xy\right) + p_{gz}\sin\left(A_{p_{gz}}\pi z\right) + p_{gyz}\sin\left(A_{p_{gyz}}\pi yz\right) + p_{gzx}\cos\left(A_{p_{gzx}}\pi zx\right) \quad \text{(A-20)}$$

Gas velocity components:

$$u_g = \frac{1}{\varepsilon_g}\Big[A_{w_{gy}}\pi w_{gy}\cos\left(A_{w_{gy}}\pi y\right) + A_{w_{gxy}}\pi w_{gxy}x\cos\left(A_{w_{gxy}}\pi xy\right) - A_{v_{gyz}}\pi v_{gyz}y\cos\left(A_{v_{gyz}}\pi yz\right) + A_{w_{gyz}}\pi w_{gyz}z\cos\left(A_{w_{gyz}}\pi yz\right) + A_{v_{gz}}\pi v_{gz}\sin\left(A_{v_{gz}}\pi z\right) + A_{v_{gzx}}\pi v_{gzx}x\sin\left(A_{v_{gzx}}\pi zx\right)\Big] \quad \text{(A-21)}$$

$$v_g = \frac{1}{\varepsilon_g}\Big[-A_{w_{gxy}}\pi w_{gxy}y\cos\left(A_{w_{gxy}}\pi xy\right) + A_{u_{gyz}}\pi u_{gyz}y\cos\left(A_{u_{gyz}}\pi yz\right) + A_{w_{gx}}\pi w_{gx}\sin\left(A_{w_{gx}}\pi x\right) - A_{u_{gz}}\pi u_{gz}\sin\left(A_{u_{gz}}\pi z\right) - A_{u_{gzx}}\pi u_{gzx}x\sin\left(A_{u_{gzx}}\pi zx\right) + A_{w_{gzx}}\pi w_{gzx}z\sin\left(A_{w_{gzx}}\pi zx\right)\Big] \quad \text{(A-22)}$$

$$w_g = \frac{1}{\varepsilon_g}\Big[A_{v_{gx}}\pi v_{gx}\cos\left(A_{v_{gx}}\pi x\right) - A_{u_{gyz}}\pi u_{gyz}z\cos\left(A_{u_{gyz}}\pi yz\right) + A_{u_{gy}}\pi u_{gy}\sin\left(A_{u_{gy}}\pi y\right) + A_{u_{gxy}}\pi u_{gxy}x\sin\left(A_{u_{gxy}}\pi xy\right) - A_{v_{gxy}}\pi v_{gxy}y\sin\left(A_{v_{gxy}}\pi xy\right) - A_{v_{gzx}}\pi v_{gzx}z\sin\left(A_{v_{gzx}}\pi zx\right)\Big] \quad \text{(A-23)}$$

Solids velocity components:

$$u_m = \frac{1}{\varepsilon_m}\left[u_{m0}\sin^2\left(\frac{\pi}{2}(x+y+z)\right)\right] \tag{A-24}$$

$$v_m = \frac{1}{\varepsilon_m}\left[v_{m0}\cos^2\left(\frac{\pi}{2}(x+y+z)\right)\right] \tag{A-25}$$

$$w_m = \frac{1}{\varepsilon_m} w_{m0} \tag{A-26}$$

Gas and solids temperature:

$$\begin{aligned} T_g = T_{g0} &+ T_{gx}\cos\left(A_{T_{gx}}\pi x\right) + T_{gy}\cos\left(A_{T_{gy}}\pi y\right) + T_{gxy}\cos\left(A_{T_{gxy}}\pi xy\right) \\ &+ T_{gz}\sin\left(A_{T_{gz}}\pi z\right) + T_{gyz}\sin\left(A_{T_{gyz}}\pi yz\right) + T_{gzx}\cos\left(A_{T_{gzx}}\pi zx\right) \end{aligned} \tag{A-27}$$

$$\begin{aligned} T_m = T_{m0} &+ T_{mx}\cos\left(A_{T_{mx}}\pi x\right) + T_{my}\cos\left(A_{T_{my}}\pi y\right) + T_{mxy}\cos\left(A_{T_{mxy}}\pi xy\right) \\ &+ T_{mz}\sin\left(A_{T_{mz}}\pi z\right) + T_{myz}\sin\left(A_{T_{myz}}\pi yz\right) \\ &+ T_{mzx}\cos\left(A_{T_{mzx}}\pi zx\right) \end{aligned} \tag{A-28}$$

Solids granular temperature:

$$\begin{aligned} \theta_m = \theta_{m0} &+ \theta_{mx}\cos\left(A_{\theta_{mx}}\pi x\right) + \theta_{my}\cos\left(A_{\theta_{my}}\pi y\right) + \theta_{mxy}\cos\left(A_{\theta_{mxy}}\pi xy\right) \\ &+ \theta_{mz}\sin\left(A_{\theta_{mz}}\pi z\right) + \theta_{myz}\sin\left(A_{\theta_{myz}}\pi yz\right) \\ &+ \theta_{mzx}\cos\left(A_{\theta_{mzx}}\pi zx\right) \end{aligned} \tag{A-29}$$

The parameters appearing in the manufactured solutions are as follows:

p_{g0}	100.0	v_{gx}	-5.0	w_{m0}	5.0	ε_{m0}	0.3
p_{gx}	20.0	v_{gy}	4.0	T_{g0}	350	ε_{mx}	0.06
p_{gy}	-50.0	v_{gz}	5.0	T_{gx}	10	ε_{my}	-0.1
p_{gz}	20.0	v_{gxy}	-3.0	T_{gy}	-30	ε_{mz}	0.06
p_{gxy}	-25.0	v_{gyz}	2.5	T_{gz}	20	ε_{mxy}	0.0
p_{gyz}	-10.0	v_{gzx}	3.5	T_{gxy}	-12	ε_{myz}	0.0
p_{gzx}	10.0	$A_{v_{gx}}$	0.8	T_{gyz}	10	ε_{mzx}	0.0
$A_{p_{gx}}$	0.4	$A_{v_{gy}}$	0.8	T_{gzx}	8	$A_{\varepsilon_{mx}}$	0.4

$A_{p_{gy}}$	0.45	$A_{v_{gz}}$	0.5	$A_{T_{gx}}$	0.75	$A_{\varepsilon_{my}}$	0.5
$A_{p_{gz}}$	0.85	$A_{v_{gxy}}$	0.9	$A_{T_{gy}}$	1.25	$A_{\varepsilon_{mz}}$	0.5
$A_{p_{gxy}}$	0.75	$A_{v_{gyz}}$	0.4	$A_{T_{gz}}$	0.8	$A_{\varepsilon_{mxy}}$	0.4
$A_{p_{gyz}}$	0.7	$A_{v_{gzx}}$	0.6	$A_{T_{gxy}}$	0.65	$A_{\varepsilon_{myz}}$	0.4
$A_{p_{gzx}}$	0.8	w_{g0}	8.0	$A_{T_{gyz}}$	0.5	$A_{\varepsilon_{mzx}}$	0.4
u_{g0}	7.0	w_{gx}	-4.0	$A_{T_{gzx}}$	0.6	θ_{m0}	100.0
u_{gx}	3.0	w_{gy}	3.5	T_{m0}	300	θ_{mx}	5.0
u_{gy}	-4.0	w_{gz}	4.2	T_{mx}	15	θ_{my}	-10.0
u_{gz}	-3.0	w_{gxy}	-2.2	T_{my}	-20	θ_{mz}	12.0
u_{gxy}	2.0	w_{gyz}	2.1	T_{mz}	15	θ_{mxy}	-8.0
u_{gyz}	1.5	w_{gzx}	2.5	T_{mxy}	-10	θ_{myz}	10.0
u_{gzx}	-2.0	$A_{w_{gx}}$	0.85	T_{myz}	12	θ_{mzx}	7.0
$A_{u_{gx}}$	0.5	$A_{w_{gy}}$	0.9	T_{mzx}	10	$A_{\theta_{mx}}$	0.8
$A_{u_{gy}}$	0.85	$A_{w_{gz}}$	0.5	$A_{T_{mx}}$	0.5	$A_{\theta_{my}}$	1.25
$A_{u_{gz}}$	0.4	$A_{w_{gxy}}$	0.4	$A_{T_{my}}$	0.9	$A_{\theta_{mz}}$	0.7
$A_{u_{gxy}}$	0.6	$A_{w_{gyz}}$	0.8	$A_{T_{mz}}$	0.8	$A_{\theta_{mxy}}$	0.5
$A_{u_{gyz}}$	0.8	$A_{w_{gzx}}$	0.75	$A_{T_{mxy}}$	0.5	$A_{\theta_{myz}}$	0.6
$A_{u_{gzx}}$	0.9	u_{m0}	5.0	$A_{T_{myz}}$	0.65	$A_{\theta_{mzx}}$	0.7
v_{g0}	9.0	v_{m0}	5.0	$A_{T_{mzx}}$	0.4		

A.5 MMS04 manufactured solutions

The manufactured solutions for the No-slip wall BC, single phase, 3D, curl-based functions are listed below.

Gas pressure:

$$p_g = p_{g0} + p_{gx}\cos\left(A_{p_{gx}}\pi x\right) + p_{gy}\cos\left(A_{p_{gy}}\pi y\right) + p_{gxy}\cos\left(A_{p_{gxy}}\pi xy\right) + p_{gz}\sin\left(A_{p_{gz}}\pi z\right) + p_{gyz}\sin\left(A_{p_{gyz}}\pi yz\right) + p_{gzx}\cos\left(A_{p_{gzx}}\pi zx\right) \quad \text{(A-30)}$$

Gas velocity components:

$$\begin{aligned} u_g = x^2 \Big[& A_{w_{gy}} \pi w_{gy} \cos\left(A_{w_{gy}} \pi y\right) + A_{w_{gxy}} \pi w_{gxy} x \cos\left(A_{w_{gxy}} \pi xy\right) \\ & - A_{v_{gyz}} \pi v_{gyz} y \cos\left(A_{v_{gyz}} \pi yz\right) + A_{w_{gyz}} \pi w_{gyz} z \cos\left(A_{w_{gyz}} \pi yz\right) \\ & + A_{v_{gz}} \pi v_{gz} \sin\left(A_{v_{gz}} \pi z\right) + A_{v_{gzx}} \pi v_{gzx} x \sin\left(A_{v_{gzx}} \pi zx\right) \Big] \end{aligned} \quad \text{(A-31)}$$

$$\begin{aligned} v_g = x^2 \Big[& -A_{w_{gxy}} \pi w_{gxy} y \cos\left(A_{w_{gxy}} \pi xy\right) + A_{u_{gyz}} \pi u_{gyz} y \cos\left(A_{u_{gyz}} \pi yz\right) \\ & + A_{w_{gx}} \pi w_{gx} \sin\left(A_{w_{gx}} \pi x\right) - A_{u_{gz}} \pi u_{gz} \sin\left(A_{u_{gz}} \pi z\right) \\ & - A_{u_{gzx}} \pi u_{gzx} x \sin\left(A_{u_{gzx}} \pi zx\right) + A_{w_{gzx}} \pi w_{gzx} z \sin\left(A_{w_{gzx}} \pi zx\right) \Big] \\ & + 2x \Big[-w_{g0} - w_{gx} \cos\left(A_{w_{gx}} \pi x\right) - w_{gz} \cos\left(A_{w_{gz}} \pi z\right) \\ & - w_{gzx} \cos\left(A_{w_{gzx}} \pi zx\right) - w_{gy} \sin\left(A_{w_{gy}} \pi y\right) \\ & - w_{gxy} \sin\left(A_{w_{gxy}} \pi xy\right) - w_{gyz} \sin\left(A_{w_{gyz}} \pi yz\right) \Big] \end{aligned} \quad \text{(A-32)}$$

$$\begin{aligned} w_g = x^2 \Big[& A_{v_{gx}} \pi v_{gx} \cos\left(A_{v_{gx}} \pi x\right) - A_{u_{gyz}} \pi u_{gyz} z \cos\left(A_{u_{gyz}} \pi yz\right) \\ & + A_{u_{gy}} \pi u_{gy} \sin\left(A_{u_{gy}} \pi y\right) + A_{u_{gxy}} \pi u_{gxy} x \sin\left(A_{u_{gxy}} \pi xy\right) \\ & - A_{v_{gxy}} \pi v_{gxy} y \sin\left(A_{v_{gxy}} \pi xy\right) - A_{v_{gzx}} \pi v_{gzx} z \sin\left(A_{v_{gzx}} \pi zx\right) \Big] \\ & + 2x \Big[v_{g0} + v_{gy} \cos\left(A_{v_{gy}} \pi y\right) + v_{gxy} \cos\left(A_{v_{gxy}} \pi xy\right) \\ & + v_{gz} \cos\left(A_{v_{gz}} \pi z\right) + v_{gzx} \cos\left(A_{v_{gzx}} \pi zx\right) + v_{gx} \sin\left(A_{v_{gx}} \pi x\right) \\ & + v_{gyz} \sin\left(A_{v_{gyz}} \pi yz\right) \Big] \end{aligned} \quad \text{(A-33)}$$

Gas volume fraction:

$$\varepsilon_g = 1.0 \quad \text{(A-34)}$$

The parameters appearing in the manufactured solutions are as follows:

p_{g0}	100.0	v_{g0}	9.0
p_{gx}	20.0	v_{gx}	-5.0
p_{gy}	-50.0	v_{gy}	4.0
p_{gz}	20.0	v_{gz}	5.0

p_{gxy}	-25.0	v_{gxy}	-3.0
p_{gyz}	-10.0	v_{gyz}	2.5
p_{gzx}	10.0	v_{gzx}	3.5
$A_{p_{gx}}$	0.4	$A_{v_{gx}}$	0.8
$A_{p_{gy}}$	0.45	$A_{v_{gy}}$	0.8
$A_{p_{gz}}$	0.85	$A_{v_{gz}}$	0.5
$A_{p_{gxy}}$	0.75	$A_{v_{gxy}}$	0.9
$A_{p_{gyz}}$	0.7	$A_{v_{gyz}}$	0.4
$A_{p_{gzx}}$	0.8	$A_{v_{gzx}}$	0.6
u_{g0}	7.0	w_{g0}	8.0
u_{gx}	3.0	w_{gx}	-4.0
u_{gy}	-4.0	w_{gy}	3.5
u_{gz}	-3.0	w_{gz}	4.2
u_{gxy}	2.0	w_{gxy}	-2.2
u_{gyz}	1.5	w_{gyz}	2.1
u_{gzx}	-2.0	w_{gzx}	2.5
$A_{u_{gx}}$	0.5	$A_{w_{gx}}$	0.85
$A_{u_{gy}}$	0.85	$A_{w_{gy}}$	0.9
$A_{u_{gz}}$	0.4	$A_{w_{gz}}$	0.5
$A_{u_{gxy}}$	0.6	$A_{w_{gxy}}$	0.4
$A_{u_{gyz}}$	0.8	$A_{w_{gyz}}$	0.8
$A_{u_{gzx}}$	0.9	$A_{w_{gzx}}$	0.75

A.6 MMS05 manufactured solutions

The manufactured solutions for the Free-slip wall BC, single phase, 3D, curl-based functions are listed below.

Gas pressure:

$$p_g = p_{g0} + p_{gx}\cos\left(A_{p_{gx}}\pi x\right) + p_{gy}\cos\left(A_{p_{gy}}\pi y\right) + p_{gxy}\cos\left(A_{p_{gxy}}\pi xy\right) + p_{gz}\sin\left(A_{p_{gz}}\pi z\right) + p_{gyz}\sin\left(A_{p_{gyz}}\pi yz\right) + p_{gzx}\cos\left(A_{p_{gzx}}\pi zx\right) \quad \text{(A-35)}$$

Gas velocity components:

$$u_g = x^3\left[A_{w_{gy}}\pi w_{gy}\cos\left(A_{w_{gy}}\pi y\right) + A_{w_{gxy}}\pi w_{gxy}x\cos\left(A_{w_{gxy}}\pi xy\right)\right.$$
$$- A_{v_{gyz}}\pi v_{gyz}y\cos\left(A_{v_{gyz}}\pi yz\right) + A_{w_{gyz}}\pi w_{gyz}z\cos\left(A_{w_{gyz}}\pi yz\right)$$
$$\left. + A_{v_{gz}}\pi v_{gz}\sin\left(A_{v_{gz}}\pi z\right) + A_{v_{gzx}}\pi v_{gzx}x\sin\left(A_{v_{gzx}}\pi zx\right)\right] \quad \text{(A-36)}$$

$$v_g = v_{g0} + x^3\left[-A_{w_{gxy}}\pi w_{gxy}y\cos\left(A_{w_{gxy}}\pi xy\right) + A_{u_{gyz}}\pi u_{gyz}y\cos\left(A_{u_{gyz}}\pi yz\right)\right.$$
$$+ A_{w_{gx}}\pi w_{gx}\sin\left(A_{w_{gx}}\pi x\right) - A_{u_{gz}}\pi u_{gz}\sin\left(A_{u_{gz}}\pi z\right)$$
$$\left. - A_{u_{gzx}}\pi u_{gzx}x\sin\left(A_{u_{gzx}}\pi zx\right) + A_{w_{gzx}}\pi w_{gzx}z\sin\left(A_{w_{gzx}}\pi zx\right)\right]$$
$$+ 3x^2\left[-w_{g0} - w_{gx}\cos\left(A_{w_{gx}}\pi x\right) - w_{gz}\cos\left(A_{w_{gz}}\pi z\right)\right. \quad \text{(A-37)}$$
$$- w_{gzx}\cos\left(A_{w_{gzx}}\pi zx\right) - w_{gy}\sin\left(A_{w_{gy}}\pi y\right)$$
$$\left. - w_{gxy}\sin\left(A_{w_{gxy}}\pi xy\right) - w_{gyz}\sin\left(A_{w_{gyz}}\pi yz\right)\right]$$

$$w_g = w_{g0} + x^3\left[A_{v_{gx}}\pi v_{gx}\cos\left(A_{v_{gx}}\pi x\right) - A_{u_{gyz}}\pi u_{gyz}z\cos\left(A_{u_{gyz}}\pi yz\right)\right.$$
$$+ A_{u_{gy}}\pi u_{gy}\sin\left(A_{u_{gy}}\pi y\right) + A_{u_{gxy}}\pi u_{gxy}x\sin\left(A_{u_{gxy}}\pi xy\right)$$
$$\left. - A_{v_{gxy}}\pi v_{gxy}y\sin\left(A_{v_{gxy}}\pi xy\right) - A_{v_{gzx}}\pi v_{gzx}z\sin\left(A_{v_{gzx}}\pi zx\right)\right]$$
$$+ 3x^2\left[v_{g0} + v_{gy}\cos\left(A_{v_{gy}}\pi y\right) + v_{gxy}\cos\left(A_{v_{gxy}}\pi xy\right)\right. \quad \text{(A-38)}$$
$$+ v_{gz}\cos\left(A_{v_{gz}}\pi z\right) + v_{gzx}\cos\left(A_{v_{gzx}}\pi zx\right) + v_{gx}\sin\left(A_{v_{gx}}\pi x\right)$$
$$\left. + v_{gyz}\sin\left(A_{v_{gyz}}\pi yz\right)\right]$$

Gas volume fraction:

$$\varepsilon_g = 1.0 \quad \text{(A-39)}$$

The parameters appearing in the manufactured solutions are as follows:

p_{g0}	100.0	v_{g0}	9.0
p_{gx}	20.0	v_{gx}	-5.0
p_{gy}	-50.0	v_{gy}	4.0
p_{gz}	20.0	v_{gz}	5.0

p_{gxy}	-25.0	v_{gxy}	-3.0
p_{gyz}	-10.0	v_{gyz}	2.5
p_{gzx}	10.0	v_{gzx}	3.5
$A_{p_{gx}}$	0.4	$A_{v_{gx}}$	0.8
$A_{p_{gy}}$	0.45	$A_{v_{gy}}$	0.8
$A_{p_{gz}}$	0.85	$A_{v_{gz}}$	0.5
$A_{p_{gxy}}$	0.75	$A_{v_{gxy}}$	0.9
$A_{p_{gyz}}$	0.7	$A_{v_{gyz}}$	0.4
$A_{p_{gzx}}$	0.8	$A_{v_{gzx}}$	0.6
u_{g0}	7.0	w_{g0}	8.0
u_{gx}	3.0	w_{gx}	-4.0
u_{gy}	-4.0	w_{gy}	3.5
u_{gz}	-3.0	w_{gz}	4.2
u_{gxy}	2.0	w_{gxy}	-2.2
u_{gyz}	1.5	w_{gyz}	2.1
u_{gzx}	-2.0	w_{gzx}	2.5
$A_{u_{gx}}$	0.5	$A_{w_{gx}}$	0.85
$A_{u_{gy}}$	0.85	$A_{w_{gy}}$	0.9
$A_{u_{gz}}$	0.4	$A_{w_{gz}}$	0.5
$A_{u_{gxy}}$	0.6	$A_{w_{gxy}}$	0.4
$A_{u_{gyz}}$	0.8	$A_{w_{gyz}}$	0.8
$A_{u_{gzx}}$	0.9	$A_{w_{gzx}}$	0.75

Charles Zeh
Acting Executive Director
Technology Development & Integration Center
National Energy Technology Laboratory
U.S. Department of Energy

Bryan Morreale
Executive Director
Research & Innovation Center
National Energy Technology Laboratory
U.S. Department of Energy

Randall Gentry
Deputy Director
Science & Technology Strategic Plans & Programs
National Energy Technology Laboratory
U.S. Department of Energy

Technology Manager
Strategic Planning
Science & Technology Strategic Plans & Programs
National Energy Technology Laboratory
U.S. Department of Energy

NETL Technical Report Series